Bringing light into the nanoworld: What can you do with an atomic force microscope on top of your synchrotron radiation sample holder?

Mario Manuel Silveira Rodrigues

Thèse

présentée par

Mário Manuel Silveira Rodrigues

pour obtenir le grade de

Docteur de l'Université Joseph Fourier - Grenoble I

Physique de la matière condensée et du rayonnement

Bringing light into the nanoworld

What can you do with an atomic force microscope on top of your synchrotron radiation sample holder?

Directeurs de thèse:

Prof. Joel Chevrier et Dr. Fabio Comin

Membres du Jury:

Prof. Joost W. M. Frenken	Rapporteur
Prof. Olivier Thomas	Rapporteur
Prof. Joel Chevrier	Directeur de thèse
Dr. Fabio Comin	Directeur de thèse
Dr. Marc de Boissieu	Examinateur
Prof. Didier Tonneau	Examinateur

Soutenue le 29 Avril 2009

Thèse financée par la *Fundação para a Ciência e a Tecnologia*, Portugal

Thèse réalisée au *surface science laboratory* de l'European Synchrotron Research Facility, à Grenoble, France.

Acknowledgements

It is time to say a word about those who have shown us how to get there. I would like to restrict these acknowledgments to the persons who have directly contributed to my getting here.

First of all, my good old friends and Susana, who initially motivated me to enter the University. As at that time I was a full time employee at a cork factory and not by choice, going to the University implied a second order type of motivation. I think of these friends as the second order non negligible term. They gave me the kinetic energy necessary to cross inside the finite barrier potential well that is the university.

But once there, I needed extra energy get to an upper level than before being inside the well! This was indeed the part of my life when I needed the larger amount of kinetic energy because the barrier was definitely the larger. I have to thank enormously my supervisors at the cork factory, Luís and Manuel Martins. They never hesitated to grant me one or two extra hours during examination periods. They were always willing to adapt the factory's schedule to my student needs. They have been very good friends and without their friendship it really would not have been possible to get here, as I could not have attended several compulsory practicals without a rearrangement of the schedules. They were always willing to contribute to my education, since the days I was attending evening classes to complete high school. I always worked thirty minutes less though receiving the same complete salary! It is really impossible for me to translate into words their precious help. If I had worked the same eight years in some ordinary cork factory with some ordinary supervisors I would not have been able to get here. I was indeed fortunate...

To accomplish difficult deeds motivation is essential. And pleasure brings motivation. The pleasure of learning physics is very easily understood when one meets professors such as Margarida Godinho, J. Maia Alves, A. M. Vallêra and Olinda Conde. Again I was fortunate... The list may seem short, but I believe it is simply due to the fact that I hardly met most of my professors.

At this point of the crusade, and speaking of motivation and pleasure, I have to express my gratitude for Adalberto and Florinda who have always treated me like a son and, together with Susana, strongly motivated me from the beginning till the end and thus contributing directly... they were happy to see me keep on going. I have been very fortunate...

I am particularly thankful to professor Margarida Godinho for helping me in the way to the ESRF in Grenoble where I finished my Master. It was here that I met Prof. Jol Chevrier and Dr. Fabio Comin who became my thesis directors. I have to thank them a lot because they trusted me (I think), but particularly for their patience towards an emotional (physics can be highly emotional) and

sometimes very impatient person willing to add a few words into the conversation, even though many of these words turned out to be nonsenses. There are those who speak after thinking and those who think after speaking... Thank you!

At the Surface Science Laboratory I was again fortunate to work and discuss essentially with Olivier Dhez, Michal Hrouzek, Simon le Denmat, Alessandro Siria, Florence Marchi and Gauthier Torricelli, to all of them I would like to give a special thanks.

The reader will possibly find out that the aim of this work was to bring light (to be taken literally) to the atomic force microscopy world that has been left on the dark for many years now. The light was the ESRF light. Here I have worked with many people and without them most of the important results of this thesis work would not have been obtained. I would like to thank all of them but in particular I would like to thank R. Felici, T. H. Metzger, P. Glatzel, C. Mocuta, R. Magalhes Paniago, and T. Cornelius.

Finally, I would like to thank the members of the jury, in particular, professors Joost W. M. Frenken and Olivier Thomas for reading my manuscript in only a few days and for their comments and recommendations. It was for me a great pleasure to have Marc de Boissieu, with whom I sometimes share beam time at the ESRF, as the president of the Jury. Naturally, I also thank Professor Didier Tonneau for his participation in the jury.

There are many other people I would possibly like to thank...

Sommaire

Cette thèse a comme objectif principal la combinaison en temps réel et in-situ de deux types de spectroscopies différentes: la microscopie en champ proche et la spectroscopie avec la lumière de synchrotron. Donc cette thèse a pour but l'introduction de nouvelles techniques expérimentales qui permettent d'explorer les propriétés des matériaux à l'échelle nanométrique. Ces nouveaux instruments sont sensés permettre d'obtenir à la fois une image topographique et un contraste chimique avec une résolution latérale de 10-40 nm. Ceci repousserait les limites de chacune de ces deux familles de spectroscopies et ouvrirait la porte à de nouvelles opportunités de recherche et de défis. Pour réussir cette combinaison in situ et en temps réel, un microscope à force atomique (AFM) a spécialement été construit. Ce microscope a été développé autour d'un diapason à cristal de quartz qui était le capteur de force avec lequel des forces à l'échelle nanométrique ont été mesurées. Le microscope développé ici a été utilisé dans différentes lignes de lumières au synchrotron (ESRF) avec deux objectifs essentiellement différents. Un premier objectif était de faire de la spectroscopie, comme la mesure d'un seuil d'absorption, localement au moyen de la pointe de l'AFM. Ce type de mesures a effectivement été fait, mais la résolution latérale obtenue n'était pas donnée par la géométrie de la pointe mais par la taille du faisceau X. La pointe de l'AFM a également été utilisée pour mesurer la diffraction de Bragg dans des cristaux de tailles inférieures au micromètre. Un deuxième objectif a été d'utiliser la pointe de l'AFM pour interagir mécaniquement avec des systèmes à l'échelle nanométrique et simultanément utiliser un faisceau X pour mesurer des changements du paramètre de mailles dans les systèmes en question. Ainsi, la pointe de l'AFM a été utilisée pour déformer élastiquement un cristal de SiGe pendant que le signal de diffraction été mesuré. Ceci a permis d'observer des décalages des pics de Bragg en fonction de la pression appliquée par la pointe. La combinaison in-situ de microscopie atomique avec la diffraction a, cette fois ici, permis d'obtenir le module d'Young d'un cristal à l'échelle nanométrique sans aucun paramètre ajustable.

Summary

The major objective of this thesis work was to combine in situ and in real time Scanning Probe Microscopies and, in particular, Atomic Force Microscopy, with Synchrotron Radiation based techniques. The work naturally led to the introduction of new experimental techniques particularly adapted to the investigation of nano-sized materials. The initial goal of the project was to develop instrumentation capable of providing chemical contrast with lateral resolution of 10-40 nm, overcoming the existing limitations of the two separate techniques (synchrotron Radiation and Scanning probe Microscopies) and opening a wide range of research opportunities and challenges. Following this vision an adapted Atomic Force Microscope has been developed. At its heart is a quartz tuning fork crystal acting as the sensor of atomic forces. A quartz tuning fork does not need currents, does not need laser beams, and is very well suited to be used in beamline endstations. The name given to this atomic force microscope specifically developed for beamlines is X-AFM and the instrument has been mounted and tested in many endstations following essentially two lines of experiments.

A first line of experiments exploited the X-AFM as a microscope and as a beamfinder, for eventually using the tip as a detector. In absorption spectroscopy, done by collecting all the electrons emitted from the sample, the measurements indicated that the lateral resolution is still dominated by the X-ray beam size rather than by the tip apex shape, while in diffraction from nanosized particles, where the tip is used to see the diffracted spots, the resolution was actually defined by the tip.

A second line of experiments was to use the X-AFM as an instrument to mechanical interact with nano-sized systems while the X-ray beam was used to probe changes in the lattice parameter. The X-AFM tip was used to elastically indent a SiGe crystal while diffraction was simultaneously measured. It was possible to observe shifts of the Bragg peak as a consequence of the applied pressure. In this experiment, the in-situ combination of AFM with synchrotron radiation has permitted to measure the Young modulus of a crystal at the nanoscale without any kind of adjustable parameter.

The experiments presented in this thesis work show that the X-AFM is a beam monitor, a nanoscope and a force actuator: other experiments can then be formulated and carried out starting from these first ones.

Résumé

Le manuscrit se compose de cinq chapitres dont un l'introduction qui met en contexte tout le travail et explique/discute certaines choix. Le dernier chapitre est une conclusion/discussion qui apporte peu de neuf mais qui a comme objectif vite faire comprendre quelle a été la direction de cette thèse et quelles sont les conclusions importantes après chaque chapitre. Les chapitres plus spécifiques sont le chapitre deux, trois et quatre. Le chapitre deux est dédié au diapason utilisé pour construire le Microscope à Force Atomique (AFM) avec lequel différentes expériences dans plusieurs *beamlines* ont été réalisées. Le chapitre trois discute comment l'AFM a été construit et quel est le rle du diapason dans sa construction. Le chapitre quatre considère des différentes situations d'utilisation de ce AFM, tout à fait adapté aux lignes de lumière du synchrotron, pour faire des expériences qui ne sont pas une combinaison linéaire des deux techniques: Microscopie à Force Atomique et diffraction/absorption de rayons X.

Cette thèse a été réalisée au SSL (surface science laboratory) de l'European Synchrotron Research Facility, à Grenoble, France. Au SSL nous avons construit différentes prototypes d'AFM qui ont été testés sur des différentes lignes de lumière.

Ensuite nous allons faire un petit résumé de chaque chapitre.

Introduction

Depuis l'invention de l'STM dans les années 80 et de l'AFM dans la même décennie, la microscopie à balayage en champ proche a bien occupé sa place dans l'étude des *nanosystèmes*. Aujourd'hui nous pouvons facilement obtenir résolution atomique avec toutes les deux techniques mentionnées ci-dessus. Cependant, l'information obtenue est plutt structural. Dans le cas de l'AFM, cette information peut très facilement se lier à la topographie. Dans le cas de l'STM c'est la topographie des électrons ou la densité d'états. Dans les deux cas l'identification atomique reste un problème très difficile. Par exemple, avec l'STM, lorsque nous regardons une molécule, certaines parties de la molécule peuvent être invisibles.

Dans l'autre extrême, nous avons la recherche dans les synchrotrons. Ici nous avons la résolution chimique donné par la spectroscopie des rayons X. Cela permet identifier facilement les atomes qui constituent les matériaux, qu'ils soient liquides, gazes ou solides. Avec cette lumière et des cristaux compliqués constitués par des protéines, les chercheurs ont pu obtenir la complexe structure chimique et structural des différentes protéines. Ceci n'est qu'un exemple. L'importance des synchrotrons dans les nanosciences est indiscutable. En ef-

fet, toutes ces deux familles de techniques ont prouvé être indispensables à la compréhension du *nanomonde*.

Jusqu'à récemment, les deux champs d'investigation, microscopie à champ proche et recherche dans les synchrotrons, étaient indépendants l'un de l'autre. Ils étaient utilisés de façon complémentaire. Ici **l'idée est de pouvoir utiliser la microscopie en champ proche et la recherche dans les synchrotrons de façon à obtenir des résultats qui ne sont pas possibles en utilisant ces deux familles de techniques indépendamment**.

Un exemple assez bien réussit est donné dans le dernier chapitre ou nous utilisons la pointe de l'AFM, ici développée, pour déformer une nano particule de SiGe dans le régime élastique. Pendant la déformation nous avons simultanément observé la décalage du pic de Bragg. L'information simultané du gradient de force mesuré avec le diapason et du changement du paramètre de maille ont permis obtenir le module de Young de cette nanoparticule.

Pour ces types de mesures le choix de l'AFM semble honnête et normal. Cependant, nous pouvons penser à des combinaisons o les choix champ proche plus synchrotron peuvent être moins évidentes. Par exemple, nous pouvons considérer l'illumination de l'échantillon par les rayons X et la subséquente détection de l'absorption avec la pointe de l'AFM ou de l'STM. L'idée est de limiter la mesure à la taille de l'apex de la pointe (20 nm) qui est plus petit que le faisceau (quelques microns). Par contre, nous pouvons aussi penser à mesurer un changement de la probabilité d'un électron qui subit l'effet tunnel induit par l'absorption de photons. La haute résolution latéral du STM est conservée. Si nous mesurons la quantité total d'électrons émis, il est nécessaire d'isoler la pointe de façon à laisser seulement une petite ouverture au but pour augmenter la résolution latéral. La recherche d'une pointe qui peut permettre d'améliorer la résolution latéral fut aussi sujet de cette thèse.

Au moment du commencement de ce travaille quelques groupes ont voulu combiner la lumière des synchrotrons avec les techniques de champ proche. Cependant, la préférence était toujours vers le microscope à effet tunnel. Dans ce projet, nous avons désiré exploiter le plus grand nombre de possibilités. Nous pouvons, par exemple, faire des images de n'importe quel surface avec l'AFM mais les surfaces doivent être conductrices pour être imagées avec l'STM. L'AFM permet également d'interagir mécaniquement avec le *nanomonde* qu'on désire exploiter.

Théorie du diapason

Ce chapitre introduit le diapason utilisé pour construire l'AFM.

Le principe de fonctionnement est très simple. Le diapason est en quartz et lorsqu'il oscille, le stress dans le matériel est converti en charge. Cela permet de détecter son mouvement oscillatoire lorsqu'une force oscillante excite le diapason. Comme touts les diapasons, le facteur de qualité de ceci est très grand, ce que nous permet de mesurer des très petites décalages de sa fréquence de résonance. La fréquence du diapason dépende initialement de la raideur des poutres dont il est composé et de la masse effective de chaque poutre. Lorsqu'on interagit avec la surface, le gradient de cette interaction (force) s'additionne a la raideur des poutres. Cela introduit une décalage de la fréquence de résonance du diapason. Le contrle de la décalage de cette fréquence en fonction de la

distance permet d'obtenir la topographie de la surface en question. Dans le chapitre suivant nous allons meilleur expliquer comment ça fonctionne.

Ici nous sommes plus intéressés a comprendre le diapason. Cela est nécessaire si on veut faire mieux que tout simplement obtenir des images d'une surface. Pour quantifier les interactions nous devons comprendre exactement comment la fréquence de résonance du diapason se décale en fonction de l'interaction.

Le plus usuel dans la littérature est de reprendre tout ce qui a été fait pour le micro levier Si. Ce type de micro levier est le plus usuel dans l'AFM. Cependant, le même ne peut être appliqué au diapason parce que le couplage entre les deux poutres qui constituent le diapason est négligé.

Dans le modèle que nous allons soutenir nous commençons par considérer les poutres individuellement. L'équation de poutre de Euller-Bernoulli est retrouvée. C'est possible de vérifier que la fréquence du diapason n'est pas donnée par la fréquence d'une poutre individuel comme considéré normalement.

Après, nous avons couplé les deux poutres à l'aide d'un ressort idéal. Cette couplage résulte dans une fréquence de résonance qui est plus basse que la fréquence de résonance des poutres individuelles. Après ceci, nous devons coupler les deux oscillateurs avec la surface. Nous calculons alors, une nouvelle relation entre décalage de fréquence et interaction. En particulier, nous assumons que cette relation est valable jusqu'à des interactions de plusieurs kN/m.

Nous discutons aussi les différentes possibilités d'exciter le diapason, dont les plus usuels sont l'excitation mécanique et l'excitation électrique. Autres types d'excitation sont aussi discutés. Nous avons préféré l'excitation mécanique parce que cela nous permet d'utiliser les contacts du diapason de façon plus intéressante. L'excitation électrique est cependant plus local mais il faut un circuit électrique additionnel qui permet compenser la capacité parasite constituée par les électrodes déposés dans le diapason à quartz.

Le résultat plus important que nous devons retenir de ce chapitre est la relation entre la décalage de la fréquence de résonance du diapason et l'interaction.

Un AFM avec un diapason

Dans ce chapitre nous discutons les choix qui ont été faites pour la construction de l'AFM qui va être utilisé pour faire des expériences o nous utilisons à la foi la puissance local de l'AFM et la résolution chimique et structural donnée par la lumière de synchrotron. Nous commençons pour faire une introduction aux techniques qui permettent obtenir des images en microscopie à force atomique. Nous discutons l'utilisation soit du *Lock in amplifier* soit d'une *Phase Locked Loop* (PLL) et les avantages et les inconvénients de ces deux techniques sont discutés dans le cas de l'AFM avec un diapason. Nous discutons comment la phase (Lock in) ou la fréquence de résonance (PLL) peuvent être utilisées pour obtenir une image. En général, nous concluons que l'utilisation d'une PLL permet de gagner du temps par un facteur deux ou trois.

Au début de ce chapitre nous faisons également une comparaison entre la performance que on peut espérer si on utilise un diapason millimétrique à quartz on un micro levier Si plus couramment utilisé dans ce contexte. Nous concluons que cette performance est comparable et que le prix à payer pour l'utilisation pratique d'un oscillateur millimétrique est le temps d'acquisition d'une image, parce que pour compenser la raideur du diapason millimétrique il faut que son

facteur de qualité soit très grand et donc le temps de relaxation du diapason est également plus grand. En conclusion, la sensibilité de l'oscillateur dépend de la raison k/Q ou k est la constante de raideur et Q le facteur de qualité.

Les différentes éléments qui composent le microscope sont introduits. Plusieurs images qui montrent la performance du microscope sont données. Il a également été utilisé dans les contextes mécaniquement plus violents que quand il est utilisé dans un laboratoire calme. En particulier, plusieurs images ont été obtenues dans différentes lignes de lumière au synchrotron.

Nous avons aussi utilisé le microscope pour mesurer les forces latérales qui apparaissent lorsqu'un corps se déplace latéralement proche d'une surface à des distances de l'ordre du nanomètre. Depuis plusieurs années, différents chercheurs ont débattu l'origine de ce type d'interaction bien que la distance à partir de laquelle ces forces deviennent importantes. Nous avons utilisé le diapason pour conclure que ces forces n'apparaissent que quand on est en contact ou à des distances plus petites que le nanomètre. Pour montrer ça, le diapason a été excité de façon à osciller simultanément parallèle et normal à la surface. Comme les interactions qui apparaissent lorsqu'un oscillateur oscille perpendiculairement à la surface sont bien connues, on peut utiliser ces interactions connues pour estimer la distance entre le corps qui oscille parallèlement à la surface et la surface. En résume, nous avons montré que le microscope à force atomique ici développé est prêt pour aller dans une *beamline* ou le but va être de combiner/coupler soit la diffraction soit l'absorption de rayons X avec l'AFM.

Un AFM dans une ligne de lumière

Dans le chapitre antécédent à la conclusion, nous donnons plusieurs exemples o l'AFM et la lumière de synchrotron sont couplés. Cependant, avant pouvoir faire les expériences plus intéressantes nous devons penser à plusieurs détails comme l'alignement de la pointe avec le faisceau et avec les objets à étudier.

Nous commençons par expliquer la procédure expérimental et nos choix dans ce contexte.

Après, nous discutons comment l'absorption de lumière par la pointe métallique peut être utilisé pour l'alignement pointe plus faisceau. Ici nous essayons de quantifier le courant mesuré par la pointe lorsqu'elle absorbe de la lumière en termes de photons absorbés. Certains facteurs géométriques interviennent. Un autre facteur important est lié à la capacité que les électrons ont de se déplacer dans les matériaux lorsqu'ils ont été accélérés par un champ électromagnétique. L'ensemble de considérations que sont ici faites, nous donne aussi un limite théorique de la résolution latéral qu'on peut espérer si on veut détecter localement les électrons photoémits. Tandis que ceci est un des objectives de ce travaille. Ici, la conclusion a été que la meilleure résolution qu'ont peut obtenir est de l'ordre des 30nm. Même si la pointe ne mesure des électrons très localement, les photons qui ont été absorbés à 30 nm de la pointe peuvent produire un électron qui sera détecté par la pointe.

Après avoir appris à aligner le faisceau avec la pointe, il suffit de bouger l'échantillon pour aligner les objets qu'on veut étudier avec la pointe. La position de la pointe reste fixe par rapport à la position de l'échantillon.

Trois directions différentes ont été suivies:

1. AFM et simultanément Spectrométrie d'absorption des rayons X *local*. Le mot local signifie que la spectrométrie est mesurée avec la pointe de l'AFM. Nous avons obtenu plusieurs spectres d'absorption mesurés avec la pointe en tungstène collée au diapason. Cependant, pour avoir une bonne résolution spatiale, la pointe doit être couverte excepte au but pour pouvoir rejeter les électrons que sont émis des régions plus loin de l'apex. Les pointes qui permettront ceci sont encore objet de recherche. Les limites de cette technique sont discutés.

2. AFM et simultanément Diffraction des rayons X *local*. Les photons diffractés seront mesurés avec la pointe de l'AFM. Avec la pointe de l'AFM nous avons pu mesurer plusieurs courbes de diffraction. Ici la résolution latéral est meilleure que dans les cas précédents parce que l'émission des photons qui sont diffractés a un caractère plus locale. Une pointe sensible qu'au but permettra une résolution spatiale meilleure. Ce type de pointe permet aussi de réduire le *background* de photoélectrons non désiré ici.

3. indentation et simultanément Diffraction des rayons X. C'est ici que le résultat final de cette combinaison de techniques a permit d'obtenir les meilleurs résultats. La pointe a été utilisée pour déformer élastiquement une nanoparticule de SiGe et simultanément la particule était illuminée par les rayons X. L'information du gradient de force obtenu avec le diapason o la pointe est collé, associée à l'information du décalage du pic de diffraction a permit la détermination du module de Young de la nanoparticule. Ceci est un résultat important parce qu'il y a encore à découvrir dans la mécanique du *tout petit*.

Au début du projet les points les plus motivants étaient le premier et troisième mentionné ci-dessus. Si le troisième a été plutt un sucés, le premier moins. La difficulté de faire une *smart tip* est la raison. La *smart tip* est l'outil que permettra la collection locale d'électrons photoémits. Dans la partie final du chapitre quatre nous discutons les différents chemins qui ont été choisis pour arriver a une *smart tip*.

Conclusions et sommaire

La conclusion est en forme de résumé qui rappelle le pointes importantes de ce travaille et n'est pas très différente de ce résumé.

Dans la discussion finale nous observons que dans ce travaille il n'y a pas eu une vrai combinaison AFM et spectrométrie de rayons X parce que nous n'avons pas mesuré l'influence de l'absorption dans la force entre la pointe et la surface. Si en illuminant l'échantillon nous pouvons changer la densité d'électrons qui contribue aux interactions chimiques et simultanément mesurer ce changement d'interaction avec l'AFM nous faisons une interférence constructive des deux techniques. La différence est qu'on ne mesure pas les électrons photoémits de la surface illuminée mais le changement de force induite par le fait que la surface soit illuminée. Cette force est très locale, limité à la projection de l'apex de la pointe dans la surface. Une *smart tip* n'est plus nécessaire.

Contents

Chapter 1

Introduction

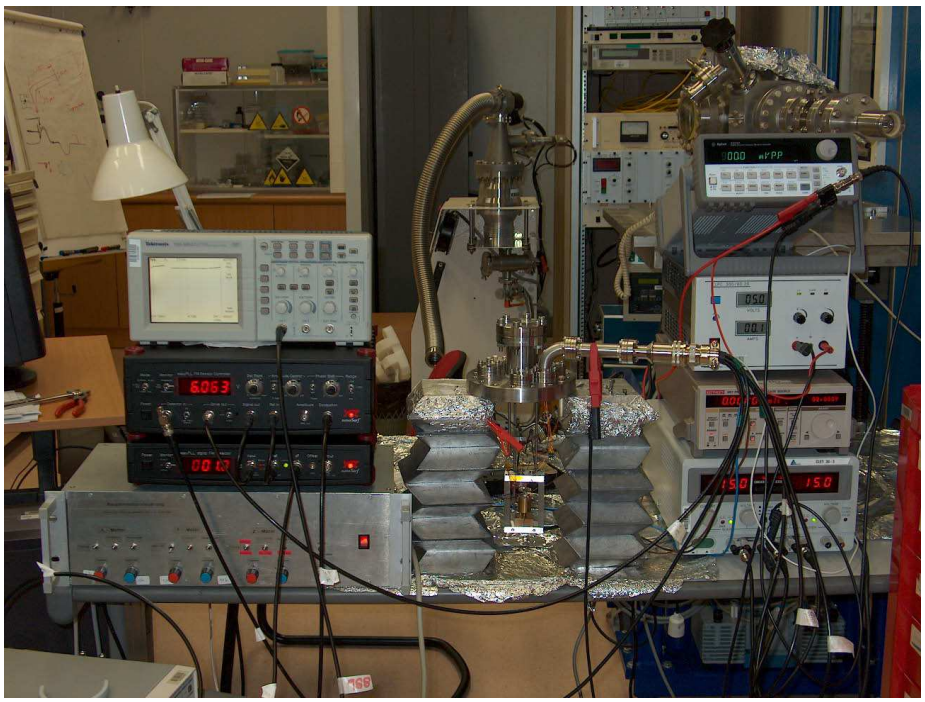

Contents

1.1 The X-tip project

The drop image and the rainbow

In the two last decades the use of synchrotron radiation (SR) has grown enormously. SR is used in many different ways to explore both the geometric and electronic properties of all kinds of condensed matter systems. However, Synchrotron Radiation, *averages* over all the illuminated volume.

The spatial resolution when using X-rays is often limited to the μm scale because of the difficulty to focus X-rays to spot sizes smaller than that. Thus, as far as the study of nano-objects is concerned, it is like looking at a rainbow where a spectrum can be observed but is the result of an average process coming from several illuminated droplets. Through the spectral analysis of the rainbow one can access the physical properties of the drops, such as their index of refraction, absorption coefficient etc, and thus have chemical sensitivity since the optical properties of material depend strongly on their chemical constituents. Since the beginning of the last century X-ray beams made it possible to easily measure inter-atomic distances [1, 2, 3]. Hence, synchrotron radiation provides us with a very large field of view, but does not let us see (except for certain particular cases [4]) nor touch what is being studied.

On the other hand, there is a field of surface science that also has been growing as fast as Synchrotron Radiation techniques. Since the invention of Scanning Tunneling Microscopy (STM, 1981 [6, 7]), Scanning Probe Microscopies (SPM) in general, and among them Atomic Force Microscopy (AFM) [8, 9, 10] found a very fast development and have been used to probe a large variety of surfaces. These techniques allow us to image individual atoms [11, 12]. Scanning Probe Microscopy (SPM) techniques are used in many scientific fields ranging from biology to materials sciences. Nowadays, they are thought to be at the heart of nanoscience. SPMs are easy to use, produce high resolution images of the sample and unveil many properties of the surface. Furthermore, they can interact with the atoms [13] or with small particles [14].

SPMs, however have their limits: usually they cannot tell or image the chemical properties of the atoms being imaged.

With particular experiments in STM it is actually possible to access chemical information of the imaged atoms, but this is not always straightforward and is limited to conductive samples. And chemical sensitivity is even more difficult with an AFM.

On the SR side, it is actually possible to image particles with dimensions as small as 100 nm making use of the coherent part of the radiation for example [4]. Also this reconstruction is complicated and it requires a number of algorithms to go from the reciprocal space to the real space [15, 16]. Still, is not possible to mechanical interact with particle.

In the most recent years the use of micro and nano X-ray beams is steadily increasing and the joint exploitation of SPM and Synchrotron Radiation techniques seems ever more desirable.

In micro-nano characterization it is often necessary to work on a single object whose size can vary from the micro to the nanoscale. For more systematic and comprehensive exploration of the micro-nano world, it is covetable to perform SPM and X-ray experiments on the same single object in the same conditions and at the same time.

The X-tip project

The motivations for the X-tip project [17] are directly linked to what has been mentioned above. The idea is depicted in figure 1.1.

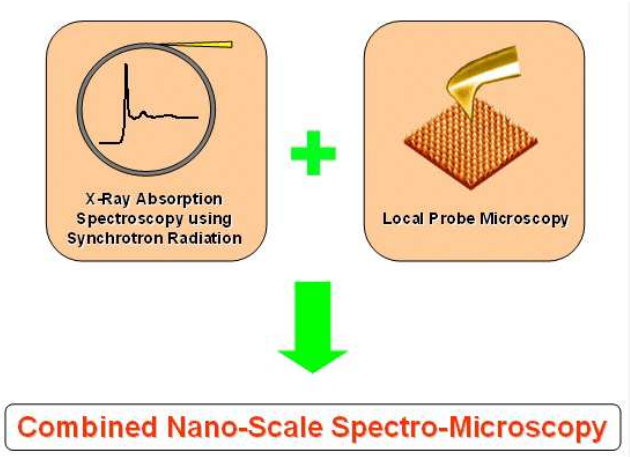

Figure 1.1: Illustration of the X-tip idea which is to combine the field of view of synchrotron light with the ability to see and touch of scanning probe microscopies. The illustration was taken from the website: http://213.175.108.134/xtip/objectives.htm.

Let us take a ferromagnetic sample for example. Using Magnetic Force Microscopy (MFM) [18], one of the many declinations of an AFM, it is easy to image different magnetic domains. On the other hand, synchrotron radiation is used to directly probe the electronic properties of a sample, thus magnetic properties, namely trough measurements such as linear or circular dichroism [19, 20]. However, synchrotron radiation beams are easily larger than magnetic domains. Thus, one of X-tip's ideas was to localize the measure of such linear or circular dichroism just below the tip of an AFM/STM. In this way, not only the magnetic domains can be imaged, but also the electronic properties of the individual domains can be studied.

As a matter of fact the X-tip vision was projecting even further:

The X-TIP project *was targeted at exploring the frontiers of knowledge by introducing new types of experimental techniques suitable for the investigation of nano-sized materials. The proposed new instrumentation, based on*

a combination of Local Probe Microscopies (LPM) such as Atomic Force Microscopy (AFM), Scanning Tunneling Microscopy (STM) and Scanning Near-field Optical Microscopy (SNOM) with X-Ray Spectromicroscopy (XRS), will provide chemical-specific contrast at unprecedented lateral resolution of up to 10-40 nanometers, thus overcoming existing limitations of the two (LPM and XRS) methods and opening a wide range of research opportunities and challenges.

This thesis work relates to the part of the X-tip project that is focused on AFM and its implementation on SR beam lines.

The thesis can be divided into two major parts:

- The first part is obviously the construction of an X-AFM. The reason is simply because it did not exist in the market a commercial AFM compact enough and open (physically) enough to go on top of a diffractometer or any other synchrotron sample holder.

- The second step is obviously to try and **X-tip it**. This has always been difficult, because one naturally needs to run some tests. But testing, it seems, is not what the beam lines are made for. Nevertheless, preliminary but encouraging results in different fields helped a lot. The idea was not at all limited to do SPM and SR experiments on line, one after the other, but rather to do those experiments that can be achieved only trough the combination of the two techniques.

As an example where X-tip has been successful, is the experiments where the X-AFM tip was used to nano-indent a particle while collecting simultaneously diffraction. It was as looking at the same time the rainbow from the drop and touching the drop. This combination allowed the determination of the particle's Young modulus without any adjustable parameter while using a very simple model.

Concerning local detection of spectroscopies with the tip, the success of this combination depends on the future development of smart tips.

1.2 How to combine SPM with synchrotron light?

Many paths have already been explored to combine SR and SPM. A first one consisted in combining Scanning Tunneling Microscopy with X-ray beams with the intention to provide chemical contrast in near field microscopies [21]. This was done by installing an Ultra High Vacuum Scanning Tunneling Microscope on a dedicated X-ray beam line [22, 23, 24]. According to the authors, X-rays induce changes in the tunneling probability adding then chemical contrast of the order of tens of nanometers to the usual topographic resolution of a Scanning Tunneling Microscope.

A different approach was taken by Ishii [25], who has combined X-ray absorption with Scanning Capacitance Microscopy [26] to probe localized charges. This last technique parallels Electrostatic Force Microscopy [27] and Kelvin Probe Microscopy [28, 29], both belonging to the family of the Atomic Force Microscopies. We shall come back to this, a little below.

Due to the versatility of the Atomic Force Microscope (AFM), we considered an extensive integration of SPM techniques on synchrotron radiation beam lines in order to combine them indifferently with diffraction or with spectroscopy experiments. For this purpose, we adapted compact, optics free AFM instruments to typical end stations. As previously mentioned, we have also used the tip as a nanomanipulation tool for sample interaction under X-ray beams. The AFM can, of course, be operated in its Magnetic Force Microscopy mode to image individual magnetic domains and perform local spectroscopy even if X-ray beams are larger than domain dimensions.

The work aimed to explore the versatility, ease of use and extent of the applications spectrum of such an instrument. The difficulties to overcome involved essentially issues of stability and alignment, since on one hand the beamline environment is not devoid of mechanic vibrations and on the other hand, the alignment of tip, sample and microbeam should be a routine procedure for an easy exploitation of the instrument. As a general reference, beamlines that do not need a diffractometer are stable enough to allow a vertical resolution of 1or 2 nanometer. On diffractometer based beamlines, this value can increase to about 20 nanometers, depending on the particular setup.

To solve the problem of alignment, the X-AFM tip has been used as a beam position monitor. Conversely, the tip can be used as a local absorption and diffraction detector. The lateral resolution in this case is still rather limited, due to the technical difficulty of producing coaxial tips bare just on their apex. A reliable method for preparing tips that leaves a submicrometer open metallic apex is still under development. We call these *Smart Tips*. Once this task is accomplished, a lateral resolution better than 50 nm is expected. The main underlying idea is that tip-mediated detection is intrinsically localized to the area *seen* by the tip (few nm) even if the beam is spread over a much wider sample area.

The microscope we developed operates very much like a conventional AFM but with a simplified, and more robust setup. In conventional AFMs, the deflection of the cantilever is detected by measuring with a Position Sensitive Photodetector the position of a laser beam reflected by the back of the cantilever. The deflection of this beam is function of the bending of the cantilever. In contrast, the AFM presented here is based on a quartz tuning fork (TF). Because quartz exhibits natural piezoelectricity, this solution allows direct detection of the motion of the oscillator since its alternating stress field is converted into alternating charge, i.e., current. The use of TFs in SPM design has been the subject of a vast and fast growing literature [30, 31].

AFM, STM, EFM or (...) ?

Obviously, the first question that was raised was: which of the scanning probe microscopies would better be combined with synchrotron light? First of all, one AFM can always be used as an STM or EFM provided the tip is conductive. Thus the choice of using an AFM seems to leave space for the other techniques as well.

The question above becomes extremely important when it comes to detect, with the tip, an absorption edge for instance. As a matter of fact, the excitation of an atom may change the tunneling probability measured with an STM, or, using a different approach, the emitted charges, may in principle, be measured

with an EFM. But what does the AFM measure? Is there any change in the force or force gradient between tip and sample when one goes across an absorption edge? In the context of this thesis the atomic force microscopy was never used to probe an absorption edge. Rather the tip of the X-AFM was used to collect photoemitted electrons from the sample, which of course has nothing to do with the AFM itself.

When the sample is illuminated with X-rays it responds by ejecting photoelectrons. If an absorption edge is measured then we want to see how this response changes as a function of energy.

If the emitted charge is detected in the tunneling regime, such that only the current which has an exponential dependence on the tip-sample distance is measured then the lateral resolution expected is high [22]. Of course, the experimental scheme must be such that the electrons that are not tunneling are rejected. This can be done because the probability to detect directly photoemitted electrons does not evolve exponentially with the decrease of tip-sample distance and in principle can be neglected. In conclusion, STM may have a natural advantage relative to an AFM in what concerns lateral resolution.

When the X-AFM tip is used in parallel to detect the photo-emitted electrons there is no mechanism, as with tunneling regime, that localizes the measurement, thus high lateral resolution, i.e., compared to the tip apex radius, can only be achieved by isolating the tip down to its apex. Otherwise, all the photo-emitted electrons that eventually end up at the tip are measured. The lateral resolution is then strongly dependent on the X-ray beam size.

In Electrostatic Force Microscopy (EFM) one measures the attractive force between the tip apex and the sample due to the tip charge and its image on the sample. If we imagine the tip-sample as a capacitor like system, as is done in EFM [27, 32], then a force gradient exist between the two plates for a given charge Q. If the gap is filled with charges, then the force is no longer only due to Q but to $Q + Ne^-$ where N is an integer and e^- the charge of the electron. It is clear that in such a situation the measurement is intrinsically localized to the region below the tip, as is in the STM case. In such case one would be measuring a force gradient and this would be a real combination between synchrotron radiation and force microscopy (in its EFM variant). However, such approach was unfortunately never explored. Simply because it is difficult to have access to synchrotron light especially if it is to make a try!

It seems clear that any real combination of SPM techniques with synchrotron light offers intrinsic high lateral resolution.

The approach we have followed can be as powerful as a real SPM combination with intrinsic lateral resolution, and even easier to implement, as long as a special tip, used to localize the region where the electrons come from, could be developed.

1.3 General context

This thesis was entirely carried out at the surface science laboratory (SSL) of the ESRF. There was no particular connection between the SSL and a given beamline. Most of the experiments done and presented here were the result of official proposals.

The SSL is the laboratory where the X-AFM was developed. Everything was built from scratch and several versions of X-AFMs were done.

The first version of an X-AFM was a vacuum chamber version. This proved to be technically difficult not because of the vacuum itself, but due to other issues as the difficulty to see the sample with an optical microscope since the vacuum chamber was small and provided with only small windows. The very simple task of aligning the X-AFM tip with the beam was much more difficult at that time. Today we have gained know-how, thus we believe, and probably such approach would be feasible.

After the first vacuum AFM approach we followed a more practical one where simplicity and versatility were the keywords.

The wrist watch quartz tuning fork used in the construction of the X-AFM was also subject of study along this thesis since as we shall see its understanding is crucial to some of the results presented here. The second chapter is fully dedicated to it. Some details relative to the X-AFM as an AFM are presented in chapter three. In the fourth chapter will be described the experiments where AFM and synchrotron radiation are combined. This includes measurement of spectroscopies with the tip of the X-AFM and indentation of a SiGe particle while diffraction was measured.

Chapter 2

Theory of the Tuning fork

Contents

2.1 Introduction

Tuning forks were introduced in the context of SPM by Khaled Karrai [33]. In particular they were used for Scanning Near Field Optical microscopy (SNOM). Therein after, tuning forks have widely been used in the conception of home made atomic force microscopes [34, 35, 36, 37, 38, 39].

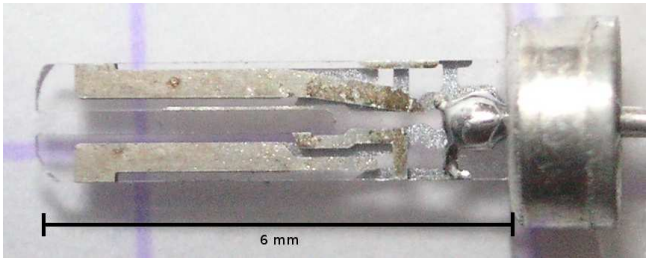

Figure 2.1: Picture of a crystal quartz tuning fork.

They have been the background all along the present thesis. For this reason we dedicate a chapter to the understanding of tuning forks. Hereinafter, we shall often refer to them simply as TF.

We shall start with a brief presentation of tuning forks and then, before entering in the specific details to the TF we shall make a quick review concerning the motion of a clamped beam. From this we will estimate the resonance frequency(ies) of the tuning fork. We will then construct the equivalent mass-spring system that will be used throughout this work. The very simple mass-spring model is compared to a more complex model of the tuning fork, to conclude that the basics of the dynamics of a tuning fork can be very well described by a very simple mass-spring model.

The ways to excite the TF and measure its motion will also be the subject of this chapter.

2.1.1 General aspects of the tuning fork

The TF's used here are the same as those used in wrist watches. They are crystal quartz.

The prongs of the tuning fork are clamped to a common body. They are coupled and vibrate symmetrically, i.e., without motion of the centre of mass. Mechanically they are no different from bigger versions commonly used to calibrate musical instruments.

The prongs' characteristics are given in the scheme of figure 2.2.

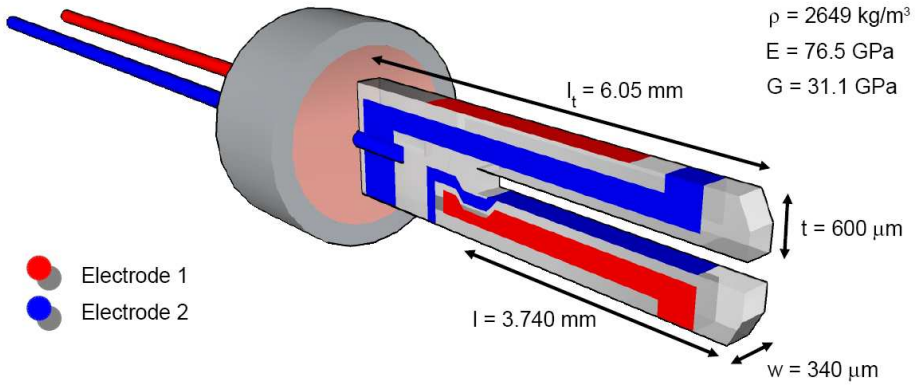

Figure 2.2: Tuning fork scheme and properties

Quartz has piezoelectric properties. The piezoelectric tensor relates polarization and stress in the material. Electric contacts deposited on the TF can be used to excite it or readout the magnitude of the stresses along certain directions. The stress is in turn related to the deflection as we shall see below.

The contacts have to be strategically positioned as determined by the polarizability tensor.

In the case of the crystals used here the contacts are placed along opposite planes in opposite prongs. This is illustrated in figure 2.2. The detected signal (i) is proportional to the amount of motion along opposite directions ($i \propto v_1 - v_2$) i.e., if both prongs move in phase and with the same amplitude the signal from one prong is canceled by the one coming from the other prong. Moreover, as determined by the polarizability tensor which depends on the symmetry of the crystal, only bending along certain directions will produce detectable signals.

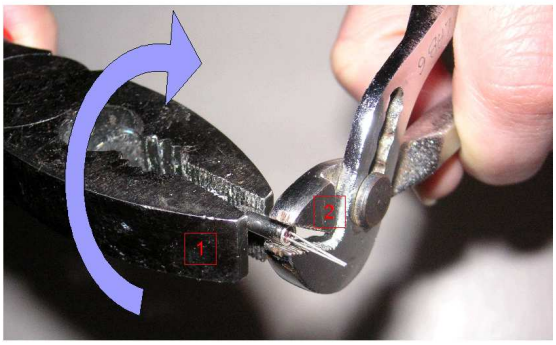

Figure 2.3: How to remove the TF from its shell: With pliers 1 and pliers two as in the picture. Then turn pliers 1 in such a way that the shell turns with it. Pliers 2 is not moving. The box turns tighten between pliers 2.

Make about ten half turns making sure that there will be static friction in pliers 1 and kinetic friction in pliers 2. Finally, pull out the TF by its contacts.

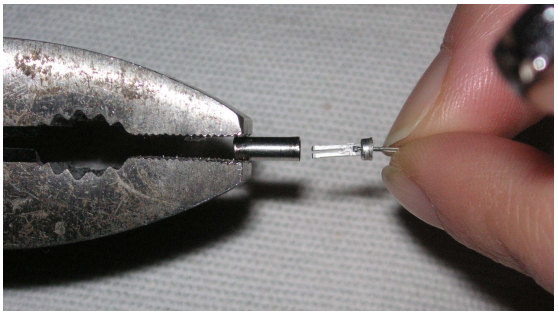

These oscillators when tuned to the resonance frequency have very high quality factors because the motions do not imply displacement of the centre of mass, resulting in very little coupling to the external world. Consequently, it matters little how the TF is connected to the external world. For their outstanding performance they are commonly used as frequency generators.

The TFs used here are meant to be integral part of an atomic force microscope. Unlike the oscillators usually used in this context - typically Si micro fabricated cantilevers; TFs have very high spring constant due to their dimensions. This fact has advantages and disadvantages that are discussed in the third chapter.

2.1.2 How to remove the TF from its shell

The following lines are just of practical importance, since the TF's are bought enveloped in little shells. The crystal is very fragile and breaks easily. The first challenge for a newcomer is to remove the TF from its shell without breaking it. It is the first question I was asked from students starting in the field.

One easy way of removing the TF from its shell is to use a pliers and squeeze the entrance of the shell until the cap of the shell breaks. This cap is the little cylinder seen in the scheme of figure 2.3 on the bottom picture close to the fingers. Breaking the cap is not a good move because it can be used to mechanically attach the TF and mechanically secures the electrodes.

Another way, preserving the cap, is to cut the cylinder around. The disadvantage is that it is time consuming and must be done very carefully.

A third way and very easy indeed, is to use two pliers. One to hold the TF

and use it to turn the shell inside a second pliers so that there is friction in this second pliers. After 7 to 12 turns the TF gently comes out. It takes about 10 seconds. This is explained more in detail in the caption of figure 2.3.

The TF is now ready to be mounted and give us his tune.

2.2 Bending Beams

2.2.1 Static bending of a beam due to shear force

Let us suppose a beam clamped at one end and free at the other end. Therefore at position $x = 0$ there is neither motion $u(0) = 0$ nor deflection $du/dx|_0 = 0$.

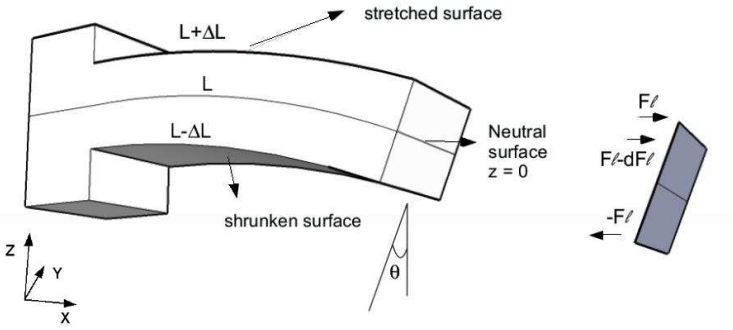

Figure 2.4: Clamped beam

Consider a force F acting on the extremity of the beam and perpendicular to it. As a result the beam will bend and be under stress. At each cross section of the beam a moment M will appear.

We refer to this moment M as bending moment and to the force F as shear force because it acts parallel to the bending, but note that at this point it is assumed no shear deformation.

This means that plane sections perpendicular to the neutral surface remain plane and perpendicular to the neutral surface. This is only true in approximation. It is a very good approximation for beams much longer than thicker, but becomes weak as the beam is short compared to its thickness.

We will consider deflections much smaller than the length of the beam so that the arc described by the beam is much smaller than 2π.

Furthermore, we will assume that there exists a neutral surface such that it only bends but does not elongate or shorten.

As a consequence of the bending the beam will elongate in one side and compress in the other. The elongation increases as we go away from the neutral surface toward the most elongated surface and vice-versa. The elongation at distance z from the neutral surface is $\Delta L = z \tan\theta$, which for small angles becomes:

$$\Delta L \approx z\theta \qquad \textit{and} \qquad \theta = \frac{L}{R}$$

Thus,

$$\Delta L = z\frac{L}{R} \tag{2.1}$$

the elongation at position x is related to the radius of curvature described by the neutral surface at that position. The more the beam is bent the smaller is the radius of curvature.

How much the beam will bend per applied force has to be related to the Young modulus E. (It also depends on the shear modulus, but we are assuming for simplicity that there is no shear.) The lower the Young's modulus E the greater the beam will bend for the same applied force, and also greater is the deformation ΔL. Simply from the definition of Young's modulus:

$$\frac{F_l}{A} = E\frac{\Delta L}{L}, \tag{2.2}$$

where F_l is the stress along the direction of the length of the beam, and increases as we go away form the neutral plane where it vanishes. Thus, to compute the bending moment we have to integrate. The deformation is related to the stress by the expression:

$$\frac{dF_l}{dA} = E\frac{z}{R}. \tag{2.3}$$

Where $dA = Wdz$ with W the width of the beam at position z. From the stress we can now compute the Bending Moment M acting on a cross section by calculating the integral $M = \int zdF_l$. From equation 2.3 we write:

$$M = \int \frac{E}{R}z^2 dA, \tag{2.4}$$

the quantity $\int z^2 dA$ is actually the moment of inertia I of the squared cross section with unit mass per unit area, or the area moment of inertia. So the Moment M comes equal to:

$$M = \frac{EI}{R}. \tag{2.5}$$

For a given momentum M the curvature of the beam is inversely proportional to the quantity EI. For this reason this quantity is often referred to as rigidity of the beam.

For small bending of the beam the curvature is approximately given by:

$$\frac{1}{R} \approx \frac{d^2u}{dx^2}. \tag{2.6}$$

Because action is equal to reaction at each section the beam will see the applied force F. Each section pushes on its neighbour as much as it is being pulled. In a similar way the sum of all the moments acting on each cross section must also vanish. Therefore the moment acting on each cross section must be given by:

$$M = F(L - x). \tag{2.7}$$

Finally, combining the three last equations to eliminate M and R we find:

$$\frac{d^2u}{dx^2} = \frac{F}{EI}(L - x). \tag{2.8}$$

By solving this differential equation, for the boundary conditions $u = 0$ and $du/dx = 0$ at position $x = 0$ we easily find:

$$u(L) = \frac{F}{EI}\frac{L^3}{3}, \tag{2.9}$$

from this we can calculate the spring constant k of the beam since $k = F/u$, we find that

$$k = \frac{3EI}{L^3}. \tag{2.10}$$

Spring constant of a rectangular beam

Consider a beam with rectangular cross section, like the prongs of the tuning forks used here. The dimensions are defined by the length L, width W and thickness T.

The moment of inertia for a cross section of the tuning fork is $WT^3/12$. If we multiply it by the Young's modulus we obtain the rigidity and consequently from 2.10 the spring constant for a TF prong is:

$$k = \frac{EWT^3}{4L^3} \tag{2.11}$$

It is worth noting that if shear is considered the spring constant would be slightly smaller. Simply because for the same bending there would be less stress in each plane as they would slight past each other. Suppose a rubber with flat ends. After bending the ends are no longer flat. If the rubber would have a lower Poisson's ratio this deformation would be smaller and the force needed to bend it larger.

Tuning Fork prongs' spring constant

Each prong of the tuning fork can deflect either along the direction of their width W or along the direction of their thickness T. The last being the most common way. We shall refer to deflections along the direction of their width as lower modes u_L and along their thickness as higher modes u_H, corresponding to lower and higher resonance frequencies accordingly and will denote them by the subscript L and H.

Depending on the direction considered we must interchange W with T in equation 2.11:

$$k_H = \left(\frac{T}{W}\right)^2 k_L \tag{2.12}$$

The static spring constants for these two deflections are:

k_H	=	26,634 N/m
k_L	=	8,553 N/m

The dimension of the TF prongs and the young modulus for quartz are given in figure 2.2.

2.2.2 Bending waves' equation

In order to obtain the dynamical properties of the cantilever, we need first to establish the equation of motion for an infinitesimal thin slice dx of the beam. Newton's second law applied to the element gives:

$$\rho A dx \ddot{u} = dF(x), \tag{2.13}$$

A is the sectional area of the beam and ρ the density.

From previous chapter we know that the bending produces a moment which according to 2.5 and 2.6 is given by:

$$M(x) = EI\frac{d^2u}{dx^2} \tag{2.14}$$

In the previous section when we investigated static bending we had an equilibrium between moment M and shear force F; here F is due to the acceleration.

$$F + \frac{dM}{dx} = 0. \tag{2.15}$$

The first term on the left is the force due to translation and the second term is the force due to bending. In a dynamic situation we also have angular acceleration of the section which spins around an axis perpendicular to the deflection and also contributes to balance the forces and momentums acting on a section. In other words each section exhibits both translation motion (eq.2.13) and rotatory motion. Though rotatory motion is often neglected, we shall further discuss this below.

Differentiating equation 2.15, replacing M from equation 2.14 and dF from 2.13 we obtain an equation for the deflection u:

$$\frac{\partial^2 u}{\partial t^2} + \frac{EI}{\rho A}\frac{\partial^4 u}{\partial x^4} = 0. \tag{2.16}$$

This is the so called Euler-Bernoulli beam equation and is obtained by assuming pure bending: only Young modulus intervenes, shear modulus is assumed to be infinite and rotatory inertia has also been neglected.

Harmonic bending waves in a beam

On the analysis of solutions to equation 2.16 we look now to those having a periodic time dependence:

$$u = u_0 exp(i\omega_n t), \tag{2.17}$$

and satisfying the boundary conditions for a free end. The bending moment and shear force are 0 for a free end:

$$\frac{d^2u}{dx^2}_{(x=L)} = 0, \qquad \frac{d^3u}{dx^3}_{(x=L)} = 0 \tag{2.18}$$

If we replace equation 2.17 in equation 2.16 we obtain the ordinary differential equation:

$$u = l_n^4\frac{d^4u}{dx^4} \tag{2.19}$$

where:

$$l_n^4 = \frac{1}{\omega_n^2}\frac{EI}{\rho A} \tag{2.20}$$

The general solution of equation 2.19 with the corresponding boundary conditions leads to the eigen-value equation:

$$\cos(L/l_n)\cosh(L/l_n) + 1 = 0 \tag{2.21}$$

From equation 2.20 and defining the constant $\alpha_n = (L/l_n)^2$ we calculate the resonance frequency:

$$\omega_n = \alpha_n\sqrt{\frac{EI}{\rho AL}} \tag{2.22}$$

This equation is valid for any beam of arbitrary cross section having a plane of symmetry which intersects the longitudinal axis, as long as $L >> T$.

It is a very good approximation for beams that are much longer than thicker (because bending is the easiest) and when only the first harmonic mode is considered because of the longer wavelength. For short wavelengths it becomes like having a small beam, then shear deformation becomes considerably important and lower the rigidity of the beam. Rotatory inertia also has a greater effect on the higher modes due to their higher frequency.

Neglecting both shear and rotatory inertia will in general result in the overestimation of the resonance frequencies, in particular of the higher modes. This overestimation will become larger as the beam is shorter.

Effective spring-mass model

Rearranging equation 2.22 using equation 2.11 to explicit ω_n in terms of the static spring constant k and mass m noticing that $m = \rho AL$. We obtain the following relationship:

$$\omega_n = \alpha_n\sqrt{\frac{k}{3m}} \tag{2.23}$$

For the fundamental mode it is easy to think in terms of an effective mass:

$$m^* = \frac{3m}{\alpha_n^2} = 0.242674m \tag{2.24}$$

where α_n^2 is computed from table 2.1. In this way the resonance frequency of the fundamental mode is given by:

$$\omega_0 = \sqrt{k/m^*} \tag{2.25}$$

which we identify with the resonance frequency of a spring-mass system.

The effective mass is obviously the same for both the lower and higher modes of the tuning fork:

$$m^* = 492 \times 10^{-6} kg$$

Resonance frequencies of one tuning fork prong

If we think about the two possibilities for deflecting a prong, along their thickness or along their width, then, using equation 2.22 we see that ω_l and ω_t are related through the expression:

$$\omega_H = \frac{T}{W}\omega_L \tag{2.26}$$

The values of l_n which satisfy equation 2.22 are the same for both modes.

The fundamental and the three following harmonic values of L/l_n and the respective resonance frequencies for both modes are given in the table below:

α_n	f_{Hn} (kHz)	f_{Ln} (kHz)
3.5160	37.039	20.989
22.034	232.119	131.536
61.697	649.940	368.306
120.90	1273.6	721.732

Table 2.1: Frequencies of one TF prong (Euller-Bernoulli).

However, it is interesting to note that these frequencies do not correspond to the experimentally observed TF frequencies. In particular those of the fundamental modes. Actually $f_H = 2^{15}Hz = 32768Hz$ and $f_L = 17873Hz$. It is worth remembering that neglecting both shear motion and rotatory inertia contribute, in general to obtain higher frequencies, because this leads to an overestimation of the stiffness and a underestimation of the effective mass.

Then, either the Euler-Bernoulli beam is not a good approximation to describe the frequencies of the tuning fork or the TF cannot simply be seen as characterized by the resonance frequencies of its prongs, as is usually done.

Therefore before entering in a different way of modeling the frequencies of the fork it is worth understanding the effects of neglecting rotatory inertia and shear motion.

2.2.3 Effect of rotatory inertia and shear

Effect of rotatory inertia

Consider a section which spins around an axis perpendicular to the deflection. The moment of inertia of this section is $I_s = \rho I dx$. If α is the angular acceleration of this section then a torque τ appears:

$$\tau = \alpha I_s \tag{2.27}$$

This acceleration is, of course, equal to the angular acceleration of the neutral surface. For small angles the angle is approximately equal to the slope, and the slope is given by $\partial u/\partial x$. Hence, we conclude that the angular acceleration is given by

$$\alpha = \frac{\partial^2 u}{\partial t^2}\frac{\partial u}{\partial x} = \frac{\partial^3 u}{\partial t^2 \partial x}. \tag{2.28}$$

Thus the force involved is:

$$F_r = \frac{\partial M_r}{\partial x} = \frac{\partial^4 u}{\partial t^2 \partial x^2} I_s. \tag{2.29}$$

This term must be inserted in equation 2.16 to include rotatory inertia. This will give accurate resonance frequencies even when higher modes are considered, as long as the beam is much larger in length than in thickness.

Shear motion

If we consider only shear then there is an angle θ_s bigger than zero even though there is no bending. The result of introducing shear is that the angle of each section is now larger for the same bending., i.e, with shear the sections are no longer perpendicular to the neutral axis. Looking at the definition of shear modulus G:

$$u = \frac{xF_s}{GA} \Leftrightarrow \theta_s = \frac{F_s}{\kappa GA}, \tag{2.30}$$

where κ is a numerical factor depending on the shape of the cross section and θ_s is the angle due to shear deformation only. This angle must be equal to the total angle minus the angle due to bending. Because the angle due to both bending and shear is given by $\theta_{bs} = \partial u/\partial x$, then:

$$\theta_s = \frac{\partial u}{\partial x} - \theta_b. \tag{2.31}$$

The total torque acting on a section due to both bending and shear is given by:

$$\tau_{bs} = F_s dx - \frac{\partial M}{\partial x} dx. \tag{2.32}$$

Using equation 2.30 and 2.5,

$$\tau_{bs} = \kappa GA\theta_s dx - EI\frac{\partial^2 \theta_b}{\partial x}. \tag{2.33}$$

Of course, here again, we must have $\tau_{bs} = \alpha_{bs} I_s$, with α_{bs} the angular acceleration of the section due to both bending and shear elastic deformations. At variant with previous assumptions here we do not approximate the angle by the slope. The final equation for the rotation of an element is:

$$EI\frac{\partial^2 \theta_b}{\partial x^2} + \kappa GA\left(\frac{\partial u}{\partial x} - \theta_b\right) = I\rho\frac{\partial^2 \theta_b}{\partial x^2}. \tag{2.34}$$

The vertical translation of an element with mass $dm = \rho A dx$ due to the shear force is:

$$\frac{\partial F_s}{\partial x} dx = \rho A dx \frac{\partial^2 u}{\partial t^2} \tag{2.35}$$

and by replacing F_s given in equation 2.30 and θ_s in equation 2.31 it is obtained:

$$\rho A\frac{\partial^2 u}{\partial t^2} - \kappa GA\left(\frac{\partial^2 u}{\partial x^2} - \frac{\partial \theta_b}{dx}\right) = 0 \tag{2.36}$$

The final equation comes as the solution of the system of equations 2.34 and 2.36, where by eliminating θ_b:

$$EI\frac{\partial^4 u}{\partial x^4} + \rho A\frac{\partial^2 u}{\partial t^2} - \rho I\left(1 + \frac{E}{\kappa G}\right)\frac{\partial^4 u}{\partial x^2 \partial t^2} + \rho^2 \frac{I}{\kappa G}\frac{\partial^4 u}{\partial t^4} = 0 \tag{2.37}$$

This is the so called Timoshenko beam equation [40]. If only the two first terms are considered then it is identical to the Euler-Bernoulli beam equation.

Bending waves revisited

If we consider periodic time dependence like in the previous section we obtain an equation where the frequency appears explicitly:

$$\omega^2 \rho A\left(1 - \frac{\rho I}{A\kappa G}\omega^2\right) = EI\frac{\partial^4 u}{\partial x^4} + \rho I\omega^2\left(1 + \frac{E}{\kappa G}\right)\frac{\partial^2 u}{\partial x^2} \tag{2.38}$$

It can be seen that the second term on the left is negligible compared to one:

$$\frac{\rho I}{AG}\omega^2 \approx \frac{2649 \times 6 \times 10^{-15}}{200 \times 10^9 \times 30 \times 10^9} \times (200 \times 10^3)^2 = 1.05 \times 10^{-4}$$

This term is only relevant for very high frequencies. By neglecting it, it is obtained:

$$\omega^2 = \frac{EI}{\rho A}\frac{u^{(4)}}{1 - \rho I b u^{(2)}} \tag{2.39}$$

Where the exponents in u denote derivatives, and $b = (1 + E/\kappa G)$.

The solution to this equation is not straightforward as in the Euler-Bernoulli beam. We note however that the solution must satisfy the same boundary conditions as in that case. The solution has to be such that the right term of equation 2.39 is a constant. This is straightforward if the solution only involves therms of the type $A\sin\omega t$ or $A\sinh\omega t$, but not altogether. To satisfy the boundary equations both hyperbolic and non hyperbolic therms are needed, such as previously in the Euler-Bernoulli beam equation. But unlike in that case the argument of the hyperbolic functions is not the same as in the non hyperbolic functions. This makes it more complicated, though it leads to a similar (more complicated) eigenvalue equation.

After some pure mathematical considerations, the solution to equation 2.39 is:

$$\omega_n = \alpha_n\sqrt{\frac{EI}{\rho A L^4}} \tag{2.40}$$

$$\alpha_n = \left(\frac{L}{l_n}\right)^2 \times \sqrt{\frac{Al_n^2}{Al_n^2 + Ib}} \tag{2.41}$$

Where α_n has the same meaning as in the Euler-Bernoulli case, but do not attains the same values. Realize that with an infinite shear modulus G, then $b = 1$. So for long enough beams (l_n increases with L) the second square root

in equation 2.40 becomes equal to one and the solution is identical to that of the Euler-Bernoulli beam.

Considering a prong with the dimensions of those of the TF the values for the first four α_n are given in table 2.2.

Higher mode		Lower mode	
L/l_n	f_n (kHz)	L/l_n	f_n (kHz)
3.5325	37.033	1.8765	20.973
22.237	228.643	4.7025	130.800
62.693	619.622	7.875	362.259
123.48	1156.12	11.036	697.714

Table 2.2: Frequencies of one TF prong (Timoshenko beam).

This table is to be compared with table 2.1. Notice that unlike in the Euler-Bernoulli beam case the values in the table are valid only for the prongs of the TF. We see that for the higher harmonics the frequencies are several kHz lower: 5kHz for the 2nd harmonic and 147 kHz for the 4th harmonic. However, for the fundamental modes the difference is meaningless and lies within the experimental error associated with the measurement of the prongs' dimensions.

The conclusion we make from this is that the resonance frequencies of the TF are not equal to the resonance frequencies of the individual prongs as is usually considered.

2.3 Two identical coupled oscillators

In the last section we have obtained what is expected for the dynamics of a beam like a TF prong clamped at one of its ends. The real TF as two prongs and both are clamped onto the same common body. If the prongs are equal both have the same resonance frequencies. In this case when they resonate there will be mechanical waves inside the material which are coherent and can interfere either destructively or constructively depending on their phases. Even if they are not equal, at some point, both prongs will be excited at the same frequency and coherent mechanical waves will exist and interfere. The motions of each prongs are therefore coupled each other. This can be very well taken into account if we assume that the prongs are not really clamped, and they are indeed not, i.e., they can exhibit little motions at their basis.

Let us imagine we force the prongs apart: the u shape deforms: - the u opens; as a consequence a restoring force acts on both prongs to close the u and vice versa. This restoring force is in phase with the symmetric motion of the prongs, i.e., when they go apart the force is to close u, when they move toward each other the force is to open u. We can imagine a spring k_c coupling oscillator 1 (k_1, m_1) and oscillator 2 (k_2, m_2) as depicted in figure 2.5.

This depiction is valid for the two orthogonal symmetric modes of the TF. By symmetric we mean that there is no displacement of the centre of mass, the prongs move with a phase difference of π relative to each other. The one having higher individual resonance frequency moves with phase difference of $\pi/2$ and the other with phase difference of $-\pi/2$ relative to the body to each they are anchored.

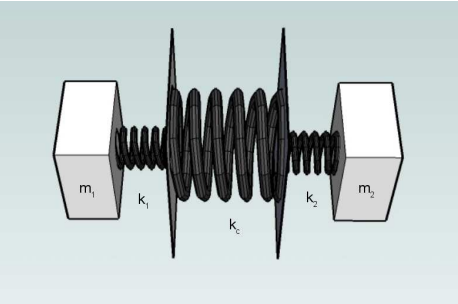

Figure 2.5: Two identical coupled oscillators. Here, (m_i, k_i) represents prong i and k_c the coupling between the two prongs.

The difference between the two symmetric modes (higher mode and lower mode), is in the stiffness of each prong and coupling. The coupling between the prongs is in both cases larger than the stiffness of the individual prongs.

If the spring constant of the element coupling the two prongs would be smaller than that of the individual prongs then we would have a system that looked pretty much like the tweezers we find in our labs. If we hold a tweezers at the basis and then close and release the prongs we observe a motion of the prongs dominated by the stiffness of the u rather than that of the prongs. In the case of a TF the natural resonance is dominated by the stiffness of the prongs but both prongs communicate trough the u.

This u with both prongs attached is then in turn coupled to the body. We shall discuss this later on.

For the moment let us neglect the interaction of the prongs with the body.

2.3.1 Single mass-spring equivalent of a tuning fork

For the particular case depicted in figure 2.5 one can think in terms of the reduced mass:

$$m_r = \frac{m_1 m_2}{m_1 + m_2} \tag{2.42}$$

And reduced stiffness:

$$k_r = \frac{k_1 k_c k_2}{k_1 k_c + k_2 k_c + k_1 k_2} \tag{2.43}$$

If there is damping associated to the motion of each mass such that γ_1 and γ_2 are the damping coefficients of prong one and two, then we find:

$$\gamma_r = \frac{\gamma_1 \gamma_2}{\gamma_1 + \gamma_2}, \tag{2.44}$$

Here we have neglected dissipation associated with k_c.
We can now write the reduced equation of motion:

$$F_r = m_r \ddot{x}_r + k_r x_r + \gamma_r \dot{x}_r \tag{2.45}$$

Where F_r, m_r, k_r, and γ_r are respectively the effective force, the reduced mass, reduced spring constant and reduced damping coefficient. We will discuss F_r in a paragraph related to the excitation of the TF. From the familiar equation

2.45 it is easy to deduct that the TF will exhibit resonant behaviour when the excitation has a frequency given by:

$$\omega = \sqrt{\frac{k_r}{m_r}} \tag{2.46}$$

The width of the Lorentzian response is in turn given by:

$$\gamma = \frac{\gamma_r}{m_r} \tag{2.47}$$

The TF can be seen as mass-spring system with mass, spring constant and damping coefficient given respectively by the first three equations in this section.

Resonance frequencies of a tuning fork

To model the resonance frequencies of the tuning fork it will be assumed k_1 and k_2 are given by equation 2.11. Further it is assumed that m_1 and m_2 are given by equation 2.23. It is necessary to know k_c. This value has not been theoretically estimated. However, it can be estimated from the experimentally obtained resonance frequencies.

For the fundamental lower mode (parallel to the TF's width; its smaller dimension) and higher mode (along its thickness) the resonance frequencies are: 17.87 kHz and 32.768 kHz. Using equation 2.46 we find k_{Hr} and k_{Lr}, and from equation 2.43 we can find the coupling constants k_{Hc} and k_{Lc}. This is given in table 2.3. We note that for a balanced tuning fork $m_r = m_f/2$, where m_f is the effective mass of one TF prong.

	k_r (kN/m)	k_c (kN/m)	m_r (μ g)	f_0 (kHz)
Lower mode	3.101	11.289	246	32.768
Higher mode	10.422	47.942	246	17.87

Table 2.3: Effective spring-mass constants for a tuning fork

It will be shown that the actual value of k_c or of the individual prongs is actually not relevant for most of the purposes. This is, if we accept a model like that of figure 2.6 then the relevant constant is of course k_r.

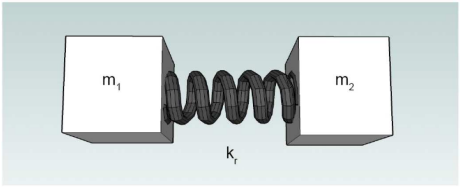

Figure 2.6: Reduced scheme of a tuning fork.

Consequently, it does not matter whether the stiffness of the individual prongs is a bit lower or higher, as long as we accept equations 2.46, 2.42 and 2.23. If we accept k_r has having the physical meaning we want to express and illustrate in figure 2.6, then k_r its value can be determined experimentally.

2.3.2 Some experimental results

The model and equations derived here above will now be submit to a certain number of questions, in order to check the validity of the model.

Frequency changes as masses are added to the TF

In a first proposed experiment, let us carefully break one prong of a TF. The prong was then roughly divided in two halves. Each half was glued onto the prongs of a new TF prong. Now, given that the effective mass is about 1/4 of the mass in an entire prong (equation 2.24), the new effective mass is 3 times higher. Since the same mass was added to each one of the TF's prongs the reduced mass is also 3 times higher. Consequently, both modes are expected to have frequencies that are $1/\sqrt{3}$ of their original frequencies. This is:

$$F_H = \frac{32768}{\sqrt{3}} = 18.919kHz$$

$$F_L = \frac{17800}{\sqrt{3}} = 10.277kHz$$

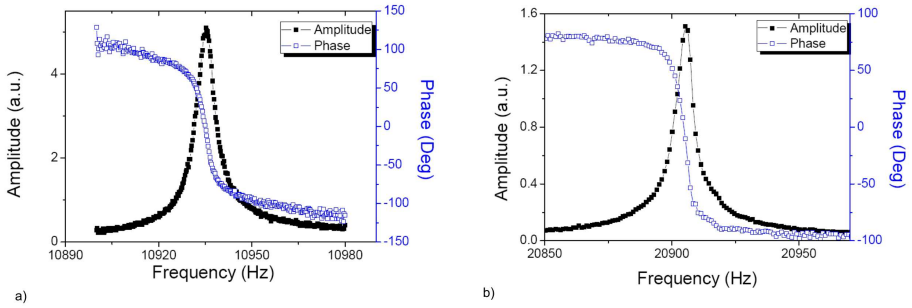

Figure 2.7: Experimental resonance curves of a tuning fork with half prongs glued on.

The resonances obtained can be seen in figure 2.7. The corresponding values where 20910Hz and 10930Hz.

There is some discrepancy for the higher mode while the lower mode is in very good agreement with the predicted value. As a matter of fact, this discrepancy is expected since when something is glued on one prong then its stiffness increases. This increase leads to an increase of the resonance frequencies.

This increase in the stiffness k_r must be taken into account if accurate measurements are to be taken.

The resonance frequency would have been well predicted if k_r was assumed 5% larger.

An infinite mass glued on one prong

A limiting case we may analyse: what happens if in one prong we glue an extremely heavy or an infinite mass?

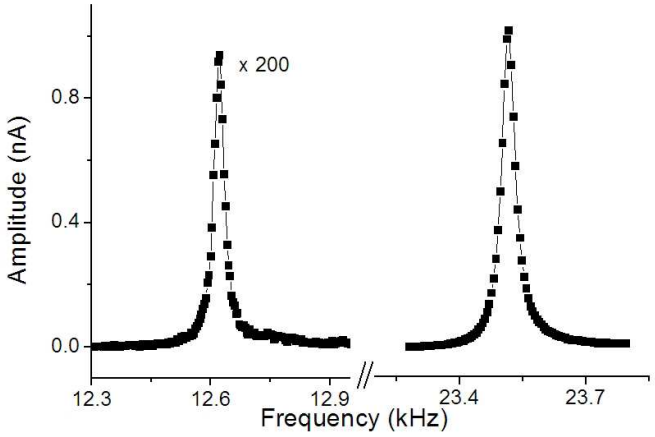

Figure 2.8: Experimental resonance curves of a tuning fork with an infinite mass glued on (see picture in the beginning of this chapter).

In this case the reduced mass becomes equal to the effective mass of the free prong. Whence it is twice the normal reduced mass. So according to equation 2.46 a peak is expected to appear at $f = f_0/\sqrt{2}$. For the higher mode this is 23.2 kHz.

As can be seen from figure 2.8 the actual resonance frequency was 23.4 kHz, instead of the 23.2 kHz and 12.65 kHz instead of 12.59 kHz. We consider this a good agreement because again there is an increase of k_r.

To further emphasize the agreement between model and experimental data, we note that if one prong is shorter by about 100 μm (which is much less than the length over which the gluing took place), then the new reduced stiffness is higher by about 3%.

This means that when we glue something on one prong, a tip for instance, the reduced stiffness k_r increases by 3% to 5%.

More experimental results will be presented latter.

2.3.3 Frequency shift of an interacting tuning fork

It is useful to consider one prong of the fork interacting with the sample or put in better words the tuning fork interacting with the sample. This is illustrated in figure 2.9.

We are interested to know what is the resonance frequency of the system depicted in figure 2.9.

For this we write for each mass the Laplace transforms of the equations of motion:

$$\begin{aligned} m_1 x_1 s^2 &= F - (k_r + \gamma_r s)(x_1 - x_2) - k_i x_1 - \gamma_i x_1 s - k_{cm}(x_{cm} - x_b) \\ m_2 x_2 s^2 &= -F - (k_r - \gamma_r)(x_2 - x_1)s - k_{cm}(x_{cm} - x_b) \end{aligned} \tag{2.48}$$

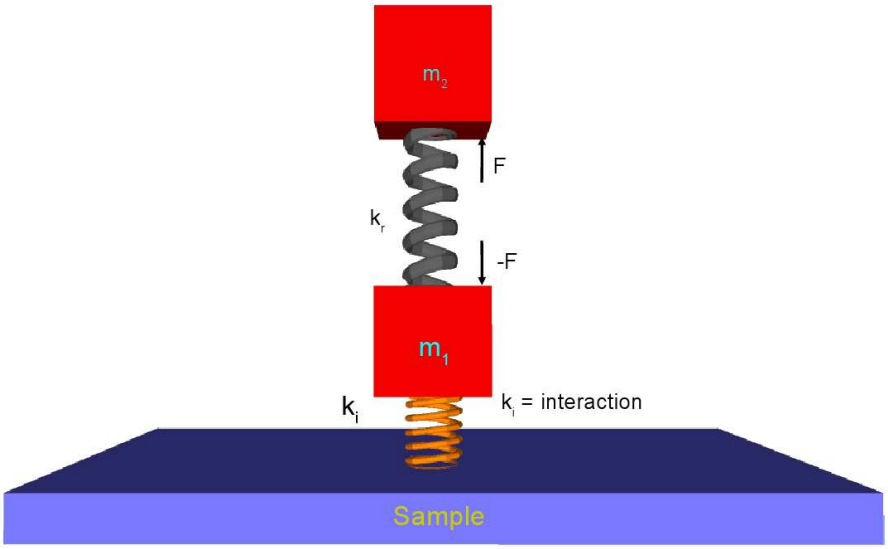

Figure 2.9: Schematic representation of a TF interacting with the sample.

where s is the complex transformed variable, and $k_{cm}(x_{cm} - x_b)$ is a restoring force proportional to the position of the centre of mass relative to the position of the body x_b, where by body we mean the mass to which both prongs of the fork are attached. Any motion of the centre of mass results in a force applied to the TF body. F is the force acting on the masses, k_i is the interaction force gradient.

The system of equation has to be solved in order to find $x = (x_1 - x_2)$ giving the relative displacement of mass 1 toward mass 2. To be remembered that the electrodes are strategically optimized so that the measured current i is proportional to the symmetric displacement of the prongs ($i \propto x$). The solution is rather complicated. However, it has a much simpler solution in the limit where $k_{cm} \to \infty$:

$$X(s) \equiv x_1 - x_2, \; k_{cm} \to \infty \tag{2.49}$$

We will refer to X(s) as the simplified transfer function of a TF. The solution when the limit above is taken is:

$$X(s) = \frac{F + (ki + (m_1 - m_2)s^2)x_b}{k_{ri} + \gamma_{ri}s + m_r s^2} \tag{2.50}$$

with:

$$\epsilon = \frac{1}{2}\frac{m_2}{m_1 + m_2} \tag{2.51}$$

Though it is true that there may be motion of the centre of mass but this is an asymmetric mode that we are neglecting for the time being. The limit means that the energy balance of the symmetric mode is in such a way that it tends to minimize motion of the centre of mass. From the simplified transfer equation

we can readily see that the TF can be excited either trough F or by driving the body ($x_b \neq 0$). This may be directly associated to electric excitation (F) or mechanic excitation (x_b).

We note that equation 2.50 is equivalent to equation 2.45 with modified stiffness and damping coefficient:

$$k_{ri} = k_r + \epsilon k_i \tag{2.52}$$

and

$$\gamma_{ri} = \gamma_r + \epsilon \gamma_i \tag{2.53}$$

The reduced mass remains the same with or without interactions.

Hence, the system will exhibit resonant behaviour when:

$$\omega_i = \sqrt{\frac{k_{ri}}{m_r}} \tag{2.54}$$

This description is most of what is needed to understand the dynamics of this (and its orthogonal) particular mode of the tuning fork in the context of its use in atomic force microscopy.

2.3.4 Coupling the two prongs with the external world

In this part we want to show that a more realistic description of the tuning fork coupling with the external world leads to the same conclusions as those taken in the previous section.

The idea is to emphasize that even if the prongs are coupled in a more reasonable way than simply by a term ($k_{cm}x_{cm}$), as was done when we calculated the simplified transfer function X(s) of the TF (2.48), still the same results are obtained approximately.

The two prongs of the tuning fork are attached to a third mass that can also vibrate and in particular exhibit resonant behaviour. This mass is what we refer to as body of the TF and denote it by the index b. Whence, its deflection is given by x_b. The body is in turn connected to a fixed reference frame. The point of connection is at position x_0.

We note that the tuning fork is not clamped. If we push the tuning fork we can easily see that it moves, there is a certain stiffness (k_b) associated to this that depends on the particular set up. In our case, because the tuning fork cap is conserved (see figure 2.3) this stiffness depends only on the stiffness of the TF electrodes.

If the vibration of the body is not negligible then this point of contact might be a path for energy loss. However, this will happen only if the TF's prongs are substantially different. Then there will be motion of the TF's centre of mass and this motion will couple to the body resulting in a motion of the body relative to the point at which it is fixed.

The damping of the body motion, occurs mainly at this point of contact.

To account for the motion of the body we write the equation of motions for each individual mass and an equation which couples the TF body with the external world:

$$\begin{aligned} m_1 x_1 s^2 &= F - k_r(x_1 - x_2) - \gamma_r(x_1 - x_2)s - k_i x_1 - \gamma_i x_1 s - k_{cm}(x_{cm} - x_b) \\ m_2 x_2 s^2 &= -F - k_r(x_2 - x_1) - \gamma_r(x_2 - x_1)s - k_{cm}(x_{cm} - x_b) \\ m_b x_b s^2 &= -k_b(x_b - x_0) - \gamma_b(x_b - x_0)s - 2k_{cm}(x_b - x_{cm}) \end{aligned} \tag{2.55}$$

Comparison with the *simplified transfer function of a TF* (eq.2.50).

The system of equations 2.55 was solved for each mass. The individual stiffness and masses used for each prong were chosen in agreement with the Euler-Bernoulli beam discussed before.

The coupling between the prongs was adjusted to give the correct resonance frequencies, as discussed in section: *Two identical coupled oscillators.*

For the illustration k_b we have used a stiffness of $10kN/m$. The calculations showed that this value only influences the behaviour of the symmetric peak when $k_b < 10k_r$. If $k_b >> k_r$, then solving the equations above or using the simplified transfer function of the TF is the same. However, in that case the description made here is too simple, as other modes of the fork need to be considered.

The effective mass of the body m_b was assumed to be equal to the total mass of the TF.

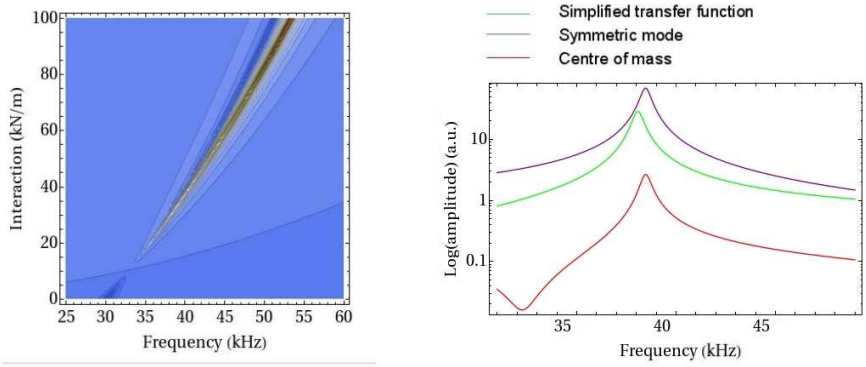

Figure 2.10: Right: equation 2.50 subtracted from the solution to the system of equations above (eq. 2.55). The two peaks superimpose up to resonance frequencies of 40kHz, then a difference between them is visible. The simplified transfer function predicts slightly lower resonance frequencies. Left: calculated resonance frequencies for a given interaction: it is shown the result obtained using the simplified transfer function (green), and in purple and red the resonance frequency of the symmetric peak and the motion of the centre of mass respectively, calculated using the system of equations above.

A comparison between the resonance frequencies of the fork calculated using the system of equations above 2.55 and equation 2.50 is shown in figure 2.10. Both models predict pretty much the same evolution of the resonance frequencies with the interaction force gradient. However, the amplitudes are substantially different. All the parameters that enter both the simplified transfer function and the system of equations are identical.

Concerning the use of the symmetric modes of the tuning fork in the context of AFM, where the interactions are very small, thus produce frequency shifts of only few Hz, the simplified transfer function (equation 2.50) is for all purposes a description that, we believe, is accurate.

Effect of cutting bits of prongs to the tuning fork

In this experiment we cut bits of the prongs in successive steps, taking at each time a resonance curve. In each step about $100\mu m$ of prong is cut. Three cuts are performed to the first prong and four cuts to the second. The final length of each prongs is measured. The result together with the simulation is shown in figure 2.11.

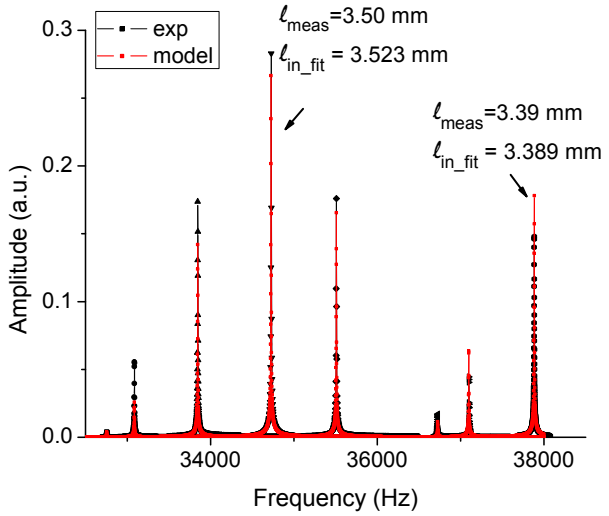

Figure 2.11: Resonance curves showing the evolution of the resonance frequency for different prong lengths. The length is adjusted to fit the data. The adjusted length is then compared to the measured length.

The length of the prongs was adjusted to better fit the experimental data. The adjusted lengths, corresponding to the final length of the prongs, are compared to the final experimental lengths. The values used and those measured are shown in figure 2.11. No other parameter was adjusted. The amplitude naturally goes up and down as a function of the symmetry of the TF, as predicted already by 2.50. The quality factor is nearly the same for all the curves, its total change is less than 5%. The resonance curves of the lower symmetric modes where also measured and the result obtained identical.

2.4 Excitation and signal detection

2.4.1 Excitation

There are at least four possible ways of exciting the tuning fork.

1. It can be excited mechanically vibrating it with an external source
2. Or acoustically; not if vacuum is required
3. It can directly be electrically excited
4. Or electromagnetically excited. The contacts' geometry is suitable for detection of electromagnetic fields.

Actually due to these many possibilities of exciting the tuning fork attention should be paid to how the excitation is done because it may happen that the TF is being excited simultaneously in two competing ways. These multiple excitations can interfere and change the shape of the Lorentzian response in some particular cases. This is particularly important when we are interested in the lower modes of the tuning fork for which the stress does not converts into charge.

There is no particular reason why one should choose one or the other way but they enter the equations of motion in different ways. There are of course, different advantages and disadvantages between them.

Mechanic excitation

The TF can be mechanically driven by shaking the point at which the TF is connected. This appears in the simplified transfer function of the TF (X(s)) 2.50 and in the system of equations 2.55 trough the terms x_b and x_0 respectively.

This excitation is non null only when the motion of the prongs implies motion of the centre of mass, i.e, if the prongs are not symmetric. Indeed, we have observed that as the prongs are less symmetric this type of excitation becomes much more effective. We have seen differences larger then two orders of magnitudes in the amplitudes of TFs driven by the same excitation, but with different prong symmetries.

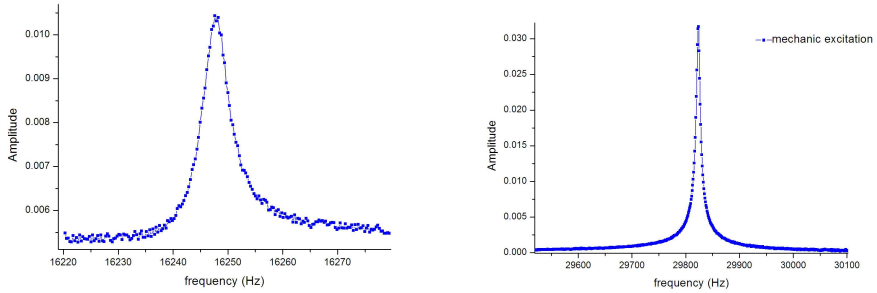

Figure 2.12: TF mechanically excited. The current is measured as the output with a transimpedance amplifier. On the left it is shown the lower mode and on the right the higher mode of TF (vibrations along its with and thickness respectively).

We have seen, perhaps many times, somebody exciting a tuning fork by tapping with one of its prongs into something. This mechanic excitation is very asymmetric and is very suitable for the excitation of a TF. In practice we

excite both prongs in the same way and then some asymmetry in the prongs is necessary - slight difference in mass for example.

It is worth mentioning that this type of excitation was the most used during this thesis.

Acoustic Excitation

Acoustic excitation can have symmetric and asymmetric components depending on the geometry of the setup i.e., due to the rather large wavelength of this waves ($\lambda \approx 11mm$) it is possible to position the nodes of the wave so as to excite each prong with an almost arbitrary phase.

This type of excitation was used when we wanted very small oscillation amplitudes of the tuning fork, i.e 10 pm for instance.

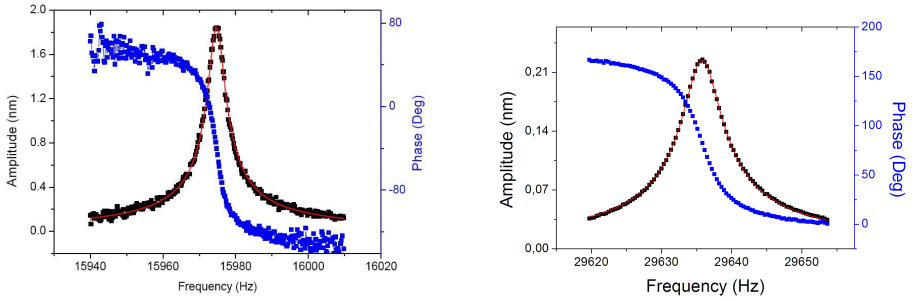

Figure 2.13: Lower (left) and higher (right) modes of the TF acoustically excited. The current is measured at the output of a transimpedance amplifier.

The exciter was a piezoelectric material positioned in air at few cm from the TF. The main problem is that because signals on the order of hundreds of mV are used, the TF may see the electromagnetic field and this can distort the resonance curve. Thus a proper shielding is required.

An issue of this type of excitation is that there may be small drifts in the amplitude of excitation with time, but also as a function of the distance between a sample and the TF.

Electrical excitation

The TF can easily be electrically excited through the electrical contacts deposited on the prongs. Unlike mechanic excitation the TF can be perfectly symmetric because the excitation is asymmetric. This is due to the strategic positions of the electric contacts on the TF which are in opposite planes of opposite prongs.

This force appears as the term F in the system of equations and in the simplified transfer function (equ. 2.50). It is assumed that the contacts are equal in both prongs.

This excitation has one disadvantage compared to mechanic excitation. The electric contacts on the tuning fork act as a capacitance with large plates and the dielectric constant of quartz. Therefore if a voltage is applied, a current i_c runs trough this capacitance independently of the fork being at resonance or not. Eventually when the TF resonates, due to the stress and piezoelectricity

a current i_{osc} is generated. Both currents add to produce the resulting current $i = i_c + i_{osc}$. The phase of it depends on the phase of the individual currents and lead to distortion of the resonance curve.

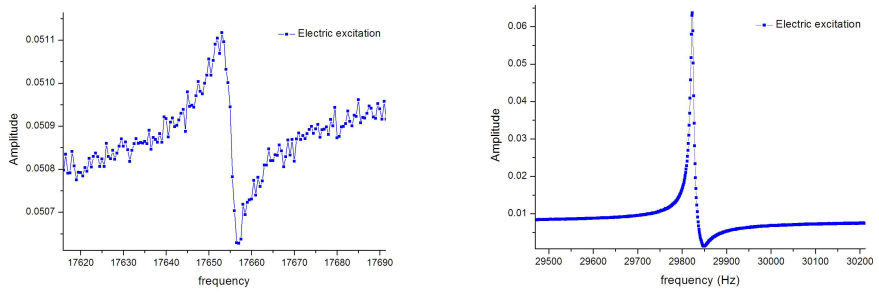

Figure 2.14: Lower and higher modes of the TF electrically excited. The current is measured at the output of a transimpedance amplifier. It is well visible the effect due to the stray capacitance, i.e, the contacts on the TF.

To compensate this, particular electric circuitry is needed. The compensation is usually done by injecting in the circuit a current which is equal to i_c in intensity but opposite in phase so that the total current is actually given by i_{osc}.

The main advantage of this type of excitation is the fact that it is applied directly on the prongs and is an asymmetric drive. It may as well excite modes other then the asymmetric ones, but it will with difficulty couple to modes other than those of the TF. When this excitation is used The TF spectrum generally looks cleaner.

Electromagnetic excitation

Electromagnetic excitation has the same disadvantages encountered in electric excitation but eve more pronounced. A given excitation produces more i_c than i_{osc} when compared to electric excitation.

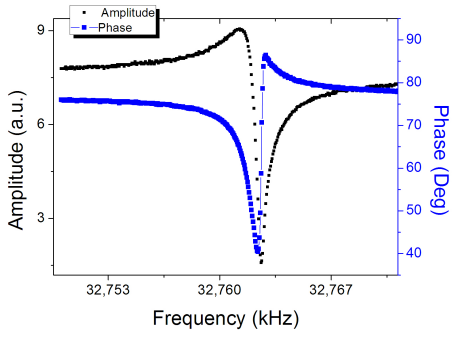

Figure 2.15: TF electromagnetically excited. The current is measured with a transimpedance amplifier. The excitation was done trough a wire passing nearby the TF. This type of excitation is essentially undesirable.

This excitation is essentially undesirable; thus, must be avoided with proper shielding.

Electric versus mechanic excitation

Electric excitation is often chosen in detriment to mechanic excitation because it is more directed toward the symmetric motion of the TF. However, it can be shown that in the same way symmetric excitation can be used to excite an asymmetric mode, the contrary also happens.

Moreover, due to the high quality factor of the tuning fork and due to the fact the TF's are always unbalanced at some extent, the oscillation amplitude is always much higher than the excitation amplitude.

Mechanic excitation has the simplicity that the readout is simple. A current will flow through the TF only if there is stress, unlike when the excitation is electric, that gives always a current trough the TF. Moreover, mechanic oscillation gives more freedom on how to use the contacts of the tuning fork.

However, in measurements implying a full frequency spectrum of the TF, then electric excitation can reduce the number of spurious peaks due to a smaller coupling with the outer mechanical systems.

2.4.2 Signal detection

When the TF vibrates the stresses are converted in polarization or charge dislocations inside the material. This charge becomes an alternating current in the case of alternating stress fields. As the current charges the capacitance across the quartz it results in an emf. Either the current or the emf can be a measurement of the motion of the TF. However, the emf depends on the total capacitance ($V = Q/C$) of the circuit, whereas the current depends only on the properties of quartz. For this reason we have always preferred to measure the current.

However, there is no particular reason for measuring the current or the voltage as long as both have been properly calibrated.

After calibration of the tuning fork, which will be discussed in the third chapter, it was found that at around 32 kHz one measures about 2 nA/nm for the higher symmetric mode and 0.034 nA/m for the lower symmetric mode.

The current we detect (except for the strict mechanic excitation) is not necessarily from the vibration of the TF alone. As discussed above, in addition to this current there can be a current which is simply proportional to the excitation voltage applied on the tuning fork contacts or due to electromagnetic fields, radiated for instance when the piezoelectric (used to mechanically excite the fork) element is excited.

Hence, even in the case of mechanic excitation we may have a parasitic current. For this reason, all cabling should be carefully thought or additional circuitry made to cancel the parasitic effects.

Since we excite the TF mechanically, we paid special attention to shield the TF from any external electromagnetic fields, particularly having frequencies close to that of the tuning fork.

Moreover, the wires from the TF to the amplifier were always as short as possible.

Detection with a transimpedance amplifier

We have in most of this thesis used a commercial *femto* preamplifier. Previously we have used an home made preamplifier mounted very close to the TF but its

performance was not as good as that of the commercial one and moreover, we found out that it should be out of the structure containing the TF for sake of temperature stability. This decision was also made because at some point we wanted to operate the TF in vacuum, and this is obviously easier if the amplifier is out of the chamber containing the TF.

The most used gain was $10^7\Omega$. This gain was found experimentally to be the one for which the signal to noise ratio at around 30 kHz was the highest. For instance, with this gain we obtain the highest contrast of the Lorentzian shaped curve of the Brownian motion of the TF prongs. If we chose a bigger gain we need a higher load resistor leading to higher white noise from the resistor. If the excitation is mechanic, then the experimental setup is as easy as that of figure 2.16.

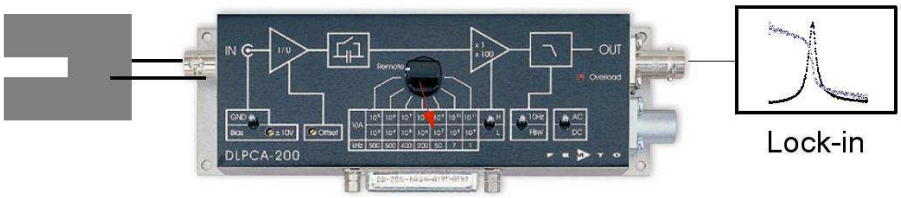

Figure 2.16: Experimental setup for measuring the displacements of the TFs prongs.

Detecting Brownian motion of the TF's prongs

If the only excitation is a white thermal excitation then at the TF's resonance frequency, Brownian motion [41, 42, 43, 44] will result in an oscillation of the TF prongs with an average amplitude of few hundreds of fm to which will correspond an average current of few hundreds of fA.

The detection done as explained above is good enough to measure the TF's Brownian motion.

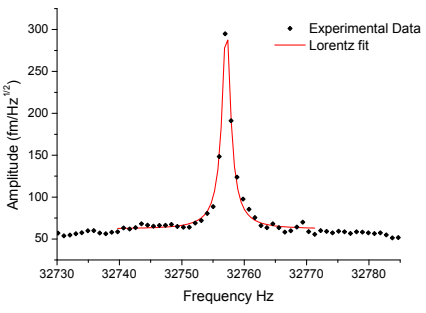

Figure 2.17: Brownian motion of the TF prongs

The curve was obtained by averaging about 1s per point.

2.5 The Q factor of the tuning fork

The quality factor Q of the tuning fork is of extreme importance for the use we want to do of the TF i.e., place it at the heart of an AFM. In this context, the Q factor of a TF is often compared to that of a more common Si cantilever.

This comparison makes sense only for use in air, since under vacuum the Q factor of a TF and Si AFM cantilever are pretty much the same.

It is often mentioned that the large Q factor of the TF is due to its symmetry. However, the high Q factor of a TF cannot simply be due to its symmetry (no motion of the centre of mass), otherwise a TF and a Si cantilever would also have different A factors under vacuum.

However, its symmetry may influence depending on how the fork is anchored.

The Q factor definition

The quality factor is defined as:

$$Q \equiv \frac{f_0}{\Delta f} \tag{2.56}$$

Where f_0 is the resonance frequency Δf the width at half maximum (FWHM) of the resonance curve. The width of the response is inversely proportional to the relaxation time i.e, $\Delta f = 1/\tau$.

Let us suppose in the time τ the oscillator makes N cycles thus taking a time $\tau = N \times T$. Hence,

$$Q = \tau f_0 = N \times T \frac{1}{T} = N. \tag{2.57}$$

Then Q is the number of cycles required for the system to relax. Q is obviously related to damping. Without damping there is no relaxation. Without relaxation the frequency response of the fork is a Dirac function.

Indeed Q is inversely proportional to the Δf, the full width at half maximum of the Lorentzian response which is given by:

$$\Delta f = \frac{\gamma}{2\pi m} \tag{2.58}$$

Where γ is the damping and m is the mass of the harmonic oscillator.

From its definition and from the fact that $2\pi f_0 = \sqrt{k/m}$ it is possible to draw a relationship depending only on the constants associated to each one of the three terms appearing explicitly in the oscillator equation stating Newtons third law (k, m, γ).

$$Q = \frac{\sqrt{km}}{\gamma} \tag{2.59}$$

The spring constant and the mass of the oscillator are intrinsic properties of it. The damping γ is, on the contrary not totally intrinsic since it is easily influenced by external damping mechanisms.

2.5.1 Damping mechanisms

We will now make a short overview of the main damping mechanisms.

Internal damping

The intrinsic damping is obviously internal loss, where mechanical energy is converted to heat.

This type of loss can be taken in account if we assume the Young modulus to be complex: $E = E_1 + iE_2$ where the complex part is associated with losses, and is usually called loss modulus. It means noting more than the following: when we assume a crystal composed of masses attached by springs, we are here assuming each spring to be damped. Of course for non crystalline materials this description is very simplified. Internal dissipation comes into play in the following way:

$$\tau_2 = \frac{1}{\pi f}\frac{E_1}{E_2} \tag{2.60}$$

For hard crystals E_2/E_1 is extremely small, down to 10^{-5}.

For crystals this path of loss is small compared to air damping and is only important if the oscillator is in vacuum or operates at extremely high frequencies.

In vacuum both a TF and a Si cantilever have Q factors of the order of 100,000. Since they have similar resonance frequencies, they both relax with a time constant of the order of 1s. Internal damping is what limits the Q factor in vacuum and when energy is not lost to external media trough the anchoring point which is another channel for dissipation.

Air damping

Air damping is important. It depends mainly on the relation between the cantilever mass and the mass of air displaced.

If we pick up two oscillators with the same resonance frequency the one with higher density will have a better quality factor. Furthermore, if they have the same density than the thicker will exhibit longer relaxation time thus better quality factor.

$$\tau_1 \propto \frac{\rho r}{\sqrt{f}} \tag{2.61}$$

For a TF this is of about 0.5 s which corresponds roughly to the observed value of 0.35 s.

It is perhaps interesting to compare this to a Si cantilever. Since the relaxation time evolves more or less proportionally to the thickness of the cantilever it is expected that a Si cantilever with comparable resonance frequency would have a Q factor few hundreds of times smaller as is the case.

This is very intuitive since the ratio of effective mass to mass of air displaced is much higher in the TF.

Actually air damping is what limits the Q factor of a Si cantilever, whereas for a TF air damping is still comparable to internal damping.

Energy loss trough the supports

If energy trough the supports could be neglected then one would not be able to excite a cantilever with a piezoelectric dither, unless the dither was directly attached to the cantilever.

This path for losses is negligible for a balanced tuning fork since there is no motion of the centre of mass, thus no energy is transfered to the supports. This fact makes if possible for a TF to vibrate in our hands. A drums dish is fast shut off as soon as we touch it.

If the tuning fork is not symmetric than one should try to either balance the fork. With proper fixation this should not be an issue even for unbalanced forks.

Due to the size (very little mass) of a Si cantilever this is usually not a limiting factor.

The total time constant

The total time constant τ is then obtained by taking the harmonic mean of the three:

$$\frac{1}{\tau} = \frac{1}{\tau_{air}} + \frac{1}{\tau_{int}} + \frac{1}{\tau_{cont}} \tag{2.62}$$

In air the damping of a Si cantilever is dominated by the first term on the right whereas for a TF the two first play the role. The experimental setup should try to avoid having the last term relevant if the Q is to be kept high.

The quality factor is then $Q = \tau f_0$.

A high Q factor is not always advantageous but in the context of AFM it is advantageous. Its role will be discussed in the next chapter.

2.6 Other resonant modes of the TF prongs

There are six vibration modes of the TF in the frequency range of 100kHz. However, several modes cannot be used due to the geometry of the TF electrodes.

There are, however, some modes of the tuning fork that can eventually be used. For instance, the torsional modes are very easy to excite and to detect.

2.6.1 Another symmetric vibration of the TF

While using the TF we observed several times a resonance peak at about 75kHz. We believe that this oscillation is also symmetric. The Q factor of this mode is always very high and its resulting signal is easy to measure. In the experiment where we have cut bits of prongs to the TF (2.11) we measured the evolution of this peak. This is shown in figure 2.18.

Note that the frequency shifts are higher than those obtained for the mode at 32.768kHz. As we will see in the next chapter, for AFM applications a good compromise between Q factor and relaxation time must be found. In this context this peak may be advantageous when compared to the frequently used peak at 32.768kHz.

2.6.2 Torsional mode

Torsional waves are non dispersive, which means that they have a wave velocity that is independent of frequency:

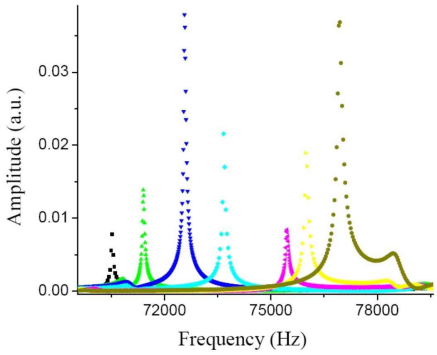

Figure 2.18: Resonance curves showing the evolution of the resonance frequency of the symmetric mode (evolving motion of the centre of mass) for different prong lengths.

$$c_t = \sqrt{\frac{GK_t}{\rho I}} \tag{2.63}$$

K_t is the torsional stiffness factor.

$\sqrt{K_t/I}$ for a prong with the dimensions of a tuning fork is of about 0.76. Thus $c_t = 2604$ m/s.

For one end clamped and one end free the allowed torsional modes are:

$$f_{tm} = m174kHz; \qquad m = 1, 3, 5.... \tag{2.64}$$

The first mode (m=1) is very easy to observe in the TF as illustrated in figure 2.19.

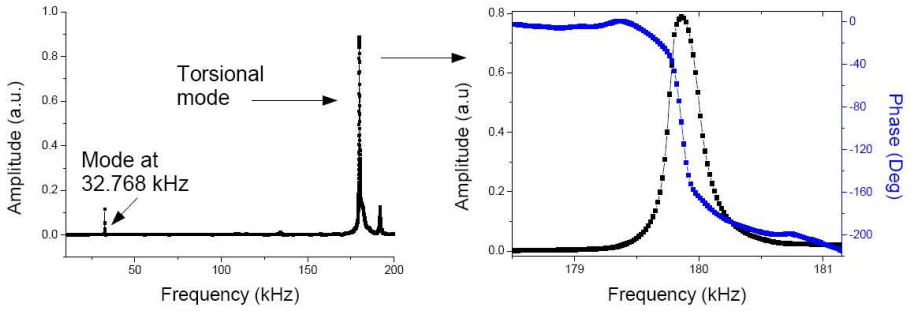

Figure 2.19: TF spectrum and torsional mode

2.7 Piezoelectric response of the TF

At some point we wondered about how much the TF piezoelectric prongs respond to a DC signal for possible application as a fine vertical scanner or to be used as a tweezers. Of course, for the last application one should, in a way or another, decrease the gap between the two prongs. Here, we will simply present the results obtained when applying a potential difference of up to 100V at the TF electrodes.

The DC voltage was applied in the TF as depicted in the scheme of figure 2.20. simultaneously, the TF mechanically excited trough a piezoelectric material glued somewhere close to the TF.

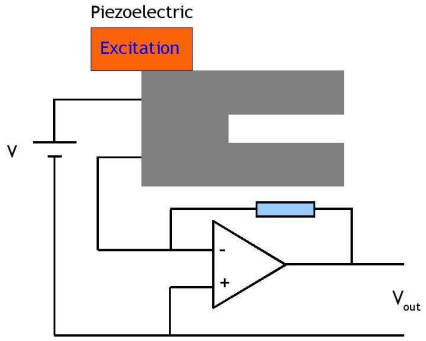

Figure 2.20: Scheme showing how was the TF connected to the high voltage power supply.

First of all we measured the resonance curve of the TF while applying 100V. We did not see any difference in the resonance curve. The TF response was then used to approach the tip to a sample. The procedure is explained in next chapter. The voltage supply was then sweep from 0V up 100V. This caused the TF prongs to open. The voltage is then sweep from 100V to 0V which caused the prongs to close. The opening and closing of the prongs can be measured because when the prongs open, the distance between tip and sample decreases which results in a response of the feedback loop to compensate the opening and closing of the prongs so that the distance between tip and sample is kept constant. This is shown in figure 2.21.

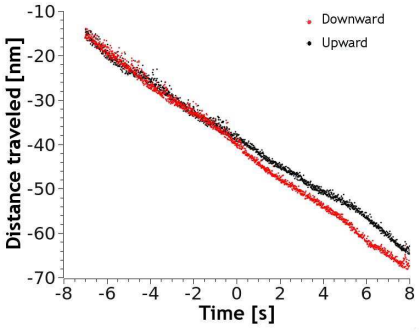

Figure 2.21: Response of the feedback loop as a consequence of an emf applied at the TF contact pads.

The prongs open about 6 Å per applied volt. It is perhaps very little for tweezers like application, unless we act to mechanically change the stiffness of the prongs. For applications where atomic resolution is envisaged, its small response to an excitation may be appreciated.

We have also obtain a topographic image of the sample while applying 100V to the TF contacts. This is show in figure 2.22.

The possible application of this have not been further explored.

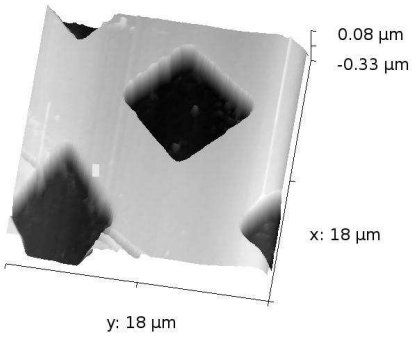

Figure 2.22: Topographical image of a calibration grating while a constant voltage of 100V is applied between the TF contact pads.

2.8 Conclusions

It was found that for the fundamental modes of an individual TF prong the Euler-Bernoulli beam approximation is sufficiently accurate and was used for all practical proposes when considering the fundamental resonance frequency of an individual clamped TF prong.

Furthermore, the fact that the experimental resonance frequencies of a TF are lower than those calculated for an individual prong is not due to a miss calculation because of neglecting rotational inertia or shear motions.

Hence, the resonance frequency of a TF is different than that of its individual prongs.

To account for the lower resonance frequencies of the TF the two prongs were coupled to a common anchoring point.

The stiffness of this common body was adjusted to give resonance frequencies identical to those observed experimentally.

A simplified transfer function that includes interaction of one of the TF prongs with the external world was then obtained. This simplified transfer function of the TF was assumed to be accurate enough for all our purposes.

The resonance frequency of the tuning fork is given by:

$$\omega_i = \sqrt{\frac{k_r + \epsilon k_i}{m_r}} \tag{2.65}$$

with $k_r = 10.4kN/m$ and $m_r = 240\mu g$ the reduced stiffness and mass respectively.
The width of the resonance curve is given by:

$$\frac{\gamma_{ri}}{m_r} = \frac{\gamma_r + \epsilon\gamma_i}{mr} \tag{2.66}$$

with $\gamma_r \approx 5mg/s$, corresponding to a width of few Hz
and

$$\epsilon = \frac{1}{2}\frac{m_2}{m_1 + m_2}. \tag{2.67}$$

It was then discussed the Q factor of the tuning fork.

Here we saw that the main damping mechanism affecting the TF as well as a Si cantilever is air damping.

Though, air damping is about 100 times higher for a Si cantilever due to its smaller dimensions. The symmetry of the TF may or not have an important role depending on the relative impedance of the media to which it is attached.

If the fork is perfectly symmetric then this last aspect never matters, since no velocity is imparted to the other media.

Due to the very small impedance of a Si cantilever this does not usually play a role.

The tuning fork is extremely easy to excite either with a piezoelectric actuator or with a small electric field at its electrodes, typically on the range of few mV.

Attention should be so that the TF is not excited with electromagnetic fields.

Acoustic excitation is also a possibility though more difficult to trigger.

The detection is very easy either using a current to voltage amplifier or a voltage to voltage amplifier. Gains of the order of $10^7\Omega$ in the first case and 100 in the second case result in signal of the order of a mV/Å of vibration.

It was also shown that the TF can easily be used as a piezoelectric scanner moving about 6 Å per applied volt.

Chapter 3

An AFM with a tuning fork

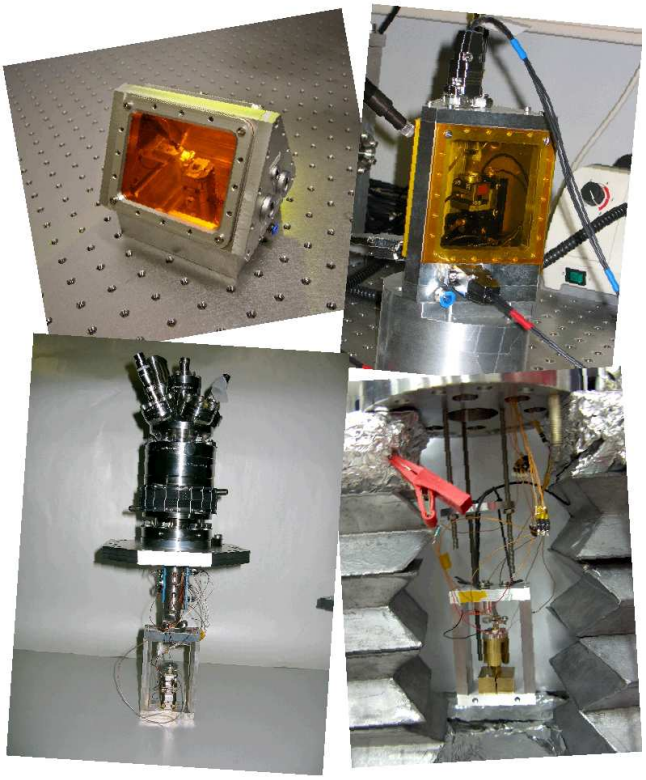

Contents

3.1 Introductory remarks

In this chapter it will be introduced the concept of atomic force microscopy. We will explain how the functions of an AFM can be accomplished with a tuning fork.

It was after the advent of scanning tunneling microscopy (STM) [6] that Binning [8] introduced the AFM. In AFM a sharp tip is used to probe the force fields emanating from the sample and acting on the tip. The interaction with the tip is then transduced through a mechanic effect in a spring-like system that translates force in displacement. The sharp tip is, of course, meant to localize the measurement.

Hence, if we would like to obtain images with atomic resolution then we would use an atomically sharp tip.

Indeed, silicon cantilevers are spring-like systems and together with a laser and a photodetector are the most widely used force transducer in atomic force microscopy. The laser and photodetector are used to convert displacements of the cantilever to an electrical signal.

The reasons for using silicon are quite obvious. It is clearly one of the chemical elements best known to humankind. It is also one of the cheapest. Silicon cantilevers can be constructed with almost arbitrary shapes and spring constants.

It exist in the market of *micro fabricated silicon cantilevers*, cantilevers with spring constants as small as $10\mu N/m$. The most typical values ranging from 1 to 40 N/m.

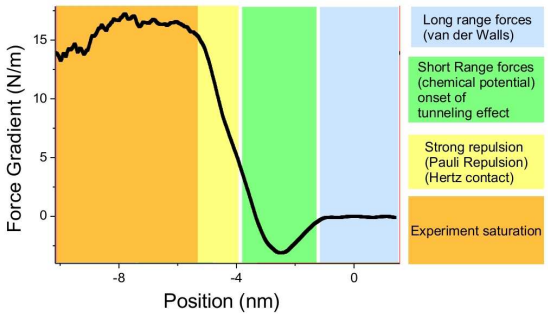

Figure 3.1: Experimental force gradient between a tungsten sharp tip and a gold surface measured with a TF.

It is interesting to compare these values with the force gradients between a surface and a sharp tip. In figure 3.1 is shown an experimental force gradient curve measured with a tuning fork.

At few nm from the sample the force gradients are much larger than the spring constant of the softest silicon cantilevers.

It becomes straight forward to measure tip-sample interactions with such cantilevers.

Of course, the actual values of the forces and force gradients depend on the geometry of the tip, or on how many atoms contribute to the total force. Here, as in most of the cases throughout this work, the tip apex radius was of few tens of nm. Industry of Si cantilevers deliver them with tips having apex radius smaller than 10nm. The use of such tips is required for atomic resolution. However, such high resolution is in most of the cases not required. Typical numbers are of 10 to 20 nm and 1 Å for lateral and vertical resolution respectively.

At short distance, when the electron clouds start to overlap, only the very first atoms of the tip contribute to the force, whereas in the van der Waals regime the whole tip apex radius contributes to the total measured force. In figure 3.1 the long range contribution, van der Waals, Casimir, etc., cannot be seen, however the stronger short range forces, essentially due to chemical bonding, can. The sensitivity to chemical bonds makes it easier to obtain atomic resolution with an AFM [45, 46].

A force can be measured with a spring-like by simply measuring the displacement of the spring and determine the force trough $F = -kx$ and this is the basic way to do it. When such is done and used to obtain AFM images, it is called contact mode. A spring-mass system is obtained when a mass is added to the spring-like system. Since one cannot make massless springs, a cantilever is always a spring-mass system. This gives us the basic way of measuring force gradients, rather than the forces themselves. A spring-mass system exhibits resonant behaviour at $\omega = \sqrt{k/m}$. While the Si cantilever interacts with the sample, its effective spring constant changes, so does its resonance frequency. When this is used to obtain images it is called *dynamic mode*. This is the mode that has always been used throughout this work and is discussed in greater detail below.

3.1.1 Contact mode

The force F can be measured by measuring the deflection of the spring. The force is then given by $F = -kz$, where k is the spring constant and z is the deflection of the spring.

In this case the spring is approached to the surface until the force is enough to deflect the spring. This deflection is routinely measured with help of a laser and a four quadrants photodetector, or with any other position sensitive photodetector. Light is shined onto the back of the deflected cantilever and is reflected on the detector. This is shown in figure 3.2.

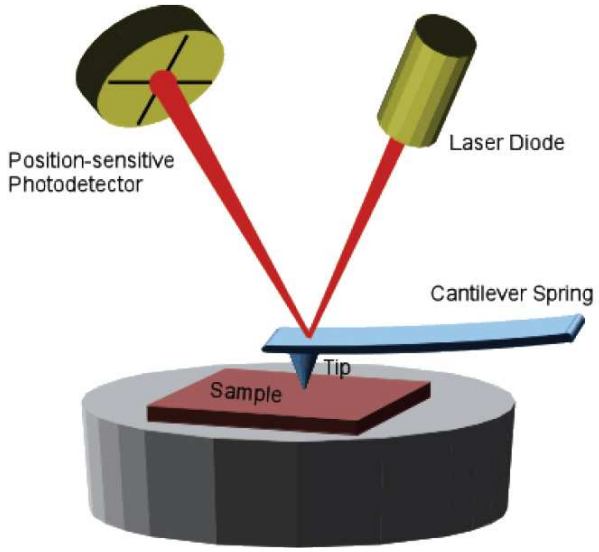

Figure 3.2: Experimental setup for measuring displacements of a cantilever interacting with a sample.

The position at which the laser is reflected depends on the deflection of the cantilever and is a direct measure of the deflection z, and thus, of the force F. When a four quadrants detector is used the position at which the laser is incident on the photodetector is given by the ratio of intensities detected at each quadrant.

A given deflection results in a constant laser position on the photodetector. Typically a feedback loop controls the height of the sample to maintain constant the cantilever deflection (Force) while the sample is scanned. The result is a 3D surface revealing the sample's topography, or more precisely, a constant force 3D surface. Alternatively the feedback can be turned off, in which case one obtains a 3D map of deflections.

3.1.2 Dynamic mode

The technique for operating the Scanning Force Microscope in the dynamic force mode was introduced in 1987 by Martin et al. [47] . In dynamic mode one uses the fact that the total spring constant of the mass-spring system depends on the interactions between the tip and the sample. An oscillator is brought close

to the surface until the force field acts on the oscillating mass. Several variables can be measured:

1. if the excitation force and frequency are constant:
   (a) a change in the oscillation amplitude
   (b) a change in phase between the excitation force and the oscillation in return
2. if the excitation amplitude and the phase between excitation and signal in return are constant:
   (a) a change in the amplitude
   (b) a change in the resonance frequency
3. if the oscillation and frequency are constant
   (a) the additional force needed to maintain the oscillation constant
   (b) a change in phase between the excitation force and the oscillation in return
4. if the oscillation amplitude and the phase between excitation and signal in return are constant
   (a) the additional force needed to maintain the oscillation constant
   (b) a change in the frequency

These represent four different ways of getting a topography. Actually any of the eight variables can be used to obtain a topography.

The most widely used method is the first where 1a and 1b can be measured. Usually 1a is used to obtain the topography while 1b may contain extra information. This is the easier mode to implement because it does not require any (extra) feedback loop to measure either 1a or 1b. Mode 4 requires two extra feedback loops, and modes 2 and 3 require 1 extra feedback loop each. In mode 2 the feedback loop is used to maintain constant the phase between excitation and signal in return by adapting the excitation frequency. This is a Phase Locked Loop (PLL) and throughout the text we shall refer to it simply as PLL. In mode 3 the feedback loop is used to maintain the amplitude of oscillation constant by adapting the excitation. This is the oscillation amplitude loop. Mode four needs both the oscillation amplitude loop and the PLL loop.

Most of the times we have used signal 2b, to obtain the topography. Signal 1a, 1b, were also used several times when 2b could not be used either because it was not suited for the particular purpose or a PLL was not available.

Why one does not always uses mode 1 which is the easier to implement is a good question. Most of the times, if not always, is because the other modes respond faster. This will be further discussed in a section below, where the application to the TF in particular will be discussed.

What is here left to ask is: what does one indeed measures in dynamic mode?

The phase or the frequency depend on the spring constant coupling the AFM tip with the sample. Whence, it depends directly on the force gradient between

the sample and the tip. Relationships linking phase or frequency changes to the interactions are readily obtained. In figure 3.1 the experimental data is simply given by the change of the measured phase between excitation and signal in return as a function of the distance. As will be seen below both the phase or the resonance frequency changes are proportional to dF/dz where z is the tip-surface distance.

The oscillation amplitude or the excitation depends primarily on the excitation frequency relative to the resonance frequency (at resonance the amplitude is higher, out of resonance lower) and on the damping acting on the oscillating mass. This damping causes the Lorentzian response curve to be broader and thus lower at the peak (if the area is kept constant by keeping the energy supplied constant). Because there are two effects causing the oscillation or the excitation amplitude to change, this changes become more difficult to quantify and a sophisticated analysis is needed.

3.2 Tuning forks' suitability for AFM

3.2.1 Gluing and etching of the W tip

One of the inconvenient aspects of using a TF is that they do not come already with tips. However, this is noting but a minor difficulty. This sections concerns the manufacture of the tips as well as the gluing procedure. In the course of this work two methods were used to etch and glue the tip on the TF. In both cases the tip was chemically etched.

The etching process

A review on the making of sharp tips with different etching techniques is given by Melmed [48].

An easy way to use etching technique is the so called *lamellae dropoff technique*, where a small ring electrode is used as a cathode. A drop of either NaOH or KOH 2-3M in the ring creates an electrolytic cell in which the tungsten wire is etched. This is illustrated in figure 3.3.

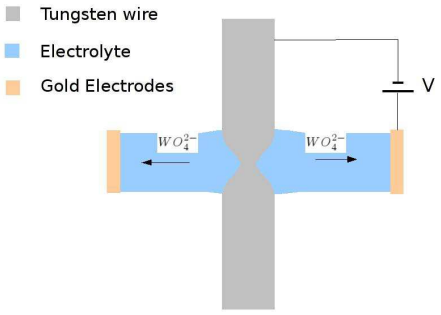

Figure 3.3: Basic scheme of *lamellae droppoff technique*

For etching, a dc voltage of about 4V to 6V is applied to the electrodes, the tungsten wire acts as the anode and the gold electrode as the cathode. An etching current on the order of mA induces the following chemical reactions:

$$6H_2O + 6e^- \leftrightarrow 3H_2 + 6OH \quad cathode \tag{3.1}$$

$$W(s) + 8OH^- \leftrightarrow WO_4^{2-} + 4H_2O + 6e^- \quad anode \tag{3.2}$$

$$W + 2OH^- + 2H_2O \leftrightarrow WO_4^{2-} + 3H_2 \quad total \tag{3.3}$$

After an etching time of less than 5 minutes, the wire becomes so thin that the lower portion of the tungsten wire falls down under its weight to a padded container, or is rejected and only the upper part is used.

The lower part is naturally sharper since the etching process stops as soon as the tip falls down. The upper part continues on etching unless the power supply is shut off. Extended etch may be useful if one desires to obtain tips with radius on the order of the μm. Otherwise tips have curvature radius smaller than 100nm. Typical tips look like those in the figure 3.4 and 3.5.

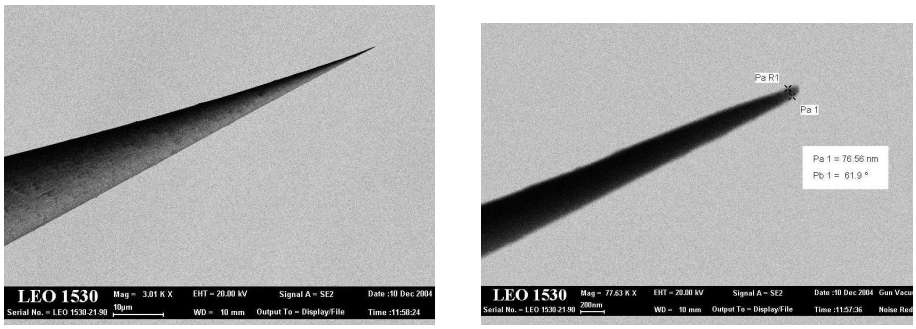

Figure 3.4: SEM pictures of a typical tungsten etched tip with the detail of the apex (right)

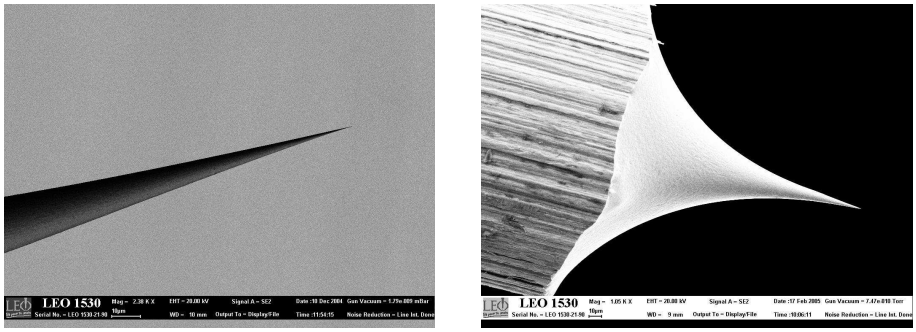

Figure 3.5: SEM pictures of the lower tip (left) and upper tip (right) for comparison

The upper tip and lower are generally different. Figure 3.5 illustrates this difference.

The length (weight) of the wire below the place were the chemical reaction takes place matters. We found that about 2 to 3cm was optimal.

Etching with one ring

Initially the scheme used shown in figure 3.3 was used. Both the upper and lower tips were used. After etching, the tips were cut off from the remaining wire and carefully glued on the TF. This is time consuming and likely to provide a big headache!

Alternatively one can replace the wire holder by the tuning fork with the wire already glued on. If the glue is conductive and connected to one of the TF contacts, then trough the glue one can connect the power supply to the tip. In this case the lower tip is rejected and the upper tip is already glued after the etching process. The power supply must be turned off fast to avoid further etching of the tip, resulting in a blunt tip.

To prevent further etching of the upper part, we have used the fact that the etching current drops drastically when the lower end of the tungsten wire falls down. The power supply was equipped with a fast electronic switch set to break the current when it falls below a preset value. A little labview program was made to detect the sudden decrease in voltage and consequently shut down the supply. Similar methods to switch off the current exist [49].

Etching with two rings

Etching using two rigs as electrodes can be considered as a useful upgrade specially for newcomers because of the increased simplicity and it does not require the power supply to be shut down automatically. The experimental setup is illustrated in figure 3.6.

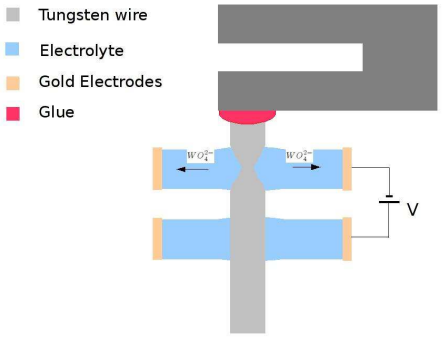

Figure 3.6: Basic scheme of *Scheme of a lamellae droppoff technique using two rings*

Here the circuit opens when the wire fall down thus stopping the etching process automatically. Moreover, the glue does not need to be conductive since the power supply is not directly connected to the tungsten wire. There is no disadvantages compared to the first method, except that there is twice the chance the *lamellae* breaks before the etching process is done. If so happens, one must restart. The general geometric aspect of the tips is of course similar to those shown before.

3.2.2 TF versus Si cantilever

In this section we compare tuning forks with the most commonly used Si cantilevers. The first advantage of TF is in the experimental set up. The exper-

imental setup of AFMs based on Si cantilevers are much more sophisticated, because they require a laser and a position sensitive photo detector. These two extra elements must be mounted in the setup in such a way that the three can be aligned: the laser incident on the cantilever and the laser reflection on the centre of the photodetector. Every time a cantilever is changed one must proceed to the alignment. Whence, the architecture of a AFM based on a TF is much simpler. Of course, the decision of a particular setup should not be limited to an inertia issue. Could one make a bigger initial effort to obtain a better final machine? It becomes relevant to make a qualitative and quantitative comparison between the two possible choices. Table 3.1 summarizes some of the differences between TF and Si cantilevers.

	Si cantilever	Tuning fork	
Resonance frequency	30kHz< f <400kHz	usually 33kHz or 100kHz	
Width at half maximum	200Hz up to 1kHz	4Hz up to 10 Hz	✓
Cantilever stiffness	1N/m to 100 N/m	5kN/m 30kN/m	×
Length	few hundreds of μ m	few mm	✓
Relaxation time	1ms to 20 ms	.1 to 1s	×
Brownian motion	up to few nm/$\sqrt{Hz}$	few hundreds of fm/$\sqrt{Hz}$	✓
Piezoelectricity	no	yes	✓
Optics-free	no	yes	✓
Comes with tip	yes	no	×
Easy to handle	no	yes	✓

Table 3.1: Comparison between TFs and Si cantilever for AFM applications.

Tuning forks are huge when compared with a Si cantilever!

They have very high spring constant. Hence, at a first look they may seem potentially less sensitive to measure forces. On the other hand they are easier to handle and to see and can have huge tips attached to them. This makes things simpler since at some point we would like to illuminate the tips with the Synchrotron X-ray beam. A larger tip is easier to find. Another aspect coming from their size, is that they have huge Q factors. Even though this is in part due to the symmetry of the TF, it is also due to the fact that tuning forks are big.

Si levers are small:

They are very soft, and thus, are potentially very sensitive, but are difficult to localize. Other aspects have to do with the temperature stability of quartz compared to that of Si cantilevers. The resonance frequency of Si cantilever changes few Hz per Kelvin, while the resonance frequency of a TF quartz has virtually no change.

3.2.3 Frequency shifts of an interacting TF reviewed

We now review some of the useful conclusions drawn in the first chapter that are here important. Namely equations 2.52, 2.53 and 2.54.

A formula for the small interactions

It is very common and convenient to consider equation 2.54 in the limit of small interactions. By small interactions it is meant that the force gradient or the *spring* coupling the oscillator with the sample is much smaller than the spring constant of the cantilever. This is often the case, and definitely is the case if a tuning fork is used because of its very high stiffness.

In case of small interactions, using equation 2.54 and equation 2.52, we can calculate what is the expected TF resonance frequency shift (df) due to a coupling between the tip and the surface.

We find without difficulty the following relationship.

$$df = \frac{\epsilon k_i}{2k_r} f_0 \tag{3.4}$$

Where we remind k_i is the force gradient, k_r, f_0, and ϵ are respectively the reduced TF stiffness natural frequency and a constant depending on the symmetry of the TF. When compared to the usual equations used when Si cantilever are implemented, a new factor ϵ intervenes.

It is common to relate the increase in the width at half maximum of the resonance curve to the dissipation resulting from the interaction forces.

If dissipative measurements take place these are also affected by the same factor ϵ:

$$d\gamma = \epsilon\gamma_i \tag{3.5}$$

Mass added to one prong: effect on the TF's sensitivity

As discussed previously, the tuning fork alone cannot be used to perform AFM. A sharp tip must be mounted on the TF.

The response and ability of the TF to be used in *dynamic atomic force context* will depend on the added mass of the tip as well as on other parameters. The added mass changes the value of the constant ϵ. The heavier the added mass the smaller ϵ will become. Because sensitivity is directly proportional to ϵ (3.4 and 3.5) it is important to evaluate its value.

The resonance frequency of the TF will of course change after the mass has been added. This change will decrease the value of ϵ from 1/4 (symmetric fork) to a lower value. It is not very practical to weight the tip that is mounted on the fork. However, one can easily tell the value of ϵ from the shift in resonance frequency. From equations 2.42, 2.46 and 2.51 its obtained:

$$\epsilon = \frac{f^2}{2(f^2 + f_0^2)} \tag{3.6}$$

where f is the frequency after mounting of the tip and f_0 is the free resonance frequency. With a small tip for which the corresponding resonance frequency would be ≈ 31 kHz ϵ would be $\epsilon = 0.236$.

Increased stiffness

As a matter of fact the tip is mounted on the tuning fork by gluing it. Thus it is not as simple as to say that one prong has a bigger mass than the other. The

prong with the tip will also become stiffer due to the tip gluing. The glue plus tip will oppose to the bending. This means that the resonance frequency shift due to the fact a mass was added is going to be slightly smaller than that expected for such a mass. This has been discussed in the first chapter (simulation and experimental results). The effect of this is that when evaluating the constant ϵ on should consider a higher *no mass added* resonance frequency f_0 if equation 3.6 is used. Or, if possible, use equation 2.51. Typically the increase of stiffness due to mounting of a small tip is of 1% to 4% which produce frequency shifts of 1% to 2%.

How much interaction do we measure?

If the tuning fork oscillates with 1 Å of amplitude and is placed above a sample in a position where the force gradient is **3nN/nm** and about constant in this 1 Å of oscillation, then the resonance frequency of the fork will change by about:

$$\frac{0.220 \times 3}{2 \times 10422} 31000 \approx 1Hz \tag{3.7}$$

The frequency change is proportional to the force gradient. The proportionality constant κ is in turn proportional to ϵ and inversely proportional to the TF reduced stiffness:

$$\kappa \approx \frac{1}{3}\ Hzm/N$$

The TF will change its frequency by about 1 Hz in the presence of 3 nN/nm force gradient.

But how little frequency shifts can we measure? That depends on the oscillator used. For a TF, operated in air, one can easily measure frequency shifts of about 0.1 Hz. It is here that the Q factor of the TF plays an important role.

3.2.4 Role of the quality factor

How can we be sensitive to nano with a millimetric cantilever?

The secret for the sensitivity and success of tuning forks lies in their high quality factor.

The Q factor is related to the damping or dissipations present in the system. Thus, it is naturally related to the Fluctuation-Dissipation theorem. Very high quality factor means little dissipation and thus, following the result of the theorem it means little fluctuations. Or in other words little *error* while measuring its state of oscillation.

It has been shown in the previous chapter that an interacting tuning fork changes its resonance frequency according to the value of the interaction. More specifically for small interactions, such as those intervening when an AFM image is taken, the resonance frequency shift $\delta f = (f - f_0)$, i.e., the difference between *interacting* frequency and *natural* frequency, is directly proportional to the force gradient of the interaction. Thus, measuring a small force gradient is ultimately a question of measuring a small frequency shift. The smaller the width of the curve (higher Q factor) the better small frequency shifts can be measured.

Why? Because the phase shifts are much larger. Q times larger.

The phase changes about linearly by $\pi/2$ within Δf, with Δf the FWHM. Thus if the change in resonance frequency is of δf than the phase change is of

$$\delta\phi = \frac{\pi}{2\Delta f}\delta f \tag{3.8}$$

and replacing Δf by f/Q,

$$\delta\phi = Q\frac{\pi}{2f}\delta f \tag{3.9}$$

finally replacing δf (equation 3.4) we find,

$$\delta\phi = \frac{\pi}{4}\frac{Q}{k}k_i \tag{3.10}$$

Thus the way the Lorentzian curve is affected by the interaction force gradient is directly proportional (for small forces) to the Q factor of the oscillator and inversely proportional to its stiffness.

About the sensitivity of the oscillator:

The frequency shifts are higher if lower spring constant is used, however, smaller frequency shifts can be measured if the Q factor is higher.

For this reason the ratio k/Q is often refer to as *dynamic stiffness* of the oscillator. In the case of the tuning fork the *dynamic stiffness* is $\epsilon k/Q$.

The problem has obviously been reduced to a phase measurement problem. In dynamic AFM either a lock-in amplifier or a phase locked loop are used to access the properties of the oscillator. If it is true that with the lock-in the output is a phase and with the PLL a frequency, it is also true that they are both phase comparators and in both is the phase that matters. In the end a frequency is nothing else than a phase evolving in time.

It is worth mentioning that the Q factor does not need to be intrinsic to the oscillator. Some authors have been using feedback systems to actively change the response of their oscillators so that larger Q factors can be obtained. However, we will not discuss this point here. The intrinsic Q factor of the TF is high enough for all the purposes of this work.

3.2.5 Lock-in and Phase Locked Loop control - a quick review

In this section we will review the basic elements and features of a lock-in amplifier and a phase locked loop, since they are essential (one or the other), to perform AFM. In the introduction of this chapter, when dynamic mode was introduced, we spoke of four possible modes, and was in that context that we introduced both the lock-in and the PLL. Depending on which mode we want to use we will choose either one or the other.

While the lock-in amplifier is widely used in experimental physics the PLL is mainly used in communications. For example in an FM radio. It is true that a lock-in amplifier is used in AM communication, but more often is because the measurement systems are often troubled by $1/f$ noise. By modulating in amplitude the signal to be measured at some reference frequency f_0 the noise at the output can be often reduced and drift problems avoided. In the next chapter we will make use of this feature by modulating the X-ray beam with a

mechanic chopper and measure only the response to the modulation resulting in automatic background subtraction. Naturally the noise component of the background remains.

In the case we present here we will use the lock-in to measure the amplitude of an oscillating lever. In AFM it is common to measure oscillation amplitudes of the order of the Å. The variation in amplitude caused by the acoustical waves we emit as we speak easily excite the lever to values higher than the Å. Thus, sophisticated tools are required to separate the useful part of the signal, containing the information we want from the useless part due to external forces.

The Phase Sensitive Detector

To fix ideas and to emphasize that both the lock-in and the PLL use a phase sensitive detector (PSD) we hereby introduce it. This is also the reason why in the previous section we have reduced the question of the role of the Q factor to a question of how much does the phase changes for a given interaction.

The PSD is composed by a mixer followed by a low pass filter. The mixer, or phase comparator, is most of the times a multiplier. The product is between the signal to be measured $x_i(t)$ and a reference signal $x_r(t)$. If the two can be described like:

$$x_i = A_i \sin(\omega_i t + \phi_i) \tag{3.11}$$
$$x_r = A_r \sin(\omega_r t + \phi_r) \tag{3.12}$$

then at the output of the multiplier one has:

$$x_{ir} = A_i A_r \sin(\omega_i t + \phi_i) \sin(\omega_r t + \phi_r) \tag{3.13}$$

Whence, using trigonometric identities:

$$x_{ir} = \frac{A_i A_r}{2}[\cos(\omega_i t + \phi_i - \omega_r t - \phi_r) - \cos(\omega_i t + \phi_i + \omega_r t + \phi_r)] \tag{3.14}$$

The resulting signal can be expressed as the sum of a component of frequency $(\omega_i - \omega_r)$ with another of frequency $(\omega_i + \omega_r)$. After the multiplier there is the low pass filter. This will remove the sum frequency component, leaving only

$$x_{psd} = \frac{A_i A_r}{2} \cos(\omega_i t - \omega_r t + \phi_i - \phi_r) \tag{3.15}$$

Of course we are for simplicity neglecting internal losses and gains due to the active components of the circuit by conserving the amplitude of the wave $(A_i A_r/2)$. Let R be a constant directly proportional to A_i such that the following is true:

$$x_{psd} = R \cos(\omega_i t - \omega_r t + \phi_i - \phi_r) \tag{3.16}$$

This equation, though simple, is the only one necessary for the discussion, since any periodic signal can be described as an infinite sum of cosine functions.

We will come back to this equation soon.

The lock-in amplifier

The lock-in amplifiers can be thought of as a band-pass filter amplifier, with an extremely small bandwidths and extremely high Q factors that cannot be achieved by a conventional circuit (eg. RLC). Q values of 10^{10} and noise bandwidths smaller than 0.001 Hz are easily implemented in lock-in amplifiers.

The basic lock-in consists basically of: - a frequency generator, that can for instance be a voltage controlled oscillator (VCO), which is an oscillator whose frequency is proportional to a d.c signal, or a PLL; - whichever is chosen is implemented then together with a phase shifter. These two elements compose the reference channel meant to produce the reference signal x_r. The output of a simple lock-in is simply the output of the PSD when using as inputs this reference signal and the signal to be measured.

Since the reference signal is also used to excite the TF, this will result in a signal at the output of the TF preamp with the same frequency of that generated by the lock-in. According to equation 3.16, this will result in an output:

$$x_{o1} = R\cos\left(\phi_i - \phi_r\right) \tag{3.17}$$

Additionally, the lock-in may dispose of a second mixer and apply to the signal the same treatment in parallel, i.e, a copy of the input signal goes to a second mixer and is mixed with the reference signal phase shifted $\pi/2$. Thus, the output of the second mixer is:

$$x_{o2} = R\sin\left(\phi_i - \phi_r\right) \tag{3.18}$$

When a second channel is available a vector/phase computer is implemented:

$$X_o = \sqrt{x_{o1}^2 + x_{o2}^2} = R \tag{3.19}$$

$$\phi_0 = \arctan\frac{x_{o2}}{x_{o1}} = \phi_i - \phi_r \tag{3.20}$$

These two last outputs are the ones typically used in AFM. The phase ϕ_i depends on the relation between the oscillator excitation and response. As seen before, its change is directly proportional to the change in the resonance frequency (due to the interactions), provided the excitation is near resonance. Thus, it is an almost direct measurement of the conservative interactions.

Both the phase and the amplitude were widely used in this work for AFM imaging and other force measurements.

The Phase Locked Loop

The phase locked loop happens when we apply feedback control to the variable out of the PSD. In the lock-in this variable is the output. In the PLL also, but is actively controlled to maintain a certain set value that follows the set point. At the output of the PSD one has:

$$x_{psd} = R\cos\left(\omega_i t - \omega_r t + \phi_i - \phi_r\right) \tag{3.21}$$

Where R is again directly proportional to the amplitude of the test signal. In the lock-in there is a fixed reference frequency given for example by a VCO. In

other words one sets a d.c. signal in the VCO and this oscillates with a fixed frequency depending on this d.c. signal.

In the case of the PLL the input of the VCO is the signal out of the PSD, x_{psd}, thus forming a loop. The frequency is now changing as much as x_{psd}. As a result of this frequency change x_{psd} changes too.

Let us suppose that the frequencies are the same in which case the PLL is locked. In that case, one finds again :

$$x_{psd} = R\cos\left(\phi_i - \phi_r\right) \tag{3.22}$$

If they are synchronized to the free running frequency or the centre frequency ω_0 then x_{psd} is zero. Which means that ϕ_r is such that $\phi_i - \phi_r = \pm\pi/2$. This is why when using a PLL we always take some care to find the proper phase. So that the condition above is fulfilled.

If ω_i changes slightly from ω_0, the signal x_{psd} will adjust and settle to a nonzero value to correct ω_r. Under the condition that the frequency lock is maintained the VCO will now oscillate at $\omega_r = \omega_i$ and $\phi_i - \phi_r \neq \pm\pi/2$. Let us say that the difference to $\pm\pi/2$ is $\pm\Delta\phi$. Then,

$$x_{psd} = \pm R\sin\Delta\phi \tag{3.23}$$

Thus a momentary change in $\Delta\phi$ will tell which way to adjust the VCO (increase or decrease its frequency ω_r) and to maintain the locked condition ($\omega_i = \omega_r + error$). Obviously, the PLL cannot follow changes that are larger than $\pm\Delta\phi$. It is worth mentioning that such difference is not expected to happen in an AFM context, provided the centre frequency equals the resonance frequency of the oscillator. Even though the resonance frequency can shift to arbitrary positive values depending on the interaction, the phase will not shift more than $\pi/2$ (change in phase of an harmonic oscillator when the frequency of excitation goes from resonance to much lower values). This gives rise to the *experiment saturation* of figure 3.1, where a lock-in was actually used. With the PLL, it is easy to follow the frequency up to the same interaction without saturation. The higher the Q factor the faster an interaction leads to this type of saturation. For this reason it is sometimes convenient to use a PLL instead of a lock-in whenever the Q factor is very high. However, while acquiring a topographical AFM image such interactions are usually not taking place (if we try to be gentle with the sample).

Finally, since x_{psd} is the signal applied to the VCO, the frequency of the system being controlled is directly proportional (in a linear PLL model system) to the frequency ω_i, in this case of the TF. The proportionality constants depend on the gain of the VCO.

Even though the PLL throws a value proportional to the oscillator frequency it adjusts this frequency by measuring a phase change. And in this context the Q factor of the oscillator to be controlled plays the same role here as when using a lock-in amplifier.

It is often said that a PLL allows fast scan even when using oscillators of very high Q factor, or very long relaxation time. As mentioned above a PLL needs an internal low pass filter to reject the higher frequencies at the output of the mixer. If the time constant associated to this filter is lower than the time constant of the oscillator than one may be able to scan faster but we will loose in signal quality, thus, increasing the overall noise. The consequence is that

larger values of the interactions will have to be involved. In practice one can go faster with a PLL than with a Lock-in amplifier but not more than a factor of about two.

3.3 XAFM Set up

The Xtip project did not followed a straight path. However, some characteristics have been present throughout this work, such has the use of the tuning fork, slip stick coarse motors, and use of piezoelectric elements for fine scanning. We shall focus on this common elements without concentrating too much on the volatile details.

The tuning fork at the heart of the AFM

The TF is meant to make part of an atomic force microscope that will be combined with Synchrotron radiation. With the tip the TF is at the heart of what one could call an X-AFM. The TF is the transducer sensing the forces and the tip is what localizes these forces and, as we will see, it is also the X-rays and photoelectrons detector. For the moment let us concentrate only on the AFM aspects.

Figure 3.7 shows the general way the TF is connected.

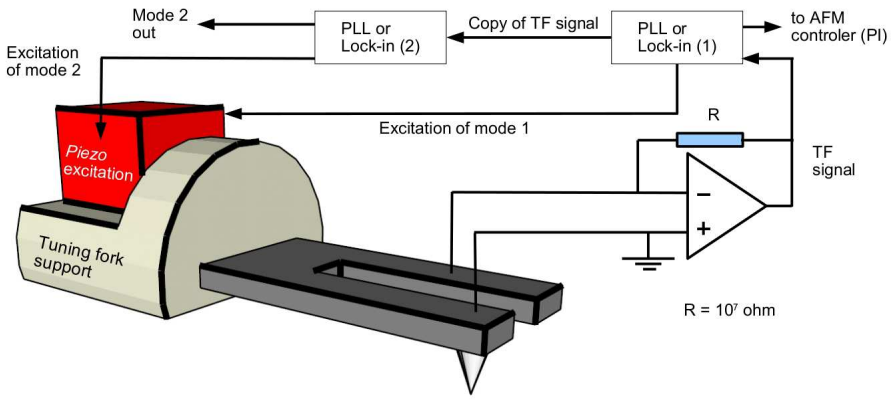

Figure 3.7: General mounting of the TF for the purpose of AFM. A tip is glued on one of the prongs. The TF is excited, usually with a piezoelectric dither. A lock-ins or PLLs are used to excite and detect the TF frequency(ies) and amplitude(s). These will change as the tip is brought close enough to a surface.

At least one lock-in or one PLL is necessary so that one property of the oscillator such as its resonance frequency can be used as the input of the feedback control. A second lock-in (or PLL) is used if we wish to measure simultaneously a second resonance frequency mode, which may be useful for combined force measurements.

For obtaining just AFM images only one lock-in (or PLL) is enough.

Now, we can measure the resonance frequencies of the fork. Let us approach the sample and see its resonance frequency changing.

Sample stage

If we want to obtain atomic resolution we need to be able to produce at the limit, displacements better than the size of an individual atom in a reproducible manner. This means of the order of few tens of pm. As an example, the Brownian motion of a Si cantilever is of the order of 1 nm.

For this small displacements it is normal and necessary, to use piezoelectric elements. They are usually very rigid, and thus exhibit little Brownian motion. The voltages applied to them are usually quite high.

Their main problem is large hysteresis and creep.

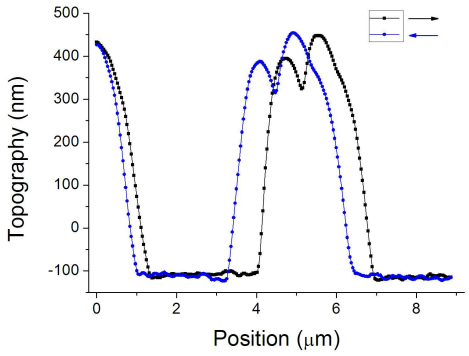

Figure 3.8: Section view of an AFM image taken with a TF. The two different curves represent scans collected with the tip moving above the sample from right to left and vice versa. The difference between them are due to piezo nonlinearities, in particular, due to creep.

Luckyly, this problem becomes less important as the explored dimension are reduced since piezoelectric actuators get closer to a linear system.

It is common to use in AFMs and specially in STM the so called piezoelectric tubes. The advantage is that one single piezoelectric element is used for the three motions, thus there is no coupling element to link X-Y and Z since they are intrinsically coupled. They definitely are the elements that move the smoothest.

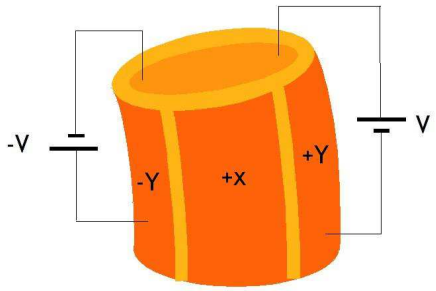

Figure 3.9: Piezo tube illustration.

However the connections and control becomes slightly more complicated. Since all the axes are coupled some algebra is necessary to uncouple them. Alternatively, this can be done via software after image acquisition. However, for large samples, uncouple the axis in real time, is better because the control loop has is job half done, i.e., it only follows the topography rather than topography plus coupling of the axes.

The XYZ fine scanners can also be composed of individual piezoelectric elements. This was always the case in the present work. The main reason was

simplicity and the usual larger ranges of this type of scanners. The disadvantage relative to piezoelectric tubes is that there is a higher drift due to a cross talk between axes, through the fasteners (acting as springs) used to hold the three directions together.

The maximum total range was either $9\mu m$ or $38\mu m$ for all the three directions. It is of course necessary to have a secondary scanner with ranges on the mm scale. Thus the X-AFM used the so called inertial motors. They are called inertial motors because they are shut off each time they move. They do not have a fixed reference frame. A piezoelectric element expands (or contracts) very fast. This produces a rod to slide between two free masses pressed against the it through springs. The piezoelectric element then slowly contracts (expands) bringing the two masses together with the rod. The result is a motion of the two masses that can be almost as little as the smallest piezoelectric motion. The process can be repeated several thousands of times per second, resulting in an almost continue motion of about 1 mm in few seconds. These motors are not always as simple as described above though they work under the same principle.

We used either Attocube® or mechonic® motors.

Figure 3.10: Pictures of the Attocube® (left) and mechonic® (right) (XYZ) systems.

The early days of the X-AFM

The initial idea of the X-AFM was to use the tip to locally measure the photoelectrons emitted from the sample while simultaneously acquiring topographical data. In this context naturally comes the idea of working in vacuum, since it reduces drastically the background of charges. Thus, the first prototype of an X-AFM was a vacuum X-AFM. This is shown in figure 3.11 and 3.12.

The first results were obtained at the ESRF beamlines with this vacuum version.

This set up had the difficulty that the vacuum pumps are usually mechanically noisy. It is definitely not the best situation in AFM. When the AFM image of figure 3.12 was taken an ionic pump was mounted below the AFM chamber. It was very time consuming because high vacuum has to be reached with a turbo pump (for ex.) before the ionic can be started. Additionally, if the mechanically stability is guaranteed by the use of an ionic pump the temperature stability is not. At the nanoscale the thermal expansion due to 1K is quite annoying. Finally, even though the chamber was equipped with several windows, including a beryllium one (for the X-rays in) it was not easy to have a clear macroscopic view of the sample, which is mandatory for preliminary alignments. To change the sample was also difficult and very time consuming.

Figure 3.11: Early AFM setup for combination with in situ X-ray experiments.

Furthermore, this version of the X-AFM could not be combined with diffraction experiments.

One step forward

After few modifications and versions, that we will skip, the project matured to a more friendly solution, lighter and wide open, as can be seen from figure 3.13.

The present version has the disadvantage that it is not high vacuum compatible. However, a primary vacuum can be set inside the X-AFM. Because it is hermetically closed can be filled or flushed with some inert gas as He.

AFM with the X-AFM

We show in figures 3.14 and fig:AFMImage4 some examples of AFM images obtained with the methods explained above and in particular with the last X-AFM version.

To conclude this section it is maybe worth pointing out that a typical time for an AFM image taken with a TF is of 1s per line, in the best case, and may go up to 3s per line if the sample is more difficult, i.e,. if it has more ups and downs. Since an image has at least 256 lines, a complete image then takes from 5mn to 15mn.

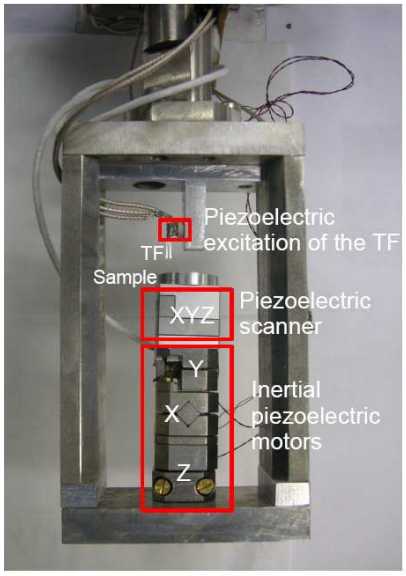

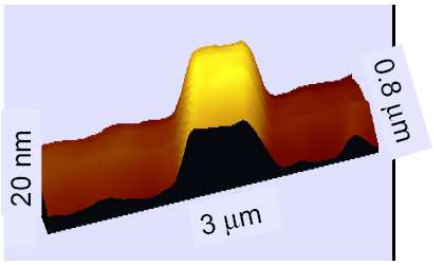

Figure 3.12: Left: Detailed picture of the vacuum X-AFM. The TF was glued on a piezoelectric dither. Piezoelectric motors were used for coarse motions and a piezoelectric scanner for the fine motions. Right: AFM image of a Nb line 10 nm height taken at ID27 at high vacuum with the X-AFM here on the left, and in figure 3.11.

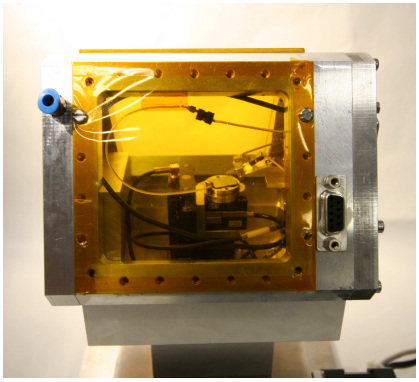

Figure 3.13: Picture of the X-AFM, now commercialized by *Small Infinity*. The triangular shape allows a wide range of incident angles for the X-rays. It uses the Mechonics inertial motors for the XY and Z coarse motions and a piezoelectric scanner for the fine motions. The TF is, as before, the force transducer for topography imaging.

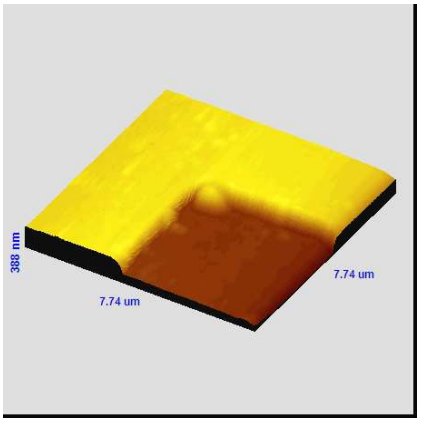

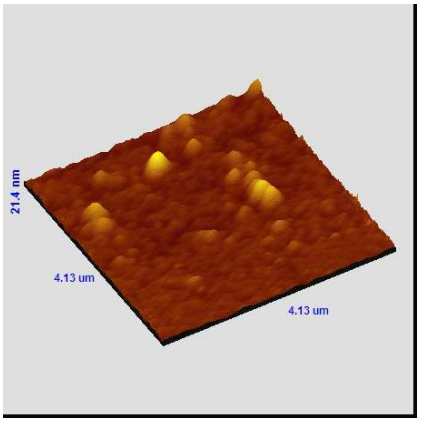

Figure 3.14: AFM images of a Si calibration grating. Both images where taken in one of the ESRF beamlines (ID26) to test the AFM in the real environment.

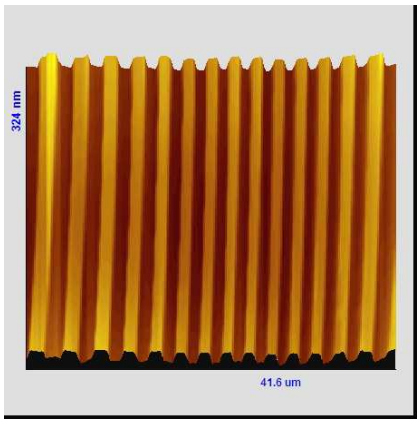

Figure 3.15: AFM image of a Si calibration grating taken at the Surface Science Lab. This was used to calibrate the AFM piezos.

3.4 A method to calibrate the tuning fork

An important parameter in Dynamic AFM is the amplitude of oscillation of the cantilever, in this case of the tuning fork. Even though we have calibrated the TF using an optical fiber, due to the fact that there is a mass on the TF or that the amplifiers used have different gains it is useful to be able to perform in situ calibration of the amplitude of oscillation.

This can be very easily performed when the oscillator is stiff enough that there is no jump to contact even for very small amplitude of oscillations. First, the oscillator is approached to the sample until the resonance frequency (or the phase) has shifted positively. This is done by choosing the adequate set point for the operation of the AFM control loop. Then one simply increase the amplitude of oscillation. The loop will move by the same amount. If the piezo is calibrated, as it should, then a plot of the position of the loop as a function of the measured amplitude gives us the calibration. This can be understood by looking at figure 3.16.

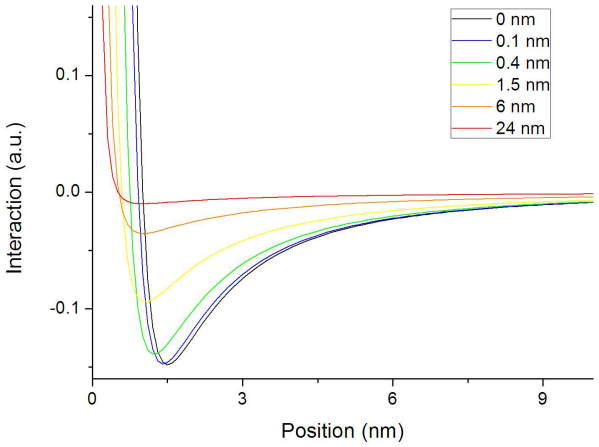

Figure 3.16: Approach curves for different amplitudes of oscillation. The XX axis is the distance from sample to the closest tip-sample position in an oscillation cycle.

In figure 3.16 it is plotted theoretical approach curves for different amplitudes of oscillation. The calculations where done assuming a Lennard-Jones like potential. The black curve is the limit of zero amplitude of oscillation and directly corresponds to the force gradient between tip and sample. The other curves are obtained by integration of the first (integration over the amplitude of oscillation) for different amplitudes of oscillation.

The curves are plotted as a function of the closest tip-sample position in an oscillation cycle. If we choose a positive interaction we see that as the amplitude (x_0) is increased the distance ($dz(x_0)$) between the sample and the bottom of the oscillation curve decreases. For higher amplitudes and same measured interaction, i.e., same setpoint, the tip gets closer to the sample. Therefore at every moment the loop will place itself at a distance:

$$z(x_0) = x_0 + dz(x_0). \tag{3.24}$$

As can be seen from figure 3.16 $dz(x0)$ is negligible compared to x_0. Thus, the approximation

$$z_0(x_0) \approx x_0$$

holds except for values of x_0 smaller than the nm. This is shown in figure 3.17.

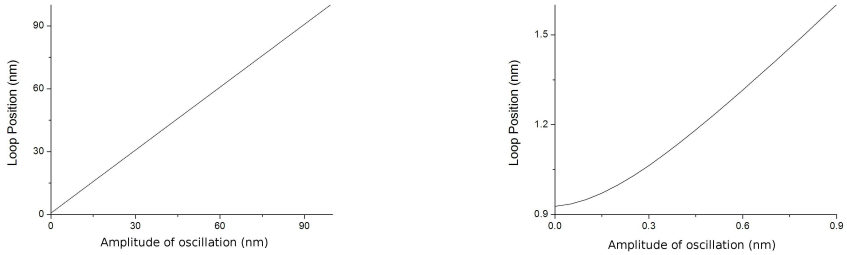

Figure 3.17: Loop position as a function of the amplitude of oscillation of the tip.

Thus, recording the position of the sample as a function of the amplitude of oscillation yields a direct calibration of the TF.

3.4.1 Experimental examples

Calibration of the higher mode of the TF (32 kHz)

This experiment was done using the higher tuning fork mode. The signal feeding the feedback loop is either the phase or the resonance frequency of the TF. The feedback loop is on and a certain time is awaited until it stabilizes. Then the amplitude of the excitation is increased and as a consequence the TF oscillation increases forcing the feedback loop to adjust the position of the sample. This is shown in figure 3.18 on left. On the right of that figure we plot the amplitude of oscillation as a function the sample position (topography).

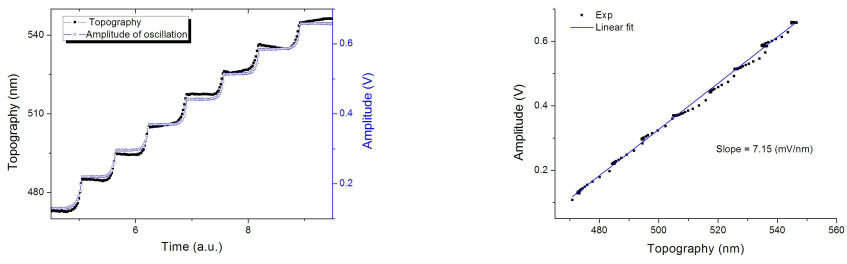

Figure 3.18: Left: Sample position (or topography) and response of the TF after the amplifiers. Right: Sample position versus amplitude of oscillation of the TF.

Calibration of the lower mode of the TF (18 kHz)

In the following example we will use the fact that both modes can be used simultaneously to calibrate the lower mode. This together with the previously described concept will allow us to take a complete resonance curve of a particular mode, in this case, the lower mode at about 18 kHz.

First, the TF is oscillated at its lower frequency mode, perpendicular to the surface.

The TF is also excited at its higher frequency mode, parallel to the sample.

The resonance frequency of the mode parallel to the surface increases when the tip-sample distance is reduced. This increase is monotonic and exponential as we will see in the next section. Because the increase is quite fast, as in the case of perpendicular oscillation (if we exclude the weaker attractive forces), the position of the feedback loop depends, approximately, only on the amplitude of oscillation of the lower mode of the TF, as described above. This approximation becomes more accurate as the exponential evolution of the potential becomes closer to a step function.

The result is that one can measure the Lorentzian response directly with the AFM z calibrated piezoelectric element.

A certain frequency shift of the parallel mode is chosen as the set point. During each oscillation, the feedback will try to maintain approximately constant the smallest distance to the surface. If the amplitude of oscillation of the lower mode is increased, the feedback responds accordingly.

The result is shown in the following figure:

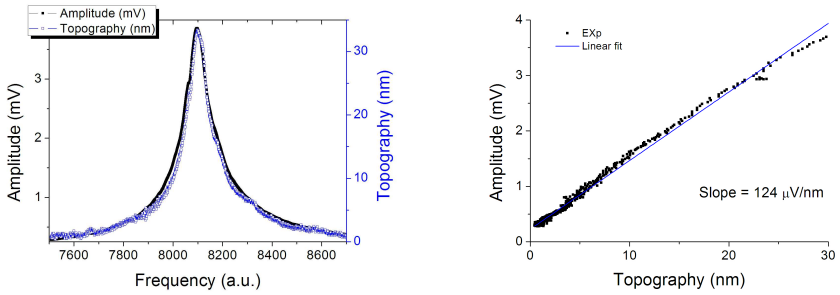

Figure 3.19: Left: Sample position (or topography) and response of the TF after the amplifiers. Right: Sample position versus amplitude of oscillation of the TF.

Comparing the slope on fig. 3.19 with that on fig. 3.18 we can see that the conversion of oscillation amplitude to generated current flowing through the contacts is about 60 times lower for the lower mode. This is due to the orientation of the piezoelectric crystal relative to the orientation of the contacts.

The total resonance curve was used intentionally to show the small non linearity due to the fact the potential is exponential rather than a step function.

3.5 Shear and friction forces

By shear and friction forces we mean the interactions that appear when a body moves parallel very near or in contact with another body.

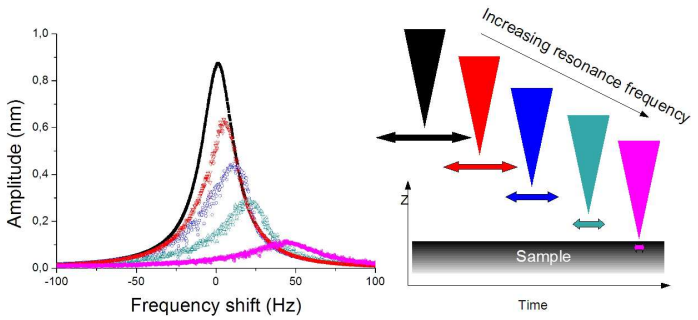

Figure 3.20: Observed resonances when the AFM tip oscillates parallel to the surface: as the distance between tip and sample is shorter the resonance frequency and the damping shift to higher values.

3.5.1 Introduction

When tuning forks entered the field of SPM they were being used mostly in the sub-field of SNOM (Scanning Near field Optical Microscopy) [50]. In this case they were used in a way such that the deflection was along the samples' surface. Generally an optical fiber was glued along one of the TF's prongs and the oscillation was then damped as the fibber was brought near the surface. Moreover, it seemed that a force, parallel to the motion, acting on the tip also exhibited a similar distance dependence. Some authors [51, 52] claimed that the damping occurred while the fiber or tip was still two tens of nanometers away from the sample's surface.

This seemed to be advantageous for combining SPM with Synchrotron techniques. However, we could not understand which physical principles were at the origin of these so called shear and friction forces.

As a matter of fact, other authors [53] were proposing mechanisms in which the tip mediates the interactions, i.e, that there was some sort of contact between the tip and the sample. Other authors [55] wonder about possible force fields acting on a tip oscillating parallel to a surface.

The scenarios of shear and frictions forces prior to our investigation were the following:

- there exists a dissipative force acting on a particle moving parallel to a surface
- there exists an elastic force acting on a particle moving parallel to a surface
- the distance at which these forces start to take place is not clear

- there are theoretical evidence that such dissipative force exists although with magnitudes several orders smaller than what is claimed by some authors
- there are experimental demonstrations of the existence of such dissipative forces but few orders of magnitude smaller of what claimed by some authors

The oscillator is initially defined by a centre frequency f_0 and a certain damping coefficient γ_0 which is related to the Q factor of the oscillator. When it is brought close to the surface both f_0 and γ_0 increase their values to $f_i = f_0 + f_{ts}$ and $\gamma_i = \gamma_0 + \gamma_{ts}$.

If we assume the smallest frequency shift possible to measure with a TF is 0.1 Hz then this corresponds to a force gradient of about 300 pN/nm.

The width of the resonance curve is initially $\gamma_0/(2\pi m_r) \approx 10Hz$. If we assume to be able to measure changes of 0.1 Hz then we could observe dampings of $1 \times 10^{-9} kg/s$.

In the article of Stipe et. al. [54] where they used an extra sensitive cantilever to probe these forces the highest value of γ_{ts} is of only $10^{-12} kg/s$, five orders of magnitude smaller than what can be measured with a bare TF. Moreover, this small value corresponded to a distance of 2 nm according to the authors.

On the other hand, K. Karrai and his co-authors measured at a distance of 10 nm, changes in the FWHM of the response of the order of $10s^-1$. This multiplied by the reduced mass of the oscillator gives damping coefficients of the order of $2 \times 10^-6 kg/s$.

Given that both authors used gold tips and worked in vacuum, the difference between the experiments must be due to the different samples. The sample was either gold on mica or Silica, gamma irradiated and non gamma irradiated in the first case and cleaved graphite in the second.

It is not expected that the sample characteristics would play a role of six orders of magnitude. Moreover, the three samples of Stipe showed differences of only one order of magnitude between the three samples. Irradiated silica damped the oscillator more than non irradiated silica which in turn damped the oscillator more than gold (111).

Two questions rise:

Which is the origin of these forces? Finally, if used for distance control which is the real tip-sample distance.

It is worth mentioning that an explanation had already been given by Gregor et. al. [53] that involved some tapping.

The time that was allocated to the study of these interaction phenomena, was unfortunately not enough to give a conclusive answer to the first question, but sufficient to answer the second one [1].

3.5.2 Experimental Results

The general behaviour of friction and shear force are shown in figure 3.21 where is shown the evolution of the oscillator response for different tip-sample dis-

[1] This research was not of direct importance with the rest of the thesis, and implied considerable changes in the set up. Though several measurements were done in air and vacuum and with different tip shapes. Part of the information relative to shear and friction force experiments was lost (among other things) as a consequence of the robbery of 3 logbooks.

tances. The response remains linear until one can no longer obtain a resonance curve. In figure 3.21 the distance from the first to the last curve is of about 30nm.

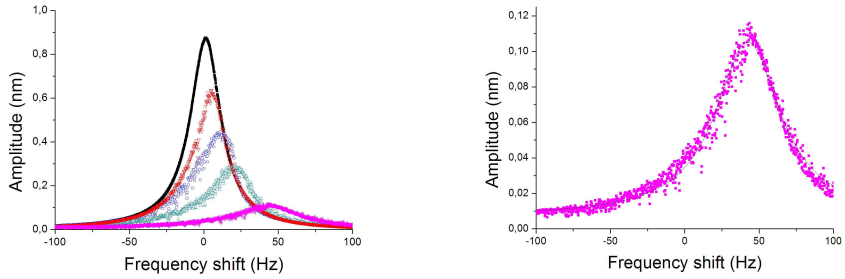

Figure 3.21: Oscillator response for different tip-sample distances (left). The distance between each curve is not constant but roundabout 5 to 7nm. The response remains linear after 30 nm from the onset of interaction.

One of the most intriguing aspects was the smooth exponential decrease of the oscillation amplitude as seen in figure 3.22. One would expect that if it exist a non contact mechanism different from the contact one there would be a fast change from one to the other. Similarly to the tunneling effect or Pauli repulsion. Thus this smooth decrease seem to indicate that there is only one regime probed.

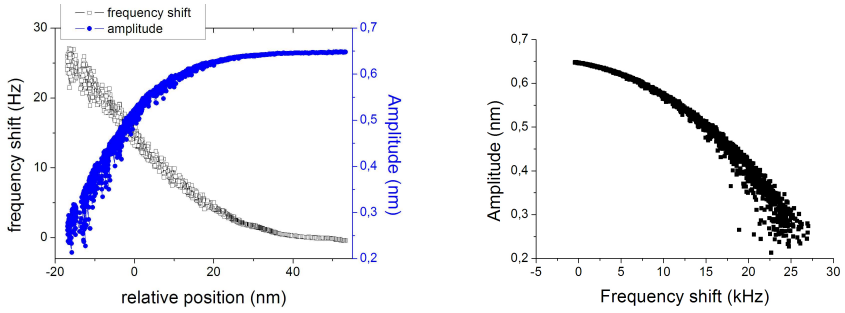

Figure 3.22: Oscillator amplitude and resonance frequency shift evolutions as a function of the tip-sample distance (left). Oscillator amplitude as a function of its resonance frequency indicating a possible correlation between them.

We have performed several attempts to detect contact using the onset of tunneling current. Unfortunately, the results were not reproducible. This was due to the experimental set up, that at that time was not good enough for tunneling measurement. We occasionally had tunneling before shear or friction forces.

We have performed several experiments in air and in high vacuum but observed no particular difference between them.

Other experiments were done with different tip apex radius. The results were similar for all tip apex radius, with the difference that the evolution of both amplitude of oscillation and resonance frequency was faster for larger tips.

Finally we have also applied an electric field between tip and sample but again no difference was found. This rules out, at least in the range of our experiments, a mechanism of the ionic pump type proposed by Karrai, where an electric field between the tip and the sample attracts charges particles to vicinity of the tip causing the observed increase in the damping and resonance frequency. We note however, that Stipe did find a dependence on the electric field applied, but the range of forces in which his experiments where done are much below the ranges probed here.

Finally, we have obtained no particular difference between conductive or isolating samples. The tip was always a conductive tip, tungsten or gold.

We have then realized that one could use simultaneously two orthogonal modes of the TF. This makes it possible to combine lateral forces with normal forces. The idea is that normal force is very well described in literature and the onset of contact easy to tell. Moreover, it can be used to study shear and friction forces both in conductors and isolators unlike in the case where the onset of contact is evidenced by a tunneling current.

Shear and friction forces seem to happen at the onset of contact

To measure the shear forces and detect from which distances do they start to play an important role, we have measured them whilst measuring the component of the force gradient normal to the surface. For that we have simultaneously used both symmetric modes of the tuning fork: $f_t = 18kHz$ and $f_l = 33kHz$. We have utilised one lock-in to excite and detect the lower resonance frequency of the TF (16 kHz with tip) oscillating normal to the surface; and one PLL to excite and detect the higher mode (30 kHz with tip) oscillating parallel to the surface. The experimental setup is as in figure 3.7.

Both modes were excited acoustically. In figure 3.23 is shown the evolution of both TF modes for distances close to contact.

Note the much larger variations relative to the mode oscillating perpendicular to the sample. The amplitude change is of 50% and the phase change is of several tens of degree corresponding to several Hz. For the lateral mode the amplitude change is less than 15% and the resonance frequency has hardly changed when the tip is already in contact with the sample.

On the left of figure 3.23 we show a zoom out of the interactions.

3.5.3 Conclusion and perspectives

One obvious conclusion is that, independently of the origins of these forces, they are less sensitive to the presence of the surface than the usual perpendicular mode. On the other hand, if the technique is supposed to be non-destructive then the forces involved ought to be small. In the case of shear or friction forces they are small even when the tip is already in contact. However, it is our belief that these forces, in the range experimented here which is typical, are essentially arising from contact. The frequency shifts are then the result of the tip bending while in contact. A non contact microscopy method using these forces should be carefully thought [56]. As a matter of fact, even if there would be no contact, the old rule of physics, *action reaction* still rules and imposes that if the sample has an effect on the tip, the tip has an effect on the sample, whether there is

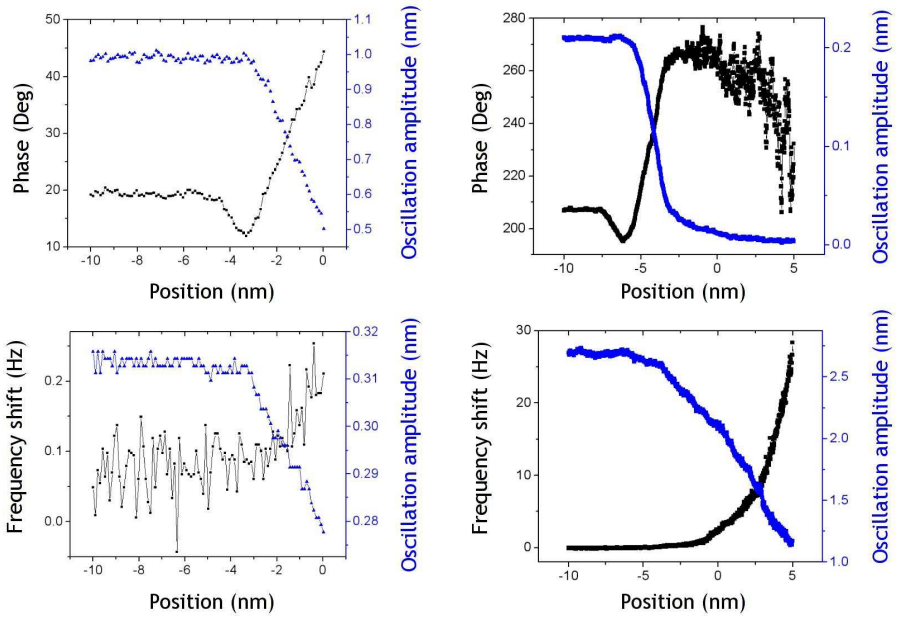

Figure 3.23: Top: Amplitude and phase shift of the mode oscillating perpendicularly to the surface. At the bottom: Amplitude and frequency shift of the mode oscillating parallel to the surface.

contact or not is a matter of point of view (it is not relevant), what is of matter is the intensity of the involved forces.

We also believe that the combination of the two modes can be potentially used for spectroscopy. If the perpendicular mode gives us the normal load then shear force can be used as a chemical probe by measuring different damping in different samples at an equal normal load. The modes combined together may possibly give real time chemical resolution since they can be used together whilst taking an AFM image.

3.6 Conclusions

In this chapter we have seen how easy is to use the TF together with a tungsten etched tip as a force transducer.

The TF is perfectly suited for making up an atomic force probe.

A comparison between a conventional cantilever and the TF leads to the conclusion that they can probe similar interactions even though they exhibit very different spring constant.

The sensitivity, in fact, depends on the dynamic spring constant that can be defined as:

$$k_{dynamic} = \frac{k}{Q} \tag{3.25}$$

The higher Q factor of the TF leads to higher settling times ($\approx$ 300ms)

when compared to a Si cantilever ($\approx 30ms$). The consequence is that the measurements are intrinsically slower whether they are made using a lock in or a PLL.

The AFM images taken with the methods described here resemble the images taken with more conventional approaches.

The TF, together with its tip, was also used in the context of an atomic force probe to study the interactions between a body moving parallel to a surface and the surface. The main conclusion is that the forces become important only when the tip is at the onset of contact with the sample.

Chapter 4

An AFM in a Synchrotron's sample holder

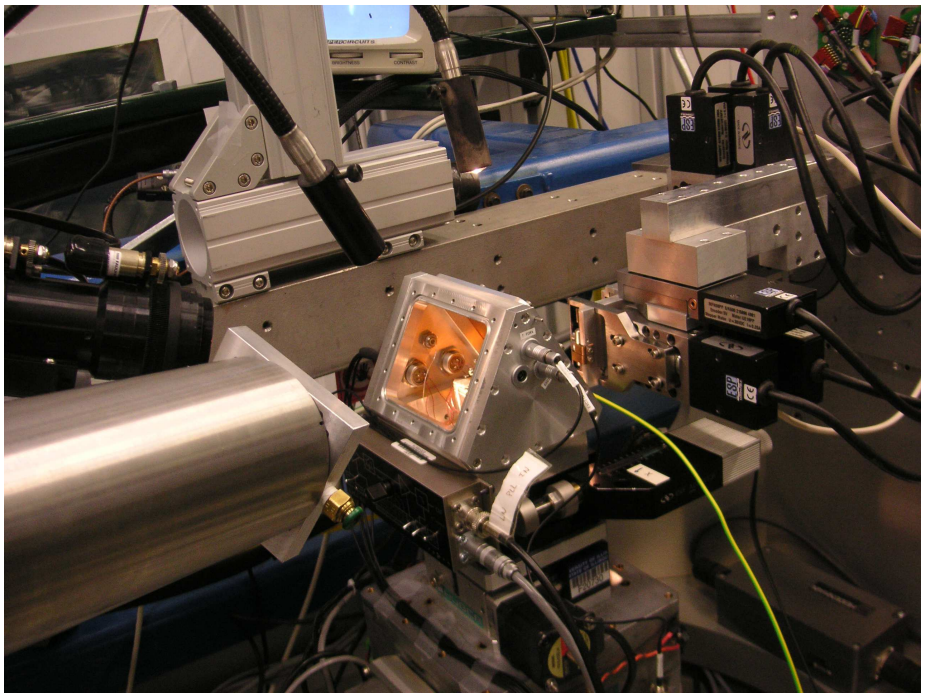

Contents

4.1 Introduction

This chapter concerns the development of a new instrument and new techniques that will allow a mutual cross-fertilization between Synchrotron Radiation (SR) and Scanning Probe Microscopy techniques, in particular AFM. The combination between SR and SPM techniques may, however, be more advantageous if other SPM techniques, in particular EFM (electrostatic force microscopy), SCM (scanning capacitance microscopy) or STM (scanning tunneling microscopy) are used for the combination, as discussed in the introduction.

Before proceeding one must first introduce the synchrotron, its origins, the main objectives and the techniques to achieve those objectives. Focus will be given to those techniques which contributed to the present thesis.

The Synchrotron

It is perhaps interesting to see how the synchrotron is presented to the general public. In the home page of the ESRF, the third largest synchrotron in the world and the most important in terms of published articles, can be read:

The thirst for knowledge drives us to explore the world around us. What is our planet made of? What are the processes that sustain life? How can we

explain the properties of matter and develop new materials? Will it one day be possible to conquer viruses, predict natural catastrophes or eliminate pollution?

Most of these questions cannot be answered without a profound knowledge of the intimate details of the structure of matter. To help in this quest, scientists have developed ever more powerful instruments capable of resolving the structure of matter down to the level of atoms and molecules. Synchrotron radiation sources, which can be compared to "supermicroscopes", reveal invaluable information in numerous fields of research. There are about 50 synchrotrons in the world being used by an ever growing number of scientists.

The three largest and most powerful synchrotrons in the world:

Figure 4.1: The three largest and most powerful synchrotrons in the world: The *Advance Photon Source* in the USA, the European synchrotron Research Facility in France and *Spring-8* in Japan.

More specifically a synchrotron is used to study any type of material, condensed or not. What is specific about this? The techniques used!? There are as many techniques as ways we can combine 3 or 4 letters in the alphabet! The specificity is the study of the electronic and geometric structure of matter above the atomic scale trough the use of collimated X-ray beams. But how are the photons in the beams used, that is up to one's imagination!

A non extensive list of the techniques is:

EXAFS	Extended X-rays Absorption Fine Structure
DAFS	Diffraction Anomalous Fine Structure
XANES	X-ray Absorption Near Edge Structure
MAD	Magnetic Anomalous Diffraction
SAXS	Small Angle Scattering
GiSAXS	Grazing incidence Small Angle X-ray Scattering
PES	Photoelectron Spectroscopy
ARPES	Angle resolved PES
XIFS	X-ray Intensity Fluctuation Spectroscopy
and so on	...

Some of these techniques are introduced below. The common element to all these techniques is that all of them use photons and in all of them it is measured the interaction of photons with electrons, or specific electrons bound or unbound to a nucleus. Hence, materials with low density of electrons are more difficult to measure, thus the high intensity of the beams is quite handy, specially when the samples are small, like biological crystals difficult to produce with large volumes.

Why and how are there so many techniques? There are several aspects that explain such a number of different techniques. At SR facilities (specifically 3rd generation) one finds the main features [57]:

1. A broad spectrum of the light; which allows to explore very different energy ranges, from the meV up to more than 100keV, thus it allows to explore from the almost free electrons up the the most binded ones.

2. High intensity; which allows short acquisition times and tiny samples can be investigated

3. High degree of collimation; allowing for very high angular resolution

4. Linear polarization in the plane of orbit and circular polarization allowing linear and circular dichroism measurement

5. high brilliance of the source

6. time structure; pulse duration as short as 50 ps

Since the usual speed of electron in a synchrotron are very close to the speed of light, the properties of SR can be understood from the picture of an oscillating dipole subjected to a Lorenz transformation [58]. One of the effects of the electrons being relativistic is that the angular distribution of the radiated waves is strongly distorted into a narrow cone in the direction of the electron trajectory whilst the emitted spectrum is strongly Doppler shifted. For non relativistic electrons the emission is a cardioid. The increase in energy due to the Doppler shift goes from the microwave range up to the hard x-ray regime. The critical wavelength can be used as a reference.

$$\lambda_c = \frac{4}{3}\pi R\gamma \tag{4.1}$$

with $\gamma = E/m_0c^2$, where m_0c^2 is the electron rest mass energy, R is the bending radius of the electron orbit. At SPRING8 in Japan the energy is of 8Gev and the bending radius is R=39 m, whence we find $\lambda_c = 0.429$ Å.

The European Synchrotron Radiation Facility

The European Synchrotron Radiation Facility is an international institute funded by 19 countries. It operates Europe's most powerful synchrotron light source and hosts 6000 scientific user visits per year for 900 different experiments.

The ESRF was the first 3rd generation synchrotron to be built and was open to users in 1994.

All of the experiments presented in this thesis that involve Synchrotron Radiation where performed at the ESRF.

4.1.1 Basics of X-ray Absorption

It will now be introduced the main aspects of X-ray absorption. The idea is to go **only** trough the necessary aspects and notations required for the understanding of the rest of the present thesis.

The particular feature of X-ray absorption spectroscopy (XAS) are the fact that it is element specific, i.e., electrons in different atoms are at different energy levels resulting in different spectral lines, and unlike diffraction, XAS does not require any long range ordering. However, as will be seen, some ordering provides additional information. XAS is closely related to the empty density of states, consequently it provides useful information of the local electronic structure of the chemical element studied.

We recall here Lambert-Beer's law which gives the intensity $I(\omega)$ after a beam with incident intensity $I_0(\omega)$ as past trough a slab of thickness t:

$$I(\omega) = I_0(\omega)e^{-\mu(\omega)t} \tag{4.2}$$

where $\mu(\omega)$ is the absorption cross section, strongly dependent on the sample's composition. It presents, sharp steps denominated absorption edges, which are the result of the incident photon having an energy close to the energy of an electron binded to a specific shell. The position of the steps slightly depends on the chemical arrangement of the particular atom being studied for example it depends on the oxidation state of the atom. Furthermore, $\mu(\omega)$ may present some oscillations after the edge which are the result of the interaction between differently scattered electron waves. This richness in fine structure makes XAS an important tool for the characterization and study of any type of materials i.e, atoms, molecules, surfaces, adsorbates, solids and liquids.

The measure of $\mu(\omega)$ is one of the most common tasks in a synchrotron. However, there are several ways to measure it. One can simply measure the intensity before and after the sample. This is transmission detection and is the most direct measure of $\mu(\omega)$, specially when hard x-rays are used. For soft X-rays ($< 1keV$) the attenuation length is less than $1\mu m$ which implies samples extremely thin. In transmission the sensitivity to the sample's surface is weak or non at all depending on the specimen thickness. However, the absorption can also be obtained from the decay of the created core-hole, which gives rise to an avalanche of electrons, photons and ions escaping from the sample's surface. Thus, one often measures the fluorescence or the photoemitted electrons.

X-ray Absorption Near Edge Structure

The X-ray Absorption Near Edge Structure (XANES) is obtained when the energy of the incoming X-ray beam is scanned around the edge. For a noble gas, where the interaction between different atoms is weak, such scan will result in a sharp step at the energy of the edge. However, for condensed matter the electron clouds are deformed due to the neighbour atoms. This deformation leads to slight shifts in the energy of the edge or to a deformation in the step shape. These deformations appear at energies close to the edge (before and after) and are usually referred to as *near edge structure*. The spectral information contained here gives information about the electronic properties of the absorbing atom and depends on electron correlation and on the density of empty states above the Fermi level [59, 60, 61]. The electron escaping the absorbing atom propagates toward neighbor atoms and is then scattered back. For electronic waves of low energy the scattering process goes on and on, and this leads to a modification of the final state of the transition cross-section.

White line

The dependence of the absorption on the empty states is extremely illustrative at the near edge region. For some materials it can be observed an intense peak just at the edge jump. This peak is usually called white line. In general its intensity decreases as we go from the left to right on Mendeleev's table.

Extended X-ray Absorption Fine Structure

When a photon is absorbed by an atom above the edge, the excess energy takes the form of a photoelectron leaving the atom in an excited state. Since electrons are wave like particles they interfere with the wave reflected back, changing then the final state, thus increasing or decreasing the probability of absorbing the incoming photon. Naturally, the condition for constructive or destructive interference depends on the path traveled by the electron waves i.e., the position of the atoms relative to each other, and on the photoelectron wavelength which, in turn depends on the energy of the incident photon. This results in oscillation of absorption probability as a function of incident photon energy. This is often referred to as EXAFS (Extended X-ray Absorption Fine Structure) oscillations. They are visible few eV after the edge up to some thousand eV after the edge. From their periodicity one can calculate the distances to first, second and often third neighbour, depending on the quality of the data. Moreover from the intensity of the oscillations one obtains information about the coordination number, disorder parameters and the Debye Waller factor. Notice, it is possible to determine inter atomic distances even if there is no long range ordering contrary to diffraction [62, 63].

Decay channels

After the absorption process the absorber atom is left in an excited state. To relax there are two competing channels, fluorescence and Auger emission. They both originate from the extra energy liberated after an electron from a shallower energy level has replaced the core hole. For light atoms the decay is more likely to be trough Auger emission, whereas for heavy atoms the emission of a photon (fluorescence) is the preferred decay channel. Both emissions have very well defined energy levels. However, only absorption very close to the surface, typically few Å, will result in emission of photoelectrons with those well defined energies. Electrons produced at greater depths (Auger or photoemitted) undergo inelastic scattering whilst thermalizing. This thermalization leads to emission of electrons with a continuum of energies down almost to 0eV. If the photon absorption happens at depths greater than typically few tens of nm, then complete thermalization inhibits the electron escape. Notice however, that at energies close to the edge, the cascade of electrons is more likely to originate from Auger electrons since these have energies much higher than the photoemitted electron. Auger spectroscopy has proved to be a useful tool for chemical analysis of surfaces, whilst a number of techniques for analysis of the electronic structure in materials is based on photoemission spectroscopy [64, 65].

In the case of fluorescence, the signal is coming from a depth related to the absorption length of the material studied, for the energy of the outcoming photon. This is somewhere from $1\mu m$ up to $100\mu m$ depending on the specimen. As an example around 1.8 keV the attenuation length in Si varies from $14\mu m$,

just below the edge, to about $1\mu m$ at the Si K edge. For a given energy the attenuation length decreases with the electron density of the material.

Measuring either the fluorescence or the outcoming electrons makes it possible to measure the absorption because there is an approximate linear relationship between the decay channels and the absorption cross-section [66, 60].

Total Electron Yield

A simple experimental scheme, that allows to measure the absorption edges is the Total Electron Yield (TEY). Here all electrons that emerge from the sample surface are measured regardless of their kinetic energy. The probing depth is of few nm up to few tens of nm depending on the materials studied and on the incident photon energy, thus the sensitivity to the surface is very high because the attenuation of the electrons by the material occurs much faster than in the case of photons, i.e. electrons interact more (have higher cross-sections) with matter than the photons.

In this thesis the TEY detection was the envisaged experimental method for combining the spatial resolution of an AFM with the chemical information contained in $\mu(\omega)$. However, in practice, a mix of TEY and fluorescence was always measured. This is because the AFM tip used as probe cannot directly distinguish photons from electrons. A double phase lock-in, may, however, give some insight on whether photons or electrons are measured.

4.1.2 Basics of Diffraction

Diffraction involves the illumination of a crystal sample, or an ensemble of crystals. Each atom will potentially interact with the incoming electromagnetic wave or photon and diffuse it. If the material is ordered then conditions for constructive and destructive interference exist. This results in a diffraction pattern. The condition for this is given by Bragg's law:

$$2d \sin\theta(1 - \delta/\sin^2\theta') = m\lambda_m \tag{4.3}$$

where λ is the wavelength of the incoming radiation, $(1 - \delta)$ is the real part of the refraction index. The factor $(1 - \delta/\sin^2\theta')$ is often considered to be equal to one, yielding an approximate relationship where d is the distance between diffracting planes and θ is the angle between these planes and the radiation, or the Bragg angle. For a certain set of planes there is a characteristic angle that fulfils the diffraction condition for a given energy.

In the present context diffraction was measured from single crystals [67]. Light of a well known wavelength is impinging on the crystal. The crystal is rotated by ϕ in the plane perpendicular to the beam and by θ, the angle of incidence, so that the lattice planes are well oriented in the reference frame of the beam. A scheme illustrating ϕ and θ is given in figure 4.2.

Crystal truncation rod

For an infinite crystal the diffraction can be seen as the Fourier transform of the electron densities. Characteristic distances in a crystal result in characteristic angles for which equation 4.3 is satisfied. It results then as an ensemble of peaks, constituting the diffraction pattern, from which the inter atomic distances can

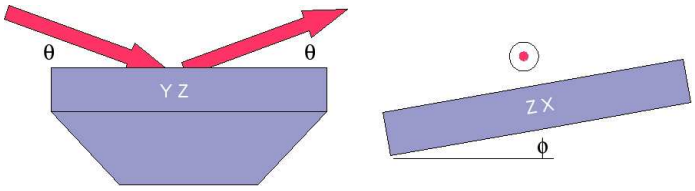

Figure 4.2: Scheme showing the definition of θ and ϕ.

be calculated. The fact that the crystal has a surface, or that it is not infinite, is equivalent to multiply the infinite crystal by a box function. The peaks, then will be convoluted with the Fourier transform of the box, that essentially will link all the peak along the vertical to the sample. They are truncation rods [68].

Diffraction Anomalous Fine Structure

DAFS stands for Diffraction Anomalous Fine Structure and is a less common technique [69, 70, 71] that combines diffraction with absorption simultaneously. Here one looks at the intensity of the diffracted X-ray as the energy of the incoming photons is scanned across a particular absorption edge. Thus, information similar to that contained in XANES or EXAFS is combined with diffraction information. One can think of it as diffraction sensitive to a particular atomic specimen or XAS from a particular atomic species in a particular site. Hence, it is a site selective tool, given by the particular diffraction condition. This information is combined with the chemical information contained in the change of the diffraction intensity as the beam incident energy is scanned across a given edge.

Coherent diffraction

In most diffraction experiments one looks at an ensemble of Bragg peaks which have spatial periodicity related, trough the Fourier transform, to the spatial periodicity of the atoms in a crystal. However, a Fourier transform of the crystal in the real space to the reciprocal space shows fringes which are related to the crystal size. These fringes are most of the times absent from the diffraction data because X-ray light is only partially coherent. Transversal coherence in modern synchrotrons goes from few tens of microns to microns, depending on energy. This partial incoherence destroys the pattern of fringes. However, if a crystal is smaller than the coherence length of the light shining on the crystal one should see such fringes. The Fourier transform from the reciprocal space to the real space gives not only the internal periodicity of the crystal but its shape. This technique also allows to map the strain field inside the illuminated crystal [4, 5]. For this reason we have tried to combine coherent diffraction data with contact stiffness (see below: **Indentation with a tuning fork**) to study mechanical properties of gold nanocrystals.

4.2 Experimental Set up for the XAFM

It will now be described the general set up for combining X-ray spectroscopies with AFM. We will refer to the instrument used as XAFM. Pictures of it have already been shown in the previous chapter.

The basic idea is to have a functional AFM that allows illumination of the sample with the X-rays in a wide range of angles. The AFM tip will always be used to map the X-ray beam position. Furthermore, the tip can be used to locally measure the sample X-ray absorption in TEY mode, or the X-ray diffraction. The general setup is shown in figure 4.3.

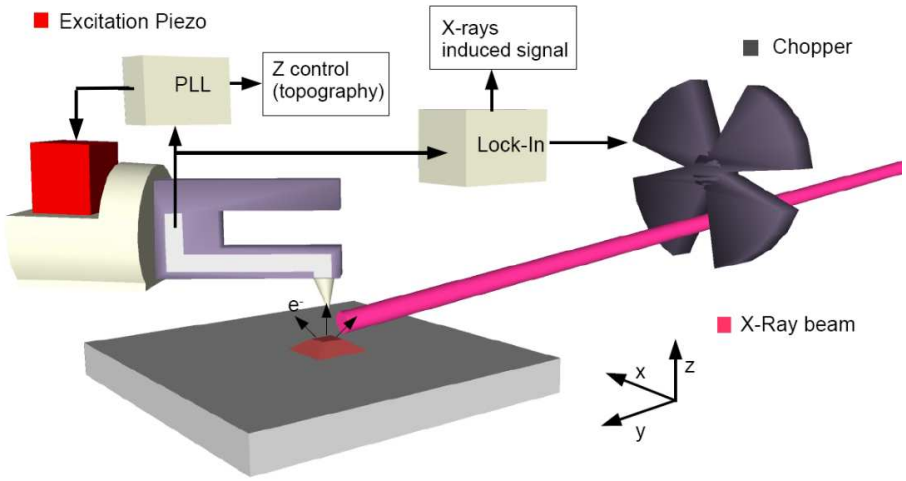

Figure 4.3: Experimental set up: A tuning fork with a conductive tip is used to obtain an AFM topography of the sample. Its oscillation signal is demodulated, typically with a PLL. A small piezoelectric dither is used to provide mechanical excitation of the TF. The conductive tip is also used to measure the signal directly or indirectly caused by X-ray absorption either from the sample or tip or diffraction from the sample. The X-rays are time modulated thus its induced signal collected by the tip is time modulated too.

The working principles of the AFM based on the tuning fork have already been explained before. It must now be added that the signal from the TF is now the sum of two signals:

- A current signal due to its oscillation (i_o)
- A current signal directly or indirectly induced by the X-rays (i_x). This can be either due to sample photoelectrons impinging on the AFM tip or

due to photoelectric effect on the tip caused by direct exposition of the tip to the beam or due to photons that are diffracted from the sample toward the tip

The tip is electrically connected to the electrode read by the preamp and through it, it is connected to a virtual ground whereas the second TF electrode is grounded.

Both current signals are time modulated which allows their separation trough the use of lock-in or PLL amplifiers. The time modulation on i_o is given by the resonance frequencies of the TF, whereas there are some freedom choosing the frequency of the second signal (i_x). To modulate the X-rays signal a mechanical chopper, shown in the scheme of figure 4.3, is placed before the XAFM. These choppers can't work at frequencies higher than few kHz. It is important to be as far as possible from the so called *f corner* and on the other hand have the chopper working with stability.

4.2.1 Chopper and lock-in

The use of a lock in to detect the signal induced by the X-rays allows not only separation of the two signals (i_o, i_x) but also strongly reduces the background because of its extremely reduced bandwidth. The frequency of the chopper was typically between 1 to 3 kHz. The smallest possible signal measured with it was correspondent to few hundreds of fA. The preamp gain was usually the same used for amplification of the oscillating TF signal, i.e., $10^7\Omega$. 100 fA corresponds to a preamp output of few μV connected to the lock in input. This corresponds to about the background as measured by the lock in, and thus indicates the limit with the present experimental scheme.

The lock in is very sensitive to phase changes (see previous chapter). This fact makes it very simple in some cases to distinguish photons from photoelectrons. When the beam is on the tip the current is expected to be in phase with the incident beam. To be noted that the characteristic time scales for absorption and emission of photoelectron are much, much smaller than $1/f$, with f the frequency of the chopper. On the contrary, when the beam is illuminating the sample the same photoelectric effect produces a tip current (if the emitted electrons go in the tip's direction) which lags in phase by π. However, if the sample diffracts the photons then again the current should be in phase with the beam. A simple example is shown in figure 4.4.

The sample is substrate of Si where SiGe islands were epitaxially grown.

The X-ray beam is initially illuminating the tip, this corresponds to beam position (I) as illustrated in figure 4.4. Initially, the absolute signal (in phase and out of phase) is of $100pA = 100 \times 10^{-}12C/s \approx 2 \times 10^7 e/s \approx 10^{-}6 I_0 e/s$.

As the beam moves vertically from the tip to the sample, it goes from illuminating the tip to illuminate the sample. The current goes to a minimum when the beam is in between the sample and the tip (II).

The beam then illuminates the sample (III), and photoelectric effect causes electrons to escape the sample's surface toward the tip.

More examples of this will be shown along this chapter.

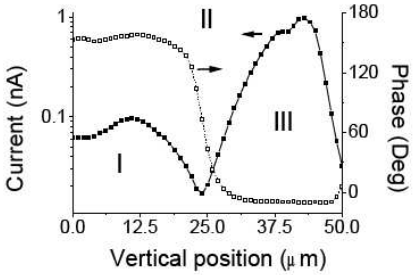

Figure 4.4: (region I) the X-ray beam is initially illuminating the tip, (region II) as the beam moves vertically from the tip to the sample, it goes from illuminating the tip to illuminating the sample. When the X-ray beam is between the tip and the sample a local minimum appears. (region III) 180 Deg phase change indicates the tip is collecting photoelectrons from the sample.

4.3 The tungsten tip as a detector and as a sample

The first step of any experiment with the XAFM is the alignment of the X-ray beam with the XAFM tip. This is easily done because once the beam illuminates the tip, a cascade of electrons due to photoelectric effect will flow out of the tip. A scan around the position of the tip will produce its photoelectric image, thus giving its coordinates relative to the beam.

To further understand how easy/difficult is to align the tip with the beam we must first consider how the absorption gives rise to a current. Also, the tip itself is an interesting sample.

4.3.1 Absorption by the W tip

The Total Electron Yield (TEY), due to tip photoemission after illumination with a synchrotron X-ray beam, produces a measurable current, shown already in the previous section. This has been systematically recorded as the tip is moved in the XZ plane perpendicular to the beam, thus producing experimental images of the tip as shown in fig. 4.5 (left), also shown is a fit to the data (right) as discussed below. The energy of the photons was about always in the range between 10keV to 13keV. The beam size is about $7(\mu m)^2$.

A characteristic feature of this type of scans is an increase in the current when the X-ray beam is at grazing incidence on the tip. This produces the higher contrast on the tip edges well visible in fig. 4.5. This higher contrast is only due to the geometry of the incidence since the current is proportional to the illuminated area and at grazing incidence this area is maximized. If the area is larger, then there is more absorption happening near the surface, thus more electrons are likely to escape.

The relevant parameters for analysing the experimental results of figure 4.5a are the absorption length α (which is of few microns for the energy used), the inelastic mean free path for e^- in solids λ (which is typically of few nm), and the characteristic energy loss per unit of length i.e., the stopping power S(E) for electrons.

In order to quantify the results, we define the effective escape depth d_{eff} as the depth for which there is a probability 1/3 that a photon absorbed at a

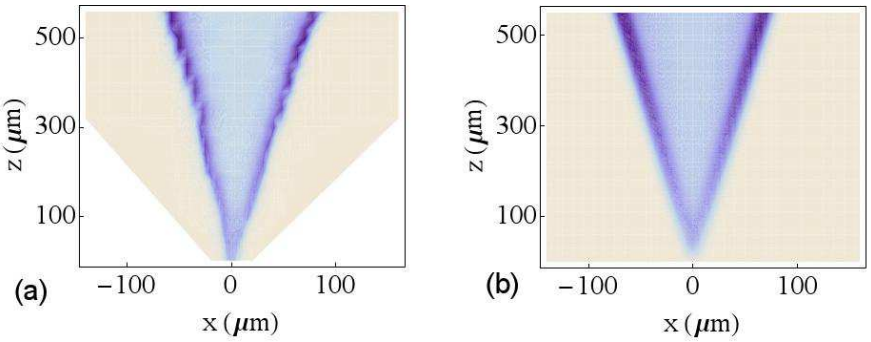

Figure 4.5: a) 3D plot of the current flowing from the W tip as the tip is moved in the XZ plane perpendicular to the beam. b) Fit of data a)

.

distance smaller than d_{eff} will result in one electron escaping the tip. The other e^- go further deep into the tip and do not escape. The factor 1/3 corresponds to half the height of a cylinder with the same volume as a unit sphere, and accounts, in approximation, for all possible directions of the e^-.

Considering the complexity of the photon absorption processes, the conversion into electrons, and how these electrons loose their kinetic energy, it is clear that such a definition is oversimplified. However, it is sufficient to take into account the experimental results and provide a reasonable analysis.

We calculated the intensity of the current $i(x, z)$ taking into account the 2D Gaussian beam shape and the linear absorption length on W for photons of 10 keV ($\alpha = 5.8$ μm). The current is then given by:

$$i(x,z) = \int I(x,z)\frac{1}{3}f(x,z)(1 - e^{-t(x,z)/\alpha})dxdz \tag{4.4}$$

$I(x, z)$ is the Gaussian distribution of the photons, $f(x, z)$ takes into account only the number of photons that are absorbed at a distance smaller than d_{eff} from the surface and $t(x, z)$ is the length along which the absorbed photons produce measurable current. Both $f(x, z)$ and $t(x, z)$ depend on the geometry of the tip as well as on the beam-tip geometry and therefore both depend on the parameter d_{eff}. If the radius of the tip is smaller than d_{eff} then $f = 1$ and $t(x, z)$ is simply the thickness $t = \sqrt{R(z)^2 - x^2}$ with $R(z)$ being the radius of the tip at position z. If the radius of the tip is much larger than d_{eff} and the beam is incident on the tip perpendicular to it, then $t(x, z) = d_{eff}$.

On the basis of this calculation we can now estimate d_{eff}. Figure 4.5b, and 4.7 show the agreement between measured and calculated current versus the tip position relative to the beam. The only adjustable parameter is d_{eff}. All other quantities are derived from experimental conditions. From our experiments, we systematically obtain d_{eff} of about 30 nm.

We note that in the context of this work, this is an important figure since it indicates how deep the surface is probed and gives an insight into the best possible lateral resolution. Neglecting any issue of convolution with the tip shape, the best possible lateral resolution in total electron yield collection cannot be better than this value, that in turn is material dependent.

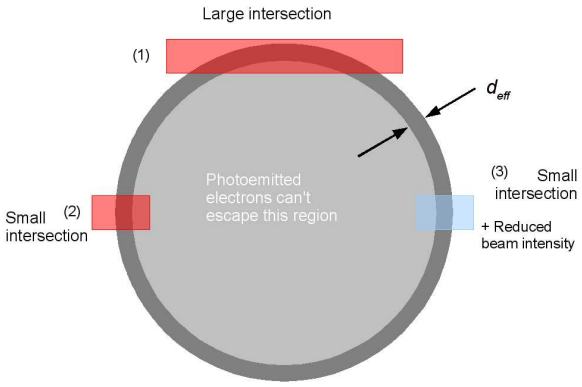

Figure 4.6: Scheme illustrating how the geometry of the beam incidence changes the measured current. Two situations are considered: (1) incidence at the edges: corresponds to the most favourable situation, since the intersection of the beam with the region near the surface is maximized; (2+3) incidence at the centre: is the most unfavourable, since the intersection is in this case the smallest possible. The part intersected at (3) is negligible until the tip is illuminated at a position where its diameter is smaller than the absorption length for X-rays in the material (Typically few μm).

Absorption edge of the tungsten tip

When combining TEY measurements with AFM, the goal is to have topographical and chemical information simultaneously. Hence, one should be able to detect the absorption edges with the tip. Because the tungsten tip is the detector, one should be able to easily measure the tungsten edge. The tip thus becomes both the sample and detector.

Such measurement is shown in figure 4.3.1.

Data with quality better than the one obtained here will hardly be obtained using other sample than the tip, because here the measurement is done with the material that is absorbing the incoming radiation. Of course if a material with higher Auger yield (lower Z) is the sample, then more electrons are emitted per steradian but the detection will be done in a smaller solid angle. In the context of the work presented in this thesis, this is the only case of detection in TEY mode. In all the practical cases the XAFM tip works as a detector collecting particles (electrons or photons) in an solid angle smaller than 4π sr.

The beam used in the experiment above had about 10^{10} photons/s. We have seen that only absorption in the first 30 nm contribute to the measured signal.

Thus,

$$I_{30nm} = I_0(1 - e^{-x/\alpha}) \tag{4.5}$$

or,

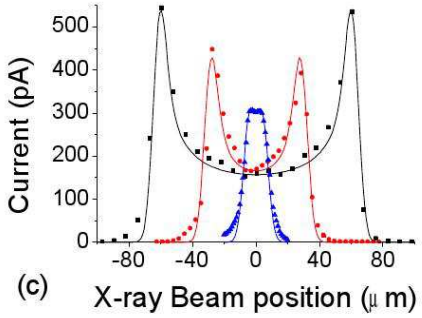

Figure 4.7: Experimental tip photoemission images cross section and theoretical fit. These are in fact horizontal cross sections of figure 4.5. There is one adjustable parameter d_{eff}.

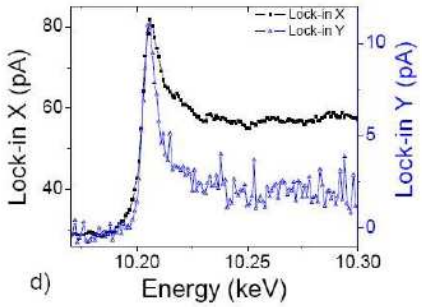

Figure 4.8: L_3 edge of tungsten from the tip measured in TEY mode.The two outputs from the double phase lock in (X and Y) are shown.

$$\alpha = -\frac{x}{\log(1 - \frac{I_{30nm}}{I_0})} \tag{4.6}$$

if we assume the number of absorbed photons is given by the current measured, then before the edge one finds:

$$I_{30nm} = \frac{30 \times 10^{-12}}{1.602 \times 10^{-19}} = 2.5 \times 10^8 \ photons/s \tag{4.7}$$

and after the edge about $5 \times 10^8 photons/s$.
Taking this simple estimation this results in an absorption length of $2\mu m$ before the edge and $4\mu m$ after.
In reality the changes in the absorption length across the edge are larger than by a factor two: before the edge $5.8\mu m$ and after the edge $2.5\mu m$. The discrepancy is mainly due to two factors:

- the effective escape depth of 30 nm is assumed to be the same before and after the edge
- before the edge the photoelectrons are the most energetic particles whereas after the edge electrons of the Auger decay are the most energetic particles.

To carefully measure the changes in the absorption edge one should consider different effective escape depths for different electrons. This should also include a correction due to the different Auger yields, which are first due to absorption by the M shell electrons and after due to absorption by the L shell electrons.

Low energy photoelectrons

We discuss in the next few lines what seems to be a contribution from the slower electrons. Since a careful look into the lock-in signal leads to this discussion.

The lock-in measures only the component of the signal which has its own specific frequency (within a certain small bandwidth). This signal may have a phase lag. The total signal is given by $R\sin(\omega t+\phi) = X\sin\omega t + Y\cos\omega t$, the rms is then given by $R = (X^2+Y^2)^{0.5}$. X is the in-phase contribution while Y is out of phase by $\pi/2$. The absorption and emission processes happen in a time scale ($< ns$) much smaller than $1/\omega$ ($\approx 100\mu s$), thus the signal is expected to be in phase or to lag by π depending whether electrons are emitted from the tip or into the tip. In figure 4.5d as we scan across the L_3 edge of tungsten, the edge jump is seen both in the X and Y lock-in signals.

Y has a value close to zero along all the scan except at the white line (the peak). Thus some other physical process must be involved.

A tentative explanation might be that this is caused by the low energy electrons that are just above the Fermi level and cannot cross the barrier into vacuum. This is further discussed below in *What about the lock-in phase*.

4.3.2 Imaging with the XAFM tip

Since the tip can collect photons and photoelectrons from the sample, it can be used as a camera, as the beam scans a given region close to the tip. An example is shown in figure 4.9, where we can see the tip a rolled up tube (right) and a trench or cut in the surface.

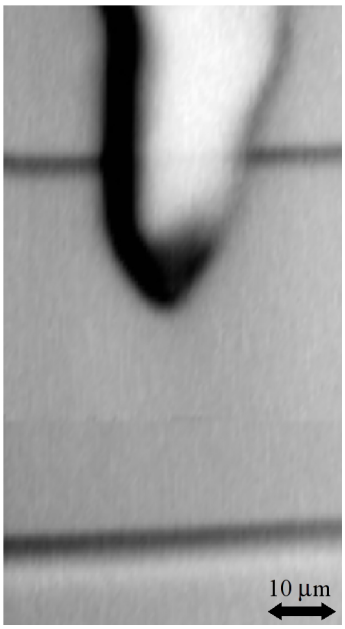

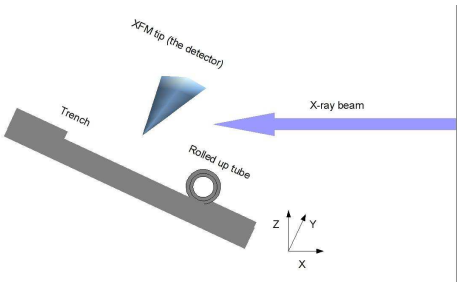

Figure 4.9: (left) Photocurrent from and into the tip. The beam scans a region close to the tip. When the tip is illuminated there is emission directly from it. When the X-ray beam illuminates the sample the tip collects mainly sample emitted photoelectrons. (right) Scheme of the set up.

The image is of course a projection on the YZ plane as illustrated in figure 4.9. This fact simplifies the alignment since it allows simultaneous alignment of the beam, the tip and the sample.

For alignment purposes, the photo-emission from the tip is a useful help. However, it is sometimes hard to tell where the tip apex is in the vertical axis, with a precision better than the X-ray beam vertical width. This difficulty depends on the tip geometry, our prior knowledge of that geometry (SEM images) and on the X-ray beam intensity. Depending on the experiment goals this may or not be an issue of concern.

Currently, work is being done to solve this problem. This difficulty will possibly be overcome trough the use of what we call *smart tips*. This is discussed more in detail in a section below.

4.4 Combining AFM with XAS

In this section we will give some examples of XAS combined with AFM. The limitations will be discussed.

4.4.1 Estimation of the limits

Let us suppose a small particle with photons incident on it. For example a gold sphere of radius $r = 50nm$. The attenuation length α is 7 μm before and 3 μm after the L_3 edge. The number of photons per second absorbed by such particle is approximately given by

$$I_{abs} = I\frac{a}{A}\frac{r}{\alpha}(photons/s) \tag{4.8}$$

If the photons are focused in a 1μm the ratio of particle surface to X-ray beam surface is $a/A = 0.01$. Let it be $I = 10^{12}$ photons/s. Let us also assume the particle is small enough for all the photoelectrons to escape and that each absorption even results in one electron out.

Then the current is,

$$i = 70 \times 10^6(e/s) = 11pA\ before\ the\ edge \tag{4.9}$$

and

$$i = 167 \times 10^6(e/s) = 26.7pA\ after\ the\ edge \tag{4.10}$$

If the tip is scanning the sample in the near field and is able to collect photoelectrons from a region similar to the tip apex radius (i.e a *smart tip* is used), then about 1/10 of the total current is measured. This corresponds to currents larger than the pA.

Using a lock-in technique as mentioned before, currents of the order of a 1pA are easy to measure. Hence, one should in principle be able to detect the absorption edge of a 50nm gold particle.

Moreover, synchrotrons are today making tremendous efforts to reduce beam size. If this reduction leads to higher flux densities than one should be able to push down the particle size and still measure XAS with the XAFM tip.

The goal is to select an individual particle or a specific region of the sample to be studied and measure XAS with the tip.

In the ideal case the lateral resolution would be given by the apex of the tip. In reality, thus far, the whole surface of the tip collects charges and photons. To have a lateral resolution of perhaps 20nm we must isolate the tip and leave

only a small free apex. These tips are somewhat difficult to manufacture and thus, have unfortunately not yet been implemented in the present experiments.

4.4.2 AFM and XAS from Germanium

A substrate of Si, on which epitaxial SiGe was grown, was used as a test sample for combination of AFM topographical imaging with possibly a simultaneous chemical contrast between the Si substrate and the SiGe islands. The islands are 86% Si and 14% Ge. An in-situ topography is shown on the right of figure 4.10.

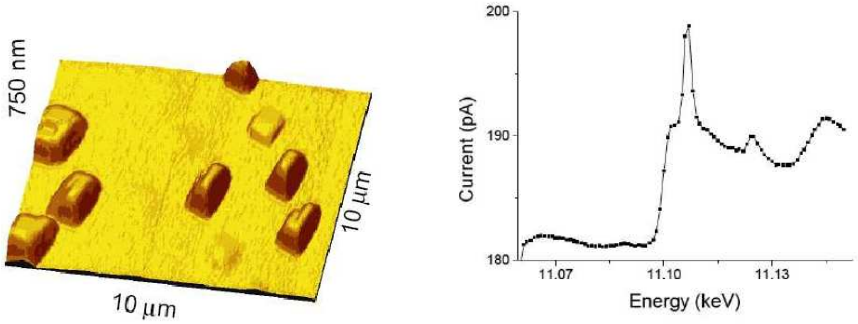

Figure 4.10: (left) In-situ AFM image; (right) measurement across the Ge edge

When the AFM image shown in figure 4.10 was taken, we were expecting to measure a contrast in the current as the tip goes through the isolated islands. The fact that this contrast could not be seen, (thus is not shown) tells us that with the present bare tips, the lateral resolution is dominated by the footprint of the beam. In our particular case the beam illuminated 8 to 12 of these islands.

Despite this, we have XAS data and we could very well measure the Ge K-edge shown on the right of figure 4.10. From the data we could conclude that the Ge islands were quite oxidized. This is indicated by the presence of a shoulder before the white line [73] This is an important piece of information that could not be obtained with the AFM alone. We note that the absorption edge shape is very similar to that obtained with more conventional techniques. Moreover, only about 14% of the islands volume is Ge.

On the other hand, if XAS had been taken in a conventional form, the topography of the illuminated sample would not have been revealed. Nowadays synchrotrons are pushing toward *nano beams*. It will be very hard to tell which part of the sample is being investigated. The techniques described here may have an important role in future nanobeam setups.

4.4.3 X-AFM on gold clusters

Experimental results and discussion

In this chapter we show results that are not completely understood, but can be a starting point for discussion. In one of the tests we made, two gold samples

were used. A first one consisting of a 20nm height gold film deposited on Si and a second one was a sample composed of clusters with 55 atoms (Au_{55}) deposited on a TiO crystal. The clusters are spaced few tens of nm.

The thin film sample, was used to verify the experimental set up by measuring XAS from the gold film. The photoemitted electrons from the film are collected with the tip in TEY mode as shown in figure 4.11. The same type of measurement was taken from the sample containing the Au clusters.

The absorption edge obtained from the Au film is shown in figure 4.11.

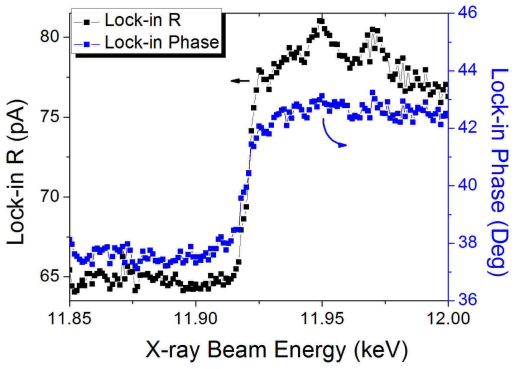

Figure 4.11: Au L_3 edge measured with the tip in TEY mode. The experimental setup for this measurement is illustrated in figure 4.3.

The shape of the absorption edge is very similar to that obtained using the more conventional transmission mode. The data shown is raw data. Each data point took $1s$ to be obtained and there is no average or accumulation since the signal comes directly from the output of the lock-in amplifier, which is synchronized with the chopper as explained above. One should note that there is no obvious reason to see the edge in the phase of the lock-in. However, a phase change of few degrees is clearly visible.

The sample is replaced by the one with the Au_{55} clusters.

In figure 4.12 it can be seen a scan as the X-AFM is moved upwards. The X-ray beam is initially illuminating the tip and the X-AFM is moving such to move the X-ray beam to the sample.

Such scan has already been shown for a different sample in figure 4.4. The type of scan is exactly the same, but here there is a sudden increase in phase when the X-ray beam is just below the tip. Furthermore this corresponds to a slightly sudden change in the amplitude.

What about the lock-in phase?

Since the absorption and emission processes happen at time scales much smaller than the period of the chopper wheel, the measured current is expected to be either in phase or out of phase by 180Deg with the chopper which itself has its own phase relative to the lock-in amplifier. Hence, at all times one expects to measure $\phi_{electron}$ or $\phi_{photons}$ which are respectively the phases when the signal is due to collection of electrons or photons, such that the equality between the three following constants holds:

$$\phi_electron = \phi_{photons} - \pi + \phi_{ref} \tag{4.11}$$

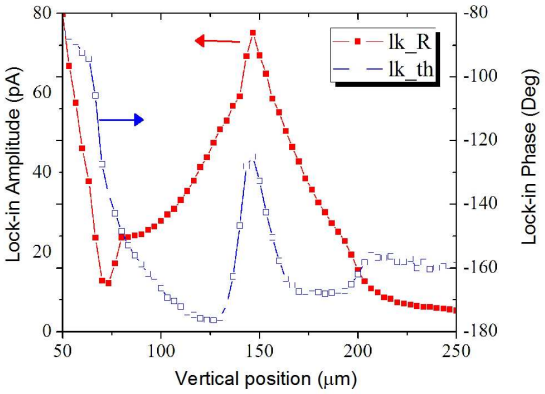

Figure 4.12: The X-ray beam is initially illuminating the tip and the X-AFM moves upward, as we go from left to right in the plot, toward a situation of X-ray beam on the sample.

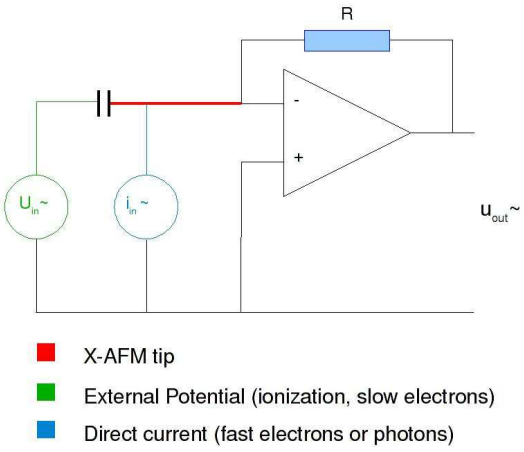

Figure 4.13: Proposed scheme to explain the additional phase change. Two channels contribute for the measured signal. Photons or fast electrons penetrate the tip barrier and generate a direct current either in phase or completely out of phase. Ionization and slower electrons result in a potential difference between the tip and the tip exterior across the capacitor.

However, in the two previous plots one finds a situation where:

$$\phi_e lectron \neq \phi_{photons} - \pi + \phi_{ref} \tag{4.12}$$

Hence we are led to conclude that there is a mechanism introducing some time constant.

Since it is necessary a certain amount of energy for electrons to escape the tip, we believe that the additional phase change is related to the amount of charge that cannot escape the tip surface. This can be pictured by means of a capacitor and an external potential as shown in the scheme of figure 4.13.

The resulting output signal is given by:

$$u_{out} = -R(2\pi j f u_{in} c + i_{in}) \tag{4.13}$$

Where u_{out} is a potential due to the charge across the capacitance C. R is the gain of the transimpedance preamp, i_{in} is a current directly induced by the photoemission, and f is the frequency of the chopper. We have assumed a chopper frequency of 1kHz, a direct current of 1nA and calculated as a function of the capacitance C and potential difference u_{in} the expected change in the absolute signal and in phase. The capacitance is chosen between 0 and 1pF and

the potential across the tip surface between -1V and 1V. The result is shown in figure 4.14.

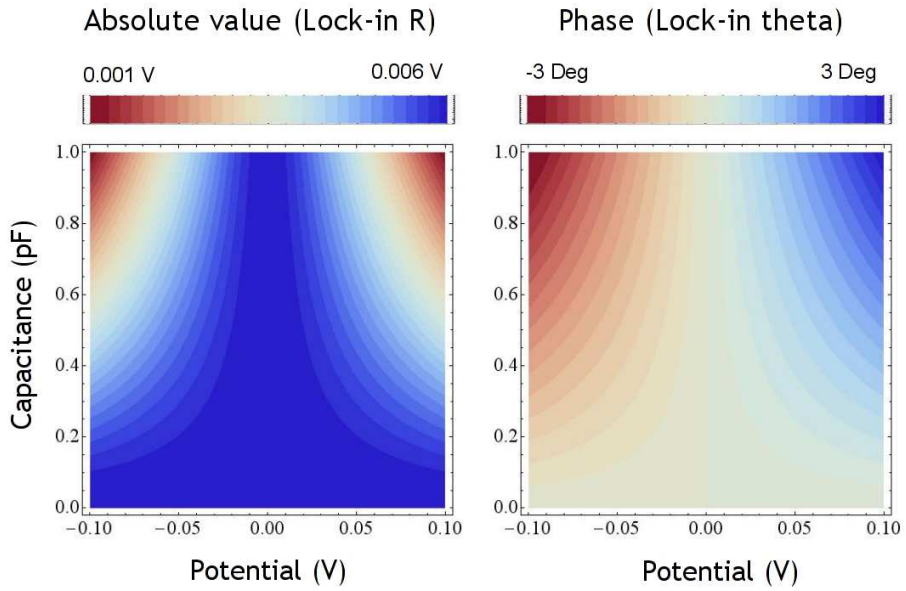

Figure 4.14: (left) Lock-in phase; the phase is zero in the absence of potential difference or for zero capacitance. (right) The measured signal is constant and proportional to the direct current in the absence of potential difference or for a zero capacitance.

For a potential difference of 0.5V and a capacitance 0.1PF the difference in the amplitude is of 5%. and a phase change of 17Deg is expected, and so, it is more visible in the phase than in the amplitude.

This is rather a qualitative description, unfortunately we do not have enough experimental data to validate this hypothesis.

Finally, the two lock-in outputs, the amplitude (left) and phase (right), from the clusters' sample are shown. Both are compared to the reference spectra. The reference spectrum, is an average of ten curves similar to those shown in figure 4.11.

Most of the illuminated surface is not gold, moreover given the size of the clusters, very little absorption is due to the Au_{55}. It is not possible to identify the Au L_3 edge in the absolute measured signal. However, the phase seems to show some peaks near the edge position. The highest peak has a phase difference of more than 20Deg. The same behaviour was observed repeatedly, thus it is not likely to be noise.

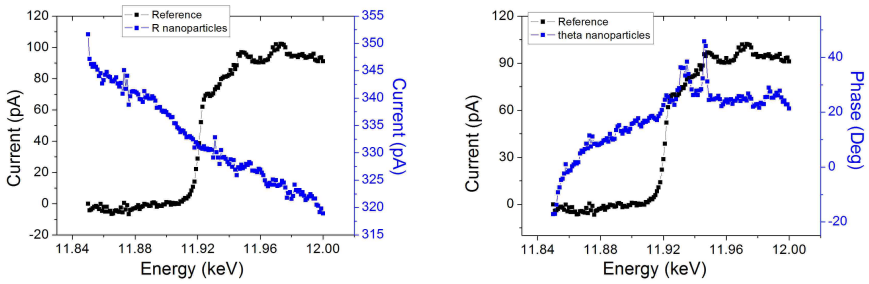

Figure 4.15: (left) Current detected from the Au clusters (blue) superposed on the reference spectrum previously measured (black); (right) Phase of the lock in (blue) superposed on the reference spectrum. It is visible the edge as well as what can be XAS oscillations.

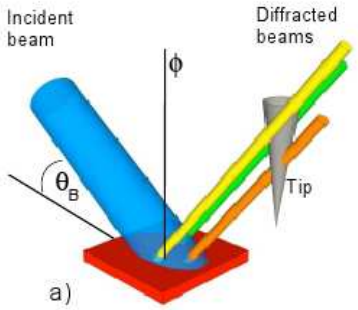

Figure 4.16: Illustration of how the tip can be used to locally measure diffraction data. In the representation, three particles diffract the incoming X-ray beam.

4.5 Combining atomic force microscopy with diffraction

Bragg reflections can be measured through collection of photons with the tip. The diffracted photons will impinge on the tungsten tip and produce photoelectric effect similar to when the tip is directly illuminated with the X-ray beam.

To show this we have performed rocking curves whilst using the tip as the photodetector.

Here again, the detector is a tip which in total occupies a large volume in space. The whole tip is then the detector. Thus the angular resolution of the detection is given by the angular distribution of the incoming beam.

The idea is illustrated in the figure below (fig. 4.16).

4.5.1 AFM and Diffraction from Ge islands

The tip was parked few μm above the sample. The beamline diffractometer was then set to scan the angle of incidence around the theoretical Bragg condition. The theoretical Bragg condition for the Ge (3 1 1) at an energy around the Ge K edge is about 12 Deg.

The current picked up by the X-AFM tip is shown in figure 4.17 for different azimuthal ϕ.

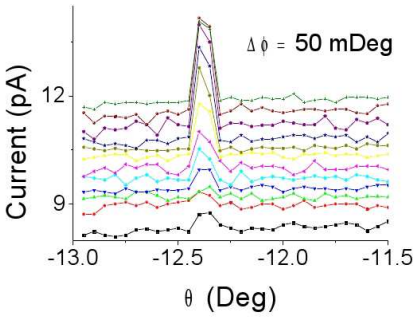

Figure 4.17: photocurrent from the W tip as a function of the incidence angle θ, and azimuthal ϕ.

The diffraction is usually measured with a 2θ detector. This detector is located about one meter after the sample and collects photons in a very small solid angle. This may be very important to reject unwanted noise or increase resolution. The angular resolution is very high compared with that we may expect if we use the tip to detect the diffracted photons.

The advantage of using the X-AFM as a stand alone detector is that we can tell *what* in the sample is diffracting.

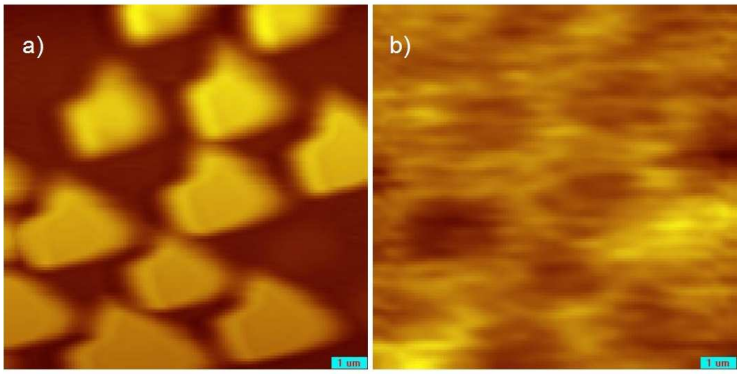

Figure 4.18: (a) AFM image; (b) current. The contrast in the current image in which we see the Ge islands as holes, is because the tip collects the diffracted x-rays which subtracts from the photoelectrons.

A first result can be seen as a contrast in the measured current while taking AFM topography images of the sample when in Bragg conditions, see figure 4.18. No contrast at all when the sample was not in Bragg condition. The AFM image suffers of a great tip effect, due to the fact that the tip was used for quite a while and was blunt. We see the particles as holes, since the photons of the Bragg reflected beams extract electrons from the W tip which causes a decrease in the overall current mainly due to the smooth background of electrons photoemitted from the sample.

DAFS measured with the X-AFM tip

In the course of the previous experiment the same Bragg peak was measured for different energies across the Ge K edge. This allows to measure the anomalous contribution to the diffraction.

Near the absorption edges there is a modification of the scattered intensity due to the absorption processes. The number of photons being diffracted has a sudden decrease due to the sudden increase of the absorption cross section. This gives the opportunity to measure the X-ray Absorption Fine Structure as seen by a particular Bragg reflection. It is often used to disentangle the Absorption Fine Structure contribution from a given atomic species but distributed in different crystal sites.

In fig. 4.19a it is shown the evolution of the Bragg peak as the photon energy is increased.

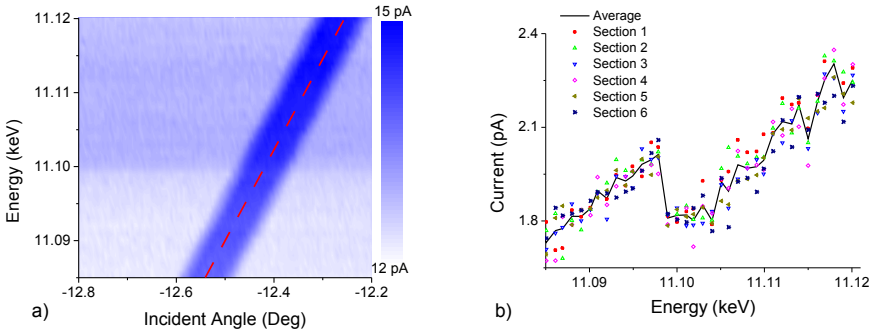

Figure 4.19: (a) Evolution of the Bragg peak intensity as a function of angle and energy; (b) cross sections along the dark stripe in (a), the solid line is the average.

Figure 4.19b shows several cross sections (red line on 4.19a indicates one of them) following the Bragg peak evolution, i.e., the Diffraction Anomalous Fine Structure spectrum. The sections are centred around the middle of the dark stripe on figure 4.19a separated by about 0.01 Deg. This is a preliminary result, but shows that local anomalous diffraction can be measured from a single *nanodot* with the X-AFM tip.

In the present experimental conditions, i.e., without *Smart Tips* the background due to sample photo emission is the major source of noise. In fig. 4.19b this background of about 12 pA has been subtracted. Note that the subtracted background is not constant throughout the image since it also depends on the photon energy.

4.6 Indentation with a tuning fork

4.6.1 Introduction

Thus far, the results shown concern the combination of AFM topographical capabilities with pure X-ray techniques, namely diffraction and absorption spectroscopy.

In this section the X-AFM tip will not be used as a photon or photo electron detector except to align the X-ray beam with the X-AFM tip. Rather the tip, attached to the TF will be used as an indenter. The X-ray setup can then be used in diffraction mode to measure lattice parameter changes.

This kind of experiment will allow studying the elastic behaviour of nano-sized particles as it offers the means to locally access their Young moduli, as explained below. It will also allow studying how the size of the particles influence the germination and propagation of defects and the role of dopant as a means to favour these defects or their propagation [78, 79]. Investigation of how transformations into other phases affect the Young modulus as the pressure is increased should also be at hand.

Interest in such experiments is obvious, due to the on going miniaturization of electric and mechanical components. It turned up that new physical properties appear as dimensions are reduced below few tenths of nanometres [80, 81]. The size of the particles is also expected to affect their plasticity [82, 83]. As a consequence measurement of these new properties has become of increasing importance.

If on the one hand the study of semiconductor nano-structures, strained during coherent growth on substrates, has been extensively investigated using synchrotron light [74] on the other hand nano-indentation experiments have been performed using mostly Berkovich indenters [75] though some were performed with AFMs [76, 77].

Experiments were performed in four different samples:

- copper crystal
- rolled up nanotubes
- Au clusters randomly orientated in a sample
- epitaxial grown SiGe islands on Si

The idea was to measure a change in the diffraction pattern whilst the tungsten tip interacts with the sample.

Such change in the diffraction pattern was observed for the first and fourth samples. However, in the first case interpretation of the data was complicated by the difficulty to separate the contribution from the bending of the sample under the tip from the indentation. However, it is perhaps worth mentioning that the TF was successfully used to indent the soft copper surface, as shown in figure 4.20.

The tip was very successful at breaking the rolled up nano-tube as well (see fig. 4.21).

This happened because as soon as the tip pushed on the nano-tube the Bragg condition was lost and to get back this condition the incidence angle had to be

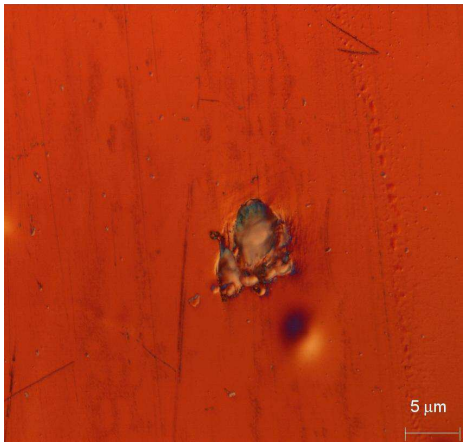

Figure 4.20: Photograph of the copper crystal surface. Visible is the indent left by the tungsten tip. The tip used had been previously blunted to have an apex radius of few μm.
Courtesy of Marc de Verdier.

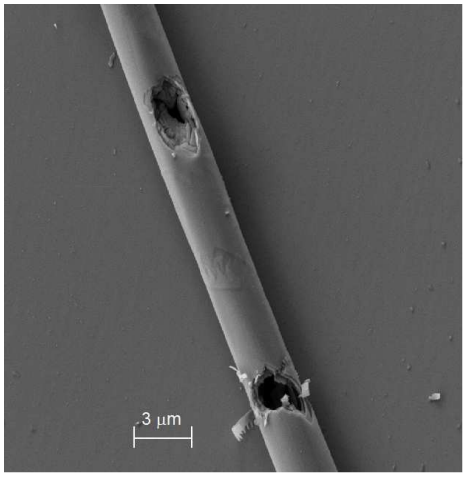

Figure 4.21: SEM image of an indented/destroyed rolled up nanotube. Courtesy of A. Malachias.

changed. This was done while the tip was close to the tube and because of motor vibrations led to its destruction.

Concerning the experiments in Au clusters we have never been able to get the diffraction from the clusters just below the tip or alternatively we have never been able to put the tip above the diffracting particle. This nano crystals were formed after heating of a Au film deposited in a Si substrate. The resulting crystals have all possible orientation and the Bragg condition is not met simultaneously for all of them as for epitaxial islands. Thus it is not possible to correlate a diffraction map with an AFM image. The experiment could be done if the alignment of the beam with the tip apex was better than few μm. However, in the vertical direction there is an alignment error that can be of ten or more μm. It becomes then difficult to say which of the clusters is diffracting if there are crystals every two or three μm. A *smart tip* would have a very important role in this context.

In what follow we will discuss more in detail the methods used and focus on the sample with the epitaxial SiGe islands.

4.6.2 Indentation of SiGe islands

The sample was constituted a Si substrate on which SiGe [74] islands were grown by Liquid Phase Epitaxy (LPE) in the Stranski-Krastanov growth mode [72].

The shape of the islands, as can be seen form the in-situ AFM image 4.22(a), is a truncated pyramid with a base length of about 1000 nm, a height of 500 - 700nm. The average Ge concentration is of 14%.

The idea is to apply a certain amount of pressure, if possible a known pressure, and measure the change in lattice parameter with the X-ray beam.

The W conductive tip is used: first, to obtain the AFM image; second, the coordinates of the X-ray beam via the consequent photoelectric current after illumination of the tip and finally to indent.

Mapping this current yields a photoelectric image of the tip which allows to align the tip with the X-ray beam and with the Ge islands. Fig. 4.22 shows one of these maps superposed to a diffraction map, i.e., after the crystallographic alignment of the Ge particles and of the tip with the X-ray beam, the AFM position is scanned resulting in simultaneous imaging of the tip (photo current) and of the islands (diffracted photons). The beam footprint was of approximately 3x1.5 $(\mu m)^2$.

After all the alignments the tip is positioned on top of one single SiGe island. A certain time is waited to avoid any drifts, then the X-AFM feedback loop is turned off and an additional voltage is applied to the Z-piezo of the AFM causing the sample to move up against the tip. For every value of load two TF resonance curves should be taken. However, in the experiment discussed here only one resonance curve was taken. This resonance corresponds to the TF mode oscillating perpendicular to the sample.

From the resonance frequency shift the contact stiffness can be deduced [84]. At each point a diffraction map is obtained with a CCD camera in $\approx 20s$. The sample is then moved up again and the process repeated. Then, for each load a resonance frequency 4.23 and a diffraction 4.24 map are recorded. From the diffraction map we deduce the lattice parameter change [14].

The resonance curves taken are shown in figure 4.23.

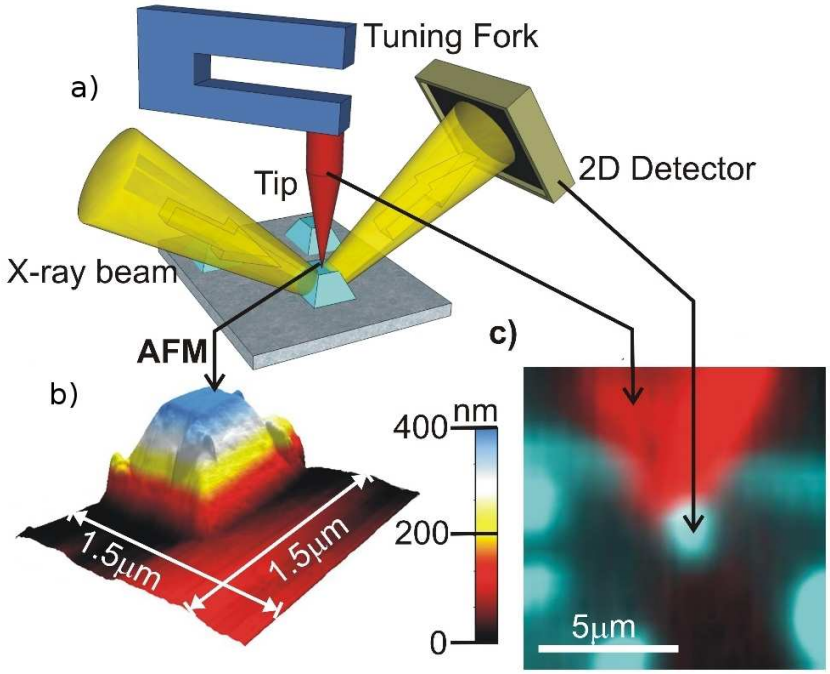

Figure 4.22: a) Experimental set up; b) Topography of the illuminated particle and (c) tip map superposed to the diffraction map. Not visible in the set up is a chopper used to chop the beam at the frequency of the Lock-in, at about 1 kHz.

The TF resonance frequency shifted from about 29 kHz, corresponding to the non interacting resonance frequency to about 50 kHz corresponding to the highest applied load. On covering the interval from 29kHz to 50kHz, other mechanical modes of the complete system couple to the TF mode. An example of this is shown in figure 4.23 in the peak labeled spurious peak. The frequency of this peak is independent of the load. Coupling with such spurious peaks leads to changes in the height of the resonance curve and makes it difficult to tell which was the amplitude of oscillation of the TF for each load. The curves shown in figure 4.23 are normalized to an amplitude of 1. The TF excitation was kept constant. Thus, amplitudes of vibration comparable to those measured prior to the indentation are expected. This corresponds to about 2nm.

Clearly for better and more consistent results one needs to work out a solution to uncouple the TF resonances from the overall mechanical setup.

The 3D diffraction pattern close to the (004) reflection is used to follow the response of the island while being stressed. The forces applied by the X-AFM tip induce a compression of the lattice parameter of the SiGe island perpendicular to the surface and thus a shift of the diffuse scattering from the island toward the (004) Si position occurs. Six of the diffraction patterns are shown in figure 4.24. The first corresponds to the unstrained SiGe island. The subsequent diffraction patterns from II to VI correspond to increasing load. Note that the Bragg peak cannot be followed since this requires changing the incidence angle.

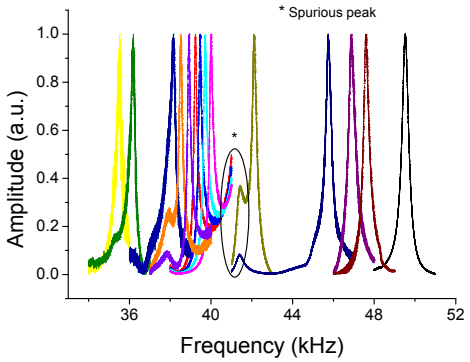

Figure 4.23: Resonance curves of the TF for different applied pressures. Higher resonance frequencies correspond higher pressures.

This cannot be done while the X-AFM tip is in contact. One could try to change the energy of the incoming beam, thus its wavelength, to follow the Bragg peak. However, this is difficult because it changes the X-ray beam position and focal characteristics.

When the X-AFM tip is retracted, the scattering signal, in this cases, follows back to the original position. This indicates that the deformation takes place within the elastic regime. This has been confirmed with X-AFM and SEM images after the experiment. The island seems perfectly untouched. In another island, deformation went on up to the fracture point.

In figure 4.25 can be seen the evolution of the resonance curves and of the lattice parameter change as a function of the distance traveled with the X-AFM piezoelectric scanner.

The lattice parameter was extracted from the position of the centre of mass of the SiGe diffraction pattern.

4.6.3 Indentation analysis

The estimations reported in this section intends to give an overview of what can be experimentally measured, in particular how can the Young modulus be obtained from experiments similar to the one previously described.

The contact stiffness S depends both on the effective Young modulus $E*$ and contact area σ [84, 85] since,

$$S = 2E_r\sqrt{\frac{\sigma}{\pi}} \tag{4.14}$$

where E_r is given by

$$\frac{1}{E_r} = \frac{1-\nu_{tip}^2}{E_{tip}} + \frac{1-\nu_{sample}^2}{E_{sample}} \tag{4.15}$$

where E and ν are respectively the Young modulus and Poison's ratio for the tip and the sample. and is obtained with the TF since its resonance frequency is given by (see second chapter):

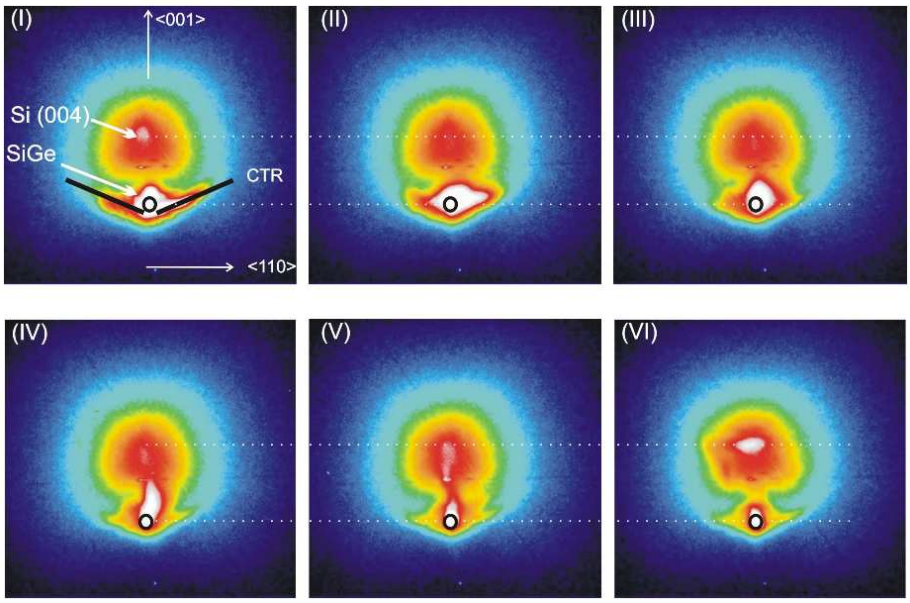

Figure 4.24: X-ray diffraction maps for 6 consecutive pressures applied on an individual SiGe island. We identify the origin of each individual signal, e.g., the island facet crystal truncation rod (white arrows), the SiGe Bragg peak itself (SiGe), the Si substrate (Si(004)) as well as the substrate crystallographic directions. The black circle denotes the substrate CTR. Note, that it does not change its position or shape, indicating that no surface tilt occurred while applying a pressure.

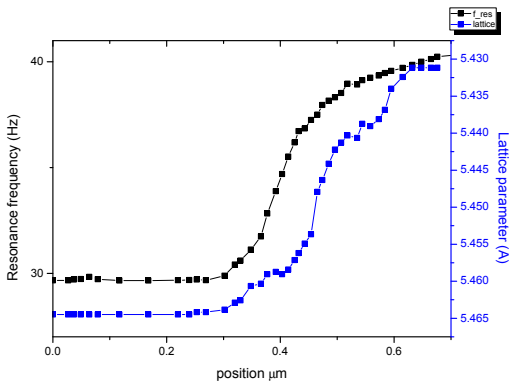

Figure 4.25: Resonance frequency shift and mean lattice parameter change plotted as a function of the traveled distance toward higher indentation depths.

$$f = \frac{1}{2\pi}\sqrt{\frac{k_{eff}+S}{m_{eff}}}. \tag{4.16}$$

Because the indentation depth h was much smaller than the tip radius R ($h \approx 5nm$; $R \approx 2\mu m$) the following approximation can be done:

$$h \approx \frac{r^2}{2R} \tag{4.17}$$

The approximation above can be understood by looking at figure 4.26. It means that at the point of contact the surface has the profile of the tip, a sphere-like surface; r is the radius of a circumference which cuts through the sphere at height h.

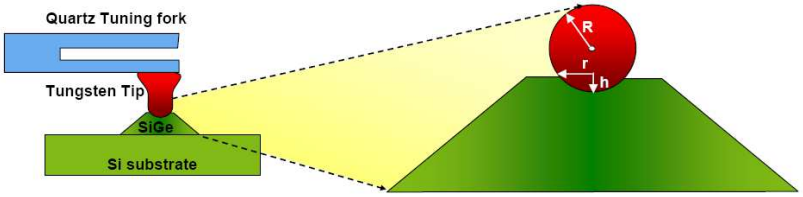

Figure 4.26: Scheme of the indentation. A sphere like profile is assumed to be a good approximation of the indentation profile.

The diffraction pattern measures the average lattice parameter a_{mean} of the island. This value must be related to the indentation h, i.e., it must be found the function $a_{mean}(h)$. For this particular geometry this is straightforward: below the tip the surface has the profile of the tip, thus $a_{mean} \approx (h/2)\times(a_0/H)$, where $(h/2)$ is approximately the mean indentation depth (found by integration) and H is the total height of the particle. In the region where there is no indentation $a_{mean} = a_0$. It is assumed that the volume is divided in two regions: a stress free region around the indentation and a uniform strained region underneath the tip.

Therefore the total a_{mean} is given by:

$$a_{mean} \approx \frac{(A-\pi r^2)a_0 + \pi r^2(a_0 - \frac{a_0 h}{2H})}{A} \tag{4.18}$$

where A is the surface of the top of the island. This combined with equation 4.17 gives:

$$a_{mean} = a_0 - \frac{a_0 \pi r^4}{4RAH} \tag{4.19}$$

The contact radius r is given by $r = \sqrt{\sigma/\pi}$. Thus $r = S/(2E_r)$ (equation 4.14). The final expression relating diffraction data with stiffness data (resonance frequency shifts) is:

$$a_{mean} = a_0 - \frac{a_0 \pi}{64RAHE^{*4}} S^4 \tag{4.20}$$

A and H are known from the in-situ X-AFM images, R is estimated from SEM images of the tip.

The top surface is: $A = 1.66 \times 10^{-13} m^2$; the height: $H = 590nm$; and the tip radius: $R = 2.4\mu m$.

The relationship expressed in equation 4.20 is seen in figure 4.27 together with the experimental data. The Young modulus was found by a linear regression.

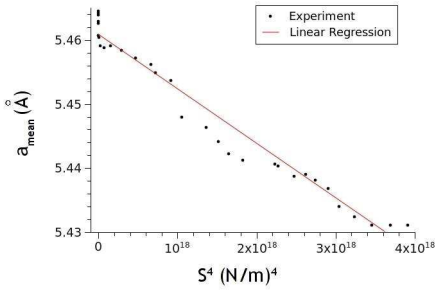

Figure 4.27: Mean lattice parameter change as a function of the resonance frequency shifts to the power of four. A linear relationship is expected from the relations explained in the text above. A linear fit to the data yields the reduced Young modulus of the tip+island. Except the Young modulus all constants are known

The value of E_r which better fitted the data was $E_r = 108.3GPa$. This value can be compared to the expected Young modulus for bulk $Si_{86}Ge_{14}$. Using Vegard's law [86] and considering Young moduli of 130 GPa and 103 GPa for Si and Ge respectively, the Young modulus of the island is $E_{island} = 126GPa$ and $\nu_{island} = 0.278$ [87]. For the tip is $E_{tip} = 405GPa$ and $\nu_{tip} = 0.3$. Using this constants a reduced elastic modulus of 105 GPa is obtained. Thus the experimentally obtained E_r of 108 GPa is in accordance with the one calculated for bulk material. Size effects in the elastic regime are not expected to occur on these length scales but for objects of a few tens of nanometres in size.

The involved forces in these experiments can be calculated by integration: $dF = Sdh$. Combining equation 4.17 with equation 4.20, putting $\xi = (a_0 - a_{mean})$ and defining b such that b/E^4 is the slope in equation 4.20 gives:

$$h = \frac{1}{8RE^{*2}}\sqrt{\frac{\xi}{b}} \quad and \quad \frac{dh}{d\xi} = \frac{1}{16RE^{*2}}\sqrt{\frac{1}{b\xi}} \tag{4.21}$$

$S(\xi)$ can be obtained from equation 4.20.

$$S(\xi) = \left(\frac{\xi}{b}\right)^{1/4} \tag{4.22}$$

Thus we have after integration ($\int Sd\xi dh/d\xi$):

$$F(\xi) = \frac{1}{12RE^{*2}}\left(\frac{\xi}{b}\right)^{3/4} \tag{4.23}$$

It is worth noting that calculating $F(h)$ using equations 4.14 and 4.17 or instead replacing h given by equation 4.21 in equation 4.23, results in a power law with exponent 1.5:

$$F(h) = \frac{4}{3}\sqrt{2R}E_r h^{1.5} \tag{4.24}$$

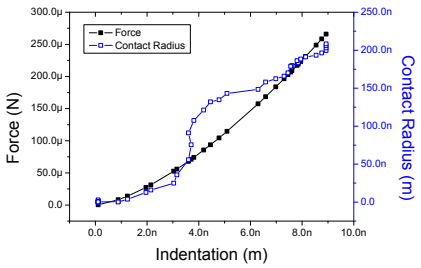

Figure 4.28: Calculated indentation, load and contact radius relations.

as expected when indentation is made with a paraboloid [84].

At the point of maximum load the force (equation 4.23) was $F = 267\mu N$. The contact radius (equation 4.14) was $r = 200nm$. Then the average pressure at maximum load was $P = 2.12GPa$.

In figure 4.28 it is shown the evolution of the load F and of the contact radius r as a function of the calculated indentation h.

4.7 *Smart tips*

4.7.1 Introduction

Since the very beginning of the project it was thought that a special tip was needed for better exploit the combination of AFM with synchrotron light spectroscopies. The initial need for a special tip was mainly to localize the detection in TEY mode to a small region below the tip apex. It turned out that a tip with special characteristics is needed for even more fundamental reasons related to the issue of aligning the tip with the X-ray beam. A good alignment between X-ray beam ant the X-AFM tip is always required. With the present tips the alignment in the direction perpendicular to both the tip and the beam is straight forward, however the vertical alignment is quite difficult and there is no real way to tell if the alignment has been successful or not.

The initial idea of a smart tip is illustrated in figure 4.29.

Such type of tip would also ease the alignment with the X-ray beam. The light absorbed at the tip core produce electrons that cannot escape through the gold coated insulating layer shielding it. This leads to significant currents from the shield and small ones from the core, as long as the beam is far from the tip apex. The situation is reversed when the beam illuminates the tip apex. The open part would be 20nm to 100nm long.

Unfortunately such tips were never tested on a beam line.

4.7.2 Simply insulated tips - strategies

Experience has shown that a tip that would simply ease the alignment is extremely important for this purpose. A tungsten insulated tip bare just at its apex should be enough simplifying the manufacturing of tips following the *smart*

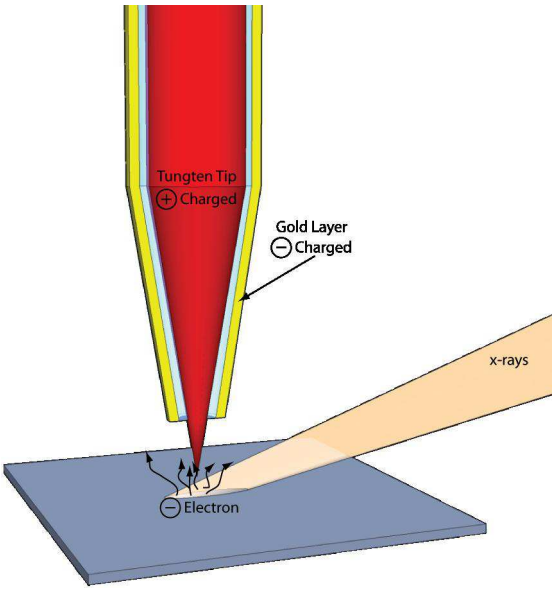

Figure 4.29: Illustration of the smart tip principle. A tungsten tip is insulated and subsequently shielded with a metallic material, such as gold, living only a small aperture at the tip's apex. The inner part of the tip is positively charged attracting the emitted photoelectrons while the outer part in negatively charged repealing the electrons.

tip concept. In this simple case if the beam does not illuminates the tip apex then, in the best case, no current whatsoever is measured since the created electrons cannot escape the insulator to reach the vacuum. Of course the thickness of the insulator must be larger than the electrons effective escape depth. For energies from 10 to 20 keV this is always of few tens of nm. If the beam illuminates the free apex than a current of few pA should be measured.

In practice if a small current is detected when the beam is still far from the apex is helpful since it helps to track the apex. If the insulating layer is made of a fluorescent material then the task of finding the tip is even easier. Then the tip position can easily be found with the fluorescence, while its apex would be found by detecting the increase in current when the X-ray beam is shining on it.

This simplified version of a *smart tip* should be able to localize TEY measurements in a way similar to that of the scheme in figure 4.29, since the electrons traveling in the direction of the insulator layer would not be able to reach the *smart tip* core. In a simply insulated tip, however, the potential of the outer shell is not controlled and parasitic localized charges may lead to funny effects difficult to control.

Three different versions of this *smart tips* have been prepared, two of which have been partially tested.

Parylene insulated tips

A tungsten tip is glued on a TF following the procedure described in chapter three. The whole system TF+tip is then isolated with parylene C. The thickness of the deposited parylene was of about 300nm. The coated tip is then brought close to a conducting surface within few nm. A sudden electric potential is then applied exploding the tip apex. Well controlling the distance and the applied potential lead to beautiful tips as the one shown in figure 4.30.

One of these tips was tested. The signal from the tip was always intense,

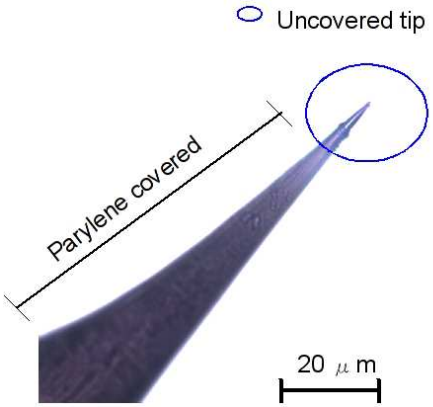

Figure 4.30: A tungsten tip covered with parylene with an open end. The end was open by electrostatically exploding the part of parylene covering the apex.

perhaps smaller than what would be obtained with an uncoated one. Either a larger amount of parylene should be used or a different material should be chosen. Unfortunately the time dedicated for testing this tips was very reduced.

Tips opened with Focused Ion Beam

Another way of opening the tips was trough the use of Focused Ion Beam (FIB). Different materials were used to coat the tungsten tips: Al_2O_3, Parylene and SiO_2. Different thickness have been used: 30nm; 200nm. From the SEM images of these tips, considering the energy of the electrons used to obtain the SEM images, it is easy to guess that neither the parylene nor the SiO_2 coatings will work. The SEM images for these two coatings are very clear indicating the coatings are transparent to the electrons. Moreover, as mentioned before, parylene coated tips have been tested and did not work successfully.

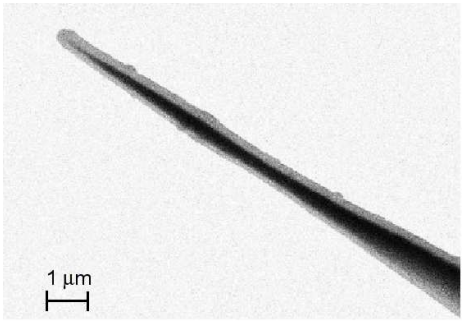

Figure 4.31: SEM image of a tungsten tip covered with SiO_2. The tip apex is to be opened with a FIB. The clarity of the image let us guess that these tips cannot be used as *smart tips*.

On the other hand tips covered with Al_2O_3 were systematically difficult to image in SEM due to accumulation of charges. We believe this type of coating might be more appropriate for the design of *smart tips*. However, thus far these tips have not been tested with X-rays. A SEM picture of Al_2O_3 coated tips is shown in figure 4.32.

Coating with an optical adhesive

Another method used to obtain *smart tips* was based on the use of a glue that cures with UV light. The idea was to cover the whole tip with the hope that

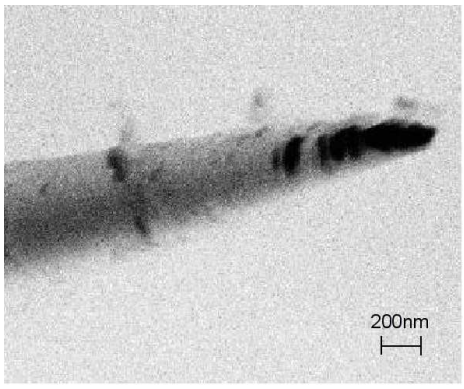

Figure 4.32: SEM image of a tungsten tip coverd with Al_2O_3. The tip apex has been opened with a FIB. It is rather difficult to tell whether the opening of the apex has been successful or not.

during the UV curing the glue would slightly shrink living an open apex. The tip is immersed in the initially liquid UV glue and then removed. Then after a UV gun is shined on the tip to dry the UV glue. A SEM image of such tip is shown in figure 4.33.

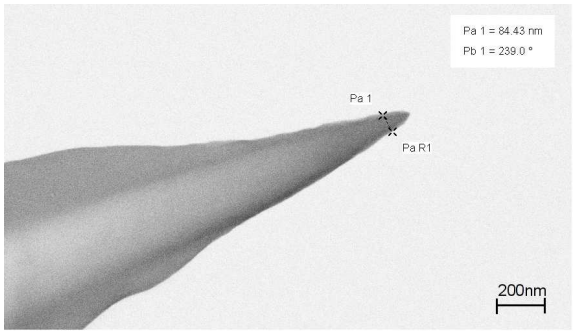

Figure 4.33: SEM image of a tip coated with UV glue.

Some of these tips have actually been tried. However, since the experiment proposal did not included testing the tips, the results obtained were just preliminary.

A photo-current is generated even when the tungsten coated tip is illuminated far from the open apex. However, the signal was about four times smaller than that from an uncoated tip. This can be seen in figure 4.34.
Four of these coated tips were scanned obtaining very similar results. Since far away from the apex the measured photocurrent is higher than that produced when the beam is illuminating the X-AFM tip apex, it becomes difficult to tell whether the apex is opened or not. In other words the z dependence of the signal is the same for a coated and an uncoated one. From the SEM images it was also difficult to tell whether the apex was opened or not.

Perspectives

Even though Al_2O_3 coated tips have not been tested, the SEM images indicate that these tips could be the best suited for being at the basis of a *smart tip*. However, to open them with FIB is both difficult and expensive. If the apex can be removed by explosion, as shown for the parylene coated tips (figure 4.30) then this would be a relatively fast and non expensive way of fabricating *smart*

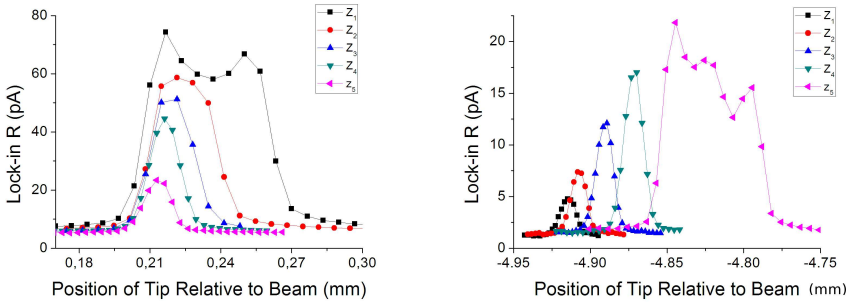

Figure 4.34: Left - Current detected from the uncoated tip; Right - Current detected from the coated tip.

tips.

4.8 Conclusions

In this chapter, after a brief discussion of the experimental setup, we started by discussing how the alignment of all the different elements can be performed. The rough alignment is easily done since photoelectric effect on the tip leads to a current flow of more than 1nA for beams with 10^12 photons/s. For sharp tips the vertical alignment of the tip apex is somewhat difficult. This is because the current slowly falls down as the X-ray beam is moved vertically away from the tip. In most of the cases, a fine vertical alignment can only be done if the exact tip profile is known from SEM images. Implementation of *smart tips* will facilitate the tip apex alignment tremendously.

Further, it was estimated that only absorption happening at less than 30nm from the surface contributes to the final signal.

We saw how the X-AFM tip can also be used to collect sample-emitted photoelectrons.

The signal detection is in most of the cases done using a lock-in amplifier.

The phase lag between the X-ray beam intensity and signal intensity allows to distinguish electrons from photons because there is a phase difference of 180Deg between the two measurements.

We have then showed some results where the tip of the X-AFM was used as a spectroscopy detector. If on one hand to measure the absorption with the X-AFM tip is straight forward on the other hand the lateral resolution is still dominated by the beam footprint.

A successful combination of both techniques where chemical contrast can be obtained simultaneously with the AFM topography can only happen through the use of *smart tips*. Using such tips we estimate to obtain a lateral resolution better than 50nm.

Since the tip can collect either photons as well as photoelectrons, diffraction is also a possibility. The angular resolution can not be compared to that obtained using more conventional and sophisticated methods. However, it is possible to identify what in the sample is diffracting. This may be useful to

align the tip and the X-ray beam in a particular diffracting particle. Here again, *smart tips* can play in important role in reducing the background and enhancing the signal.

The most successful experiment was when X-ray diffraction was combined with indentation. The X-AFM tip was used to elastically and plastically deform (indent) a surface. This was done in a synchrotron beam line, and so, diffraction from the deformed surface was simultaneously measured.

The evolution of the TF resonance frequencies were recorded for each indentation depth as well as the evolution of the diffractions peak. The two information altogether allowed to derive the Young modulus of a SiGe particle. In such derivation there are no adjustable parameters. The particle size was of almost $1\mu m$. Unfortunately no experiment has been performed on smaller particles yet.

As a final remark it seems obvious that the future of such techniques depends on the successful design and implementation of *smart tips*.

Chapter 5

Conclusions and Summary

We will now make a summary of the most important results obtained in this thesis and draw some conclusions.

5.1 Theory of the tuning fork

After introducing the context of this thesis work we have, in the second chapter, tried to address questions concerning the TF. It was found that for the fundamental modes of an individual TF prong the Euler-Bernoulli beam approximation is sufficiently accurate and was used for all practical proposes when considering the fundamental resonance frequency of an individual clamped TF prong.

Furthermore, the fact that the experimental resonance frequencies of a TF are lower than those calculated for an individual prong is not due to a miss calculation because of neglecting rotational inertia or shear motions.

Hence, the resonance frequency of a TF is different than that of its individual prongs.

To account for the lower resonance frequencies of the TF the two prongs were coupled to a common anchoring point.

The stiffness of this common body was adjusted to give resonance frequencies identical to those observed experimentally.

A simplified transfer function that includes interaction of one of the TF prongs with the external world was then obtained. This simplified transfer function of the TF was assumed to be accurate enough for all our purposes.

The resonance frequency of the tuning fork is given by:

$$\omega_i = \sqrt{\frac{k_r + \epsilon k_i}{m_r}} \tag{5.1}$$

with $k_r = 10.4kN/m$ and $m_r = 240\mu g$ the reduced stiffness and mass respectively.
The width of the resonance curve is given by:

$$\frac{\gamma_{ri}}{m_r} = \frac{\gamma_r + \epsilon\gamma_i}{mr} \tag{5.2}$$

with $\gamma_r \approx 5mg/s$, corresponding to a width of few Hz
and

$$\epsilon = \frac{1}{2}\frac{m_2}{m_1 + m_2}. \tag{5.3}$$

It was then discussed the Q factor of the tuning fork.

Here we saw that the main damping mechanism affecting the TF as well as a Si cantilever is air damping.

Though, air damping is about 100 times higher for a Si cantilever due to its smaller dimensions. The symmetry of the TF may or not have an important role depending on the relative impedance of the media to which it is attached.

If the fork is perfectly symmetric then this last aspect never matters, since no velocity is imparted to the other media.

Due to the very small impedance of a Si cantilever this does not usually play a role.

The tuning fork is extremely easy to excite either with a piezoelectric actuator or with a small electric field at its electrodes, typically on the range of few mV.

Attention should be so that the TF is not excited with electromagnetic fields.

Acoustic excitation is also a possibility though more difficult to trigger.

The detection is very easy either using a current to voltage amplifier or a voltage to voltage amplifier. Gains of the order of $10^7\Omega$ in the first case and 100 in the second case result in signal of the order of a mV/Å of vibration.

It was also shown that the TF can easily be used as a piezoelectric scanner moving about 6 Å per applied volt.

5.2 An AFM with a tuning fork

In the third chapter we have seen how easy is to use the TF together with a tungsten etched tip as a force transducer.

The TF is perfectly suited for making up an atomic force probe.

A comparison between a conventional cantilever and the TF leads to the conclusion that they can probe similar interactions even though they exhibit very different spring constant.

The sensitivity, in fact, depends on the dynamic spring constant that can be defined as:

$$k_{dynamic} = \frac{k}{Q} \tag{5.4}$$

The higher Q factor of the TF leads to higher settling times ($\approx$ 300ms) when compared to a Si cantilever ($\approx 30ms$). The consequence is that the measurements are intrinsically slower whether they are made using a lock in or a PLL.

The AFM images taken with the methods described here resemble the images taken with more conventional approaches.

The TF, together with its tip, was also used in the context of an atomic force probe to study the interactions between a body moving parallel to a surface and

the surface. The main conclusion is that the forces become important only when the tip is at the onset of contact with the sample.

5.3 An AFM in a synchrotron sample holder

In any experiment were the goal is to combine AFM with synchrotron radiation, even in the most simple case where one would like to obtain the topography of the illuminated region it is crucial to align the X-ray beam with the tip.

The rough alignment is easily done since photoelectric effect on the tip leads to a current flow of more than 1nA for beams with 10^12 photons/s. For sharp tips the vertical alignment of the tip apex is somewhat difficult. This is because the current slowly falls down as the X-ray beam is moved vertically away from the tip. In most of the cases, a fine vertical alignment can only be done if the exact tip profile is known from SEM images. Implementation of *smart tips* will facilitate the tip apex alignment tremendously.

Further, it was estimated that only absorption happening at less than 30nm from the surface contributes to the final signal.

We saw how the X-AFM tip can also be used to collect sample-emitted photoelectrons.

The signal detection is in most of the cases done using a lock-in amplifier.

The phase lag between the X-ray beam intensity and signal intensity allows to distinguish electrons from photons because there is a phase difference of 180Deg between the two measurements.

We have then showed some results where the tip of the X-AFM was used as a spectroscopy detector. If on one hand to measure the absorption with the X-AFM tip is straight forward on the other hand the lateral resolution is still dominated by the beam footprint.

A successful combination of both techniques where chemical contrast can be obtained simultaneously with the AFM topography can only happen through the use of *smart tips*. Using such tips we estimate to obtain a lateral resolution better than 50nm.

Since the tip can collect either photons as well as photoelectrons, diffraction is also a possibility. The angular resolution can not be compared to that obtained using more conventional and sophisticated methods. However, it is possible to identify what in the sample is diffracting. This may be useful to align the tip and the X-ray beam in a particular diffracting particle. Here again, *smart tips* can play in important role in reducing the background and enhancing the signal.

The most successful experiment was when X-ray diffraction was combined with indentation. The X-AFM tip was used to elastically and plastically deform (indent) a surface. This was done in a synchrotron beam line, and so, diffraction from the deformed surface was simultaneously measured.

The evolution of the TF resonance frequencies were recorded for each indentation depth as well as the evolution of the diffractions peak. The two information altogether allowed to derive the Young modulus of a SiGe particle. In such derivation there are no adjustable parameters. The particle size was of almost $1\mu m$. Unfortunately no experiment has been performed on smaller particles yet.

As a final remark it seems obvious that the future of such techniques depends on the successful design and implementation of *smart tips*.

5.4 Perspectives

In the future other techniques could be explored without changing the present experimental setup. These include Scanning Capacitance Microscopy, Electrostatic Force Microscopy, etc... We can add AFM in the line above because we have never tried to measure the change in the interaction between the tip and sample while illuminating it with X-rays. Consider tip-sample distances where the chemical bonds strongly intervene to the shape of the approach curve. As the sample is illuminated, a change in the interactions should be measured due to a modification of the electron density of states.

Therefore, we believe that a real combination of scanning probe techniques can be advantageous when compared to the case of this thesis where the tip collects charges in TEY mode or photons. We have to choose to measure some property or state that produces significant changes in the measured quantities as a function of tip-sample distances. In this way no such thing as a *smart tip* is required.

Bibliography

[1] M. von Laue, Concerning the detection of x-ray interferences, *Nobel Lectures, Physics* **1901-1921**, 1914

[2] Bragg W.L. The Specular Reflexion of X-rays, *Nature* **90** p. 410, 1912

[3] Bragg W.H., Bragg W.L., The structure of the diamond, *Nature* **91** p. 557, 1913

[4] I. A. Vartanyants, I.K. Robinson, J.D. Onken, M.A. Pfeifer, G.J. Williams, F. Pfeiffer, H. Metzger, Z. Zhong, G. Bauer, Coherent x-ray diffraction from Quantum dots, *Phys. Rev. B* **71** p. 245302, 2005

[5] M. Pfeifer, G.J. Williams, I.A. Vartanyants, R. Harder, I.K. Robinson, Three-dimensional mapping of a deformation field inside a nanocrystal, *Nature* **442** p. 63, 2006

[6] G. Binnig, H. Rohrer, Ch. Gerber, E. Weibel, (7×7) Reconstruction on Si(111) Resolved in Real Space, *Phys. Rev. Lett.* **50** p. 120, 1983

[7] Binnig G, and H. Rohrer, Nobel Lecture: Scanning tunneling microscopy from birth to adolescence, *Rev. Mod. Phys.* **59** p. 615, 1987

[8] G. Binnig, C. F. Quate, C. Gerber, Atomic force microscope, *Phys. Rev. Lett.* **56** p. 930, 1986

[9] D. Sarid, Scanning Force Microscopy, Oxford Series in Optical and Imaging Sciences, New York: Oxford University Press, 1991

[10] Giessibl F J, Advances in atomic force microscopy, *Rev. Mod. Phys.* **75** p. 949, 2003

[11] Giessibl, F. J., Atomic resolution of the silicon (111)-(7×7) surface by atomic force microscopy *Science* **267** p. 6871, 1995

[12] Franz J. Giessibl, Atomic resolution on Si. (111)-(7×7) by noncontact atomic force microscopy with a force sensor based on a quartz tuning fork, *Appl. Phys. Lett.* **73** p. 3956, 1998

[13] M. Ternes, C. P. Lutz, C. F. Hirjibehedin, F. J. Giessibl, A. J. Heinrich, The force needed to move an atom on a surface, *Science* **319** p. 1066, 2008

[14] T. Scheler, M. S. Rodrigues, T.W. Cornelius, C. Mocuta, A. Malachias, R. Magalhães-Paniago, F. Comin, J. Chevrier, and T.H. Metzger, *Appl. Phys. Lett.* **94** p. 023109, 2009

[15] J.R. Fineup, Reconstruction of a complex-valued object from the modulus of its Fourier transform using a support constraint, *J. Opt. Soc.* p. 118, 1987

[16] S. Marchesini, H. He, H.N. Chapman, S.P. Hau-Riege, A. Noy, M.R. Howells, Weierstall, J.C.H. Spence, X-ray image reconstruction from a diffraction pattern alone, *Phys. Rev. B* **68** p. 140101, 2003

[17] European FP6 project X-Tip, 2004-2007 (STRP 505634-1)

[18] Rugar D, Mamin H J, Guethner P, Lambert S E, Stern J E, McFadyen I and Yogi T, Magnetic Force Microscopy: General principles and application to longitudinal recording media, *J. Appl. Phys.* **68** p. 1169, 1990

[19] F. Baudelet, X-ray magnetic circular dichroism. *Neutron and X-ray spectroscopy*, ed. by F. Hippert et al. Dordrecht: Springer, p. 103, 2006

[20] M. Sanchi, J. Vogel, Magnetism and synchrotron radiation. *Lecture Notes in Physics*, Berlin: Springer **565** p. 87, 2001

[21] J K Gimzewski, R. Berndt, R. R. Schlittler, Observation of local photoemission using a scanning tunneling microscope, *Ultramicroscopy* **366-37** p. 42, 1992

[22] Saito A, et al., Development of a scanning tunneling microscope for in situ experiments with a synchrotron radiation hard-X-ray microbeam, *J. Sync. Rad.* **13** p. 216, 2006

[23] Eguchi T, J. Maruyama, K. Manabe, K. Kitamoto et al., Element specific imaging by scanning tunneling microscopy combined with synchrotron radiation light, *Appl. Phys. Lett.* **89** p. 243119, 2006

[24] Matsushima T, Development and trial measurement of synchrotron-radiation-light-illuminated scanning tunneling microscope, *Rev. Sci. Inst.* **75** p. 2149, 2004

[25] Ishii M, X-ray absorption fine structure measurement using a scanning capacitance microscope: Trial for selective observation of trap centers in the nm region, *Jpn J. Appl. Phys.* **41** p. 4415, 2002

[26] Williams C C, Hough W P, and Rishton, Scanning Capacitance Microscopy on a 25 nm scale, *Appl. Phys. Lett.* **55** p. 203, 1989

[27] Girard P, Electrostatic force microscopy: principles and some applications to semiconductors, *Nanotechnology* **12** p. 485, 2001

[28] M. Nonnenmacher, M. P. O'Boyle, H. K. Wicramasinghe, Kelvin probe force microscopy, *Appl. Phys. Lett.* **58** p. 2921, 1991

[29] T. Vančura, S. kičin, T. Ihn, K. Ensslin, M. Bichler, W. Wegscheider, Kelvin probe spectroscopy of a two-dimensional electrons gas below 300 mK, *App. Phys. Lett.* **83** p. 2602, 2003

[30] Betzig E, Finn P L, and Weiner J S, Combined shear force and near-field scanning optical microscopy, *Appl. Phys. Lett.* **60** p. 2484, 1992

[31] Karrai K, and Grober R D, Piezoelectric tip-sample distance control for near field optical microscopes, *Appl. Phys. Lett.* **66** p. 1842, 1995

[32] L. N. Kantorovich, A. I. Livhits, M Stoneham, Electrostatic energy calculation for the interpretation of scaning probe microscopy experiments, *J. Phys.* **12** p. 795, 2000

[33] K. Karrai, R. D. Grober, Piezoelectric tip sample distance control for near field optical microscopes, *Appl. Phys. Lett.* **66** p. 1842, 1995

[34] F. J. Giessibl, High-speed force sensor for force microscopy and profilometry utilizing a quartz tuning fork, *Appl. Phys. Lett.* **73** p. 3956, 1998

[35] Y. SEO , P. Cadden-Zimansky, V. Chandrasekhar, Low-temperature scanning force microscopy using a tuning fork transducer, *Korean Phys. Soc.* **50** p. 378 , 2007

[36] Y. Seo, W. Jhe, C. S. Hwang, Electrostatic force microscopy using a quartz tuning fork, *Appl. Phys. Lett.* **80** p. 4324, 2002

[37] W. H. J. Rensen, N. F. van Hulst, A. G. T. Ruiter and P. E. West, Atomic steps with tuning-fork-based noncontact atomic force microscopy, *Appl. Phys. Lett.* **75** p. 1640, 1999

[38] M. Labardi, M. Allegrini, Noncontact friction force microscopy based on quartz tuning fork sensors, *Appl. Phys. Lett.* **89** p. 174104, 2006

[39] M. Heyde, M. Kulawik, H.-P. Rust, H.-J. Freund, Double quartz tuning fork sensor for low temperature atomic force and scanning tunneling microscopy, *Rev. Sci. Instrum.* **75** p. 2446, 2004

[40] Timoshenko S., Vibration Problems in engineering. Second edition. New york: D. Van Nostrand Company, Inc., 1928

[41] H. B. Callen, T. A. Welton, Irreversibility and Generalized Noise, *Phys. Rev.* **83** p. 34, 1951

[42] A. N. Cleland, M. L. Roukes, Noise processes in nanomechanical resonators, *J. Appl. Phys.* **92** p. 2758, 2002

[43] A. Einstein, Investigations on the theory of, the Brownian motion (1926), edited by R. Furth, Dover Publications, Inc, 1956

[44] J. Renn, Einstein's invention of Brownian motion, *Ann. Phys.* **14** p. 23, 2005

[45] F. J. Giessibl, S. Hembacher, H. Bielefeldt, J. Mannhart, Subatomic Features on the Silicon (111)-(7×7) Surface Observed by Atomic Force Microscopy, *Science* **289** p. 472, 2000

[46] M. A. Lantz, H. J. Hug, R. Hoffman, P. J. A. van Schendel, P. Kappenberger, S. Martin, A. Baratoff, H.-J. Güntherodt, Quantitative Measurement of Short-Range Chemical Bonding Forces, *Science* **291** p. 2580, 2001

[47] Y. Martin, C. C. Williams, and H. K. Wickramasinghe, *J. Appl. Phys.* **61** p. 4273, 1987

[48] A. J. Melmed, The art and Science and other aspects of making sharp tips, *J. Vac. Sci. Technol.* B **9** p. 601, 1991

[49] J. P. Ibe, P. P. Bey, Jr., S. L. Brandow, R. A. Brizzolara, N. A. Burnham, D. P. Dilella, K. P. Lee, C. R. K. Marrian, R. J. Colton, On the electrochemical etching of tips for scaning tunneling microscopy, *J. Vac. Sci. Technol. A* **8** p. 3570, 1990

[50] A. G. T. Ruiter, J. A. Veerman, K. O. van der Werf, N.F. van Hulst, Dynamic behavior of tuning fork shear-force feedback, *Appl. Phys. Lett.* **71** p. 28, 1997

[51] R. D. Grober, J. Acimovic, J. Schuck, D. Hessman, P. J. Kindleman, J. Hespanha, A. S. Morse, K. Karrai, I. Tiemann, S. Manus, Fundamental limits to force detection using quartz tuning forks, *Rev. Sci. Inst.* **71** p. 2776, 2000

[52] K. Karrai, I. Tiemann, Interfacial shear force microscopy, *Phys. Rev. B* **62** p. 62, 2000

[53] M. J. Gregor, P. G. Blome, J. Schöfer, R. G. Ulbrich, Probe-surface interaction in near-field optical microscopy: The nonlinear bending force mechanism, *Appl. Phys. Lett.* **68** p. 308, 1995

[54] B. C. Stipe, H. J. Mamin, T. D. Stowe, T. W. Kenny, D. Rugar, Noncontact Friction and Force Fluctuations between Closely Spaced Bodies, *Phys. Rev. Lett.* **87** p. 96801, 2001

[55] J. R. Zurita-Sanches, J.-J. Grefet, L. Novotny, Friction forces arising from fluctuating thermal fields, *Phys. Rev. A.* **69** p. 22902, 2004

[56] H. Göttlich, R. W. Stark, J. D. Pedarnig, W. M. Heckl, Noncontact scanning force microscopy based on a modified tuning fork sensor, *Rev. Sci. Inst.* **71** p. 3104, 2000

[57] E-E Koch, D. E. Eastman, Y. Farge, Synchrotron Radiation - A Powerful tool in Science, *Handbook of Synchrotron Radiation*, ed. by Ernst-Eckhard Koch. Hamburg: North-Holland Publishing company, **1a** pp 159., 1983

[58] S. Krinsky, M. L. Perlman, R.E. Watson, Characteristics of Synchrotron radiation and of its sources, *Handbook of Synchrotron Radiation*, ed. by Ernst-Eckhard Koch. Hamburg: North-Holland Publishing company, **1a** p. 67170, 1983

[59] C.-O. Almbladh, L. Hedin, Beyond the one-electron model: Many-body effects in atoms, molecules, and solids, *Handbook of Synchrotron Radiation*, ed. by Ernst-Eckhard Koch. Hamburg: North-Holland Publishing Company, **1b** p. 611898, 1983

[60] A. Fontaine, Interaction of X-rays with matter: X-ray absorption spectroscopy, *Neutron and Synchrotron radiation for condensed matter studies*, ed. by J. Baruchel et al.. Les Ulis: Springer, **1** p. 323, 1993

[61] B. Lengeler, Extended Absorption Fine Structure, *Neutron and X-ray Spectroscopies*, ed. by F. Hippert et al.. Dordrecht: Springer, p.149, 2006

[62] Lytle F W, Via G H, Sinfelt J H, *Synchrotron Radiation Research*, ed. H. Winick, S. Doniach. New York: Plenum 401, 1980

[63] E. A. Stern and S. M. Heald, E. E. Koch, Principles and Applications of EXAFS, *Handbook of Synchrotron Radiation*, Hamburg: North-Holland Publishing Company, **1b** p. 9951014, 1983

[64] E. A. Stern and S. M. Heald, E. E. Koch, Photoelectron Spectroscopy, *Handbook of Synchrotron Radiation*, Hamburg: North-Holland Publishing Company, **1b** p. 905994, 1983

[65] M. Grioni, Photoelectron Spectroscopy, *Neutron and X-ray Spectroscopies*, Dordrecht: Springer p.189-237, 2006

[66] B. P. Tonner, D. Dunham, T. Droubay, J. Kikuma, J. Denlinger, E. Rotenberg, A. Warwick, The development of electron spectromiscroscopy, *J. Elect. Spect. and related phenomena* **309**, 1995

[67] G. J. Mcintyre, Single-Crystal Diffractometry with monochromatic X-rays and Neutrons. *Neutron and Synchrotron radiation for condensed matter studies*, ed. by Baruchel et al. Les Ulis: Springer, **1**, p. 179, 1993

[68] V. M. Kaganer. Crystal truncation rods in kinematical and dynamical x-ray diffraction theories, *Phys. Rev. B* **75** p. 245425, 2007

[69] J. L. Hodeau and H. Renevier, Anomalous Scattering and Diffraction Anomalous Fine Structure, *Neutron and X-ray Spectroscopies*, ed by F. Hilbert et al, Dordrecht: Springer, p. 239-269, 2006

[70] A. Freund, Anomalous scattering, ed. by S. Ramaseshan, S.C. Abrahams, Munkgsgaard Copenhagen 69, 1975

[71] Stragier H, Cross J O, Rehr J J, Sorensen L B, Bouldin C E, Woicik J C, Diffraction anomalous fine structure: A new x-ray structural technique, *Phys. Rev. Lett.* **69** p. 3064, 1992

[72] Ivan N. Stranski and L. Von Krastanow, Abhandlungen der Mathematisch-Naturwissenschaftlichen Klasse. Akademie der Wissenschaften und der Literatur in Mainz, **146** p. 797, 1939

[73] Greegor R B, Lytle F W, Kortright, J, Fischer-Colbrie A, Determination of the structure of GeO_2-SiO_2 Glasses by EXAFS and X-ray Scattering, *Journal of Non-Crystalline* **87** p. 311, 1987

[74] C. Mocuta, J. Stangl, K. Mundboth, T.H. Metzger, G. Bauer, I.A. Vartanyants, M. Schmidbauer, T. Boeck, Beyond the ensemble average: X-ray microdiffraction analysis of single SiGe islands, *Phys. Rev. B.* **77** p. 245425, 2008

[75] C. Anthony, Fischer-Cripps, Introduction to contact mechanics, Berlin: Springer, (Mechanical Engineering Series), p. 226, 2000

[76] S. Sen, S. Subramanian, D. E. Discher, Indentation and Adhesive Probing of a Cell Membrane with AFM: Theoretical Model and Experiments *Byophisical Journal* **89** p. 3203, 2005

[77] M. S. Bischel, M. R. Vanlandingham, R. F. Eduljee, J. W. Gillespie Jr., J. M. Schultz, On the use of nanoscale indentation with the AFM in the identification of phases in blends of linear low density polyethylene and high density polyethylene, *J. Matt. Sci.* **35** p. 221, 2004

[78] T. Zhu, J. Li, K. J. Van Vliet, S. Ogata, S. Yip, S. Suresh, Predictive modeling of nanoindentation-induced homogeneous dislocation in copper *J. Mech. Phys. Solids* **52** p. 691, 2004

[79] K. J. Van Vliet, S. Tsikata, S. Suresh, Model experiments for direct visualization of grain boundary deformation in nanocrystaline metals *App. Phys. Lett.* **83** p. 1441, 2003

[80] M.D. Uchic, D.M. Dimiduk, J.N. Florando, W.D. Nix, Sample Dimensions Influence Strength and Crystal Plasticity *Science* **305** p. 986, 2004

[81] Y. Choi, S. Suresh, Size effects on the mechanical properties of thin polycrystalline metal films on substrates, *Acta Materiallia* **50** p. 1881, 2002

[82] K. J. Van Vliet, J. Li, T. Zhu, S. Yip, S. Suresh, Quantifying the early stages of plasticity through nanoscale experiments and simulations, *Phys. Rev. B* **67** p. 104105, 2003

[83] Y. Choi, K. J. Van Vliet, J. Li, S. Suresh, Size effects on the onset of plastic deformation during nanoindentation of thin films and patterned lines *J. Appl. Phys.* **94** p. 6050, 2003

[84] W.C. Oliver, G.M. Pharr, An improved technique for determining hardness and elastic modulus using load and displacement sensing indentation experiments *J. Mater. Res.* **7** p. 1564, 1992

[85] J. Jang, M.J. Lance, S. Wen, T. Y. Tsui, G. M. Pharr, Indentation-induced phase transformations in silicon: influences of load, rate and indenter angle on the transformation behaviour, *Acta Materialia* **53** p.1759, 2005

[86] L. Vegard, *Zeitschrift fuer Physik*, **5** p. 17, 1921

[87] J.J. Wortman, R.A. Evans, Youngs modulus, Shear modulus, and Poisson's ratio in Silicon and Germanium, *J. Appl. Phys.* **36** p. 153, 1965